NOVEL MEMBRANE SYSTEMS FOR

ENERGY HARVESTING AND WATER RECOVERY

by

SARAH MOUSSADDY

A dissertation submitted in partial fulfillment of the
requirements for the degree of

DOCTOR OF PHILOSOPHY IN MECHANICAL ENGINEERING

2023

Oakland University
Rochester, Michigan

Doctoral Advisory Committee:

Jonathan Maisonneuve, Ph.D., Chair
Kodiah Beyeh, Ph.D.
Sarah Beetham, Ph.D.
Xia Wang, Ph.D.
Peng Zhao, Ph.D.

ACKNOWLEDGMENTS

I would like to express my praise and gratitude to the God for his blessing and surrounding me with valuable, precious, and supportive people who helped me in this journey to get my PhD.

This academic achievement would have not come into reality without the contributions and support of Dr. Maisonneuve for his valuable advice, continuous support, and guidance during my PhD study. His input and comments were always beneficial and to the point at every stage of the research project which always helped me solve the technical difficulties, in research, in an efficient way.

I would like to extend my sincere thanks to Dr. Kodiah Beyeh, Dr. Sarah Beetham, Dr. Xia Wang and Dr. Peng Zhao for being in my PhD committee and for their insightful comments and suggestions during my study.

I would like to thank my friends, lab mates, and research team for a cherished time spent together in the lab and support all through my studies.

Finally, words cannot express my gratitude to my beloved mother, husband and my brothers and sister, I could not have undertaken this journey without their prayers, help, love and encouragement. And to my late father, this pursuit would not have begun and been possible without his valuable advice and guidance and all the insightful conversations we've had before I embark on this journey.

Sarah Moussaddy

ABSTRACT

NOVEL MEMBRANE SYSTEMS FOR

ENERGY HARVESTING AND WATER RECOVERY

By

Sarah Moussaddy

Adviser: Jonathan Maisonneuve, Ph.D.

Improving energy efficiency is an important part of the transition for mitigating greenhouse gas emissions. This dissertation introduces two novel membrane processes that can improve the energy efficiency of key sectors: (1) energy recovery from exhaust gases for improved power plant efficiencies, and (2) fertilizer-based liquid desiccant systems for improved dehumidification of indoor plant farms.

Regarding the first, large amounts of energy are currently wasted from gradients of gas mixtures that are released from power plant exhaust. The energy is estimated to be 1-2 % of the plant's overall power capacity. To recover this energy, this work introduces a membrane process that uses ambient air as a sweep gas to draw concentrated gases from an exhaust source to do mechanical work in the form of compressed permeate gas flow. The concept and the developed numerical model are experimentally validated with a polydimethylsiloxane membrane using a binary gas mixture of nitrogen (N_2) and water vapor in a first study, where power density of 57 mW/m^2 is observed under relatively conservative test conditions. In a second study, N_2 and carbon dioxide (CO_2) was used and power of up to 6.35 W/m^2 is experimentally observed when pure CO_2 is supplied as feed, and up to 0.37 W/m^2 when 20 % CO_2 feed is supplied.

Regarding the second application of membranes, the focus is on a solution to improve the efficiency of energy, water, and fertilizer used in agriculture. This work introduces the novel concept of using fertilizer as a liquid desiccant for energy efficient dehumidification of indoor plant environments. The first-ever experimental demonstration of the concept is done using a polydimethylsiloxane membrane and a water vapor flux of up 1.90 $g/m^2/h$ is obtained. Dehumidification is confirmed across a range of standard greenhouse conditions and operating parameters. A theoretical modelling analysis is also performed to investigate the effects of operating conditions on the specific energy. As a result, a specific energy as low as 0.15 kWh/ kg is obtained under certain conditions with optimized desiccant temperatures and air flow rates.

TABLE OF CONTENTS

TABLE OF CONTENTS - Continued

TABLE OF CONTENTS - Continued

TABLE OF CONTENTS - Continued

TABLE OF CONTENTS - Continued

TABLE OF CONTENTS - Continued

LIST OF FIGURES

LIST OF TABLES

CHAPTER ONE

INTRODUCTION

1.1 Background

Environmental pollution and global warming are escalating at a rapid pace, and efforts to decrease the greenhouses emissions from human activity are continuously expanding. More and more programs and policies are being implemented by state and local governments to promote energy efficiency and renewable energy. Currently, fossil fuel represents around 80% of primary energy sources in the US, and it is the major source of air pollution that poses risks to human health [1]. It is also the largest source of greenhouse gas emissions from human activities that is contributing to global climate change [2]. Thus, improving the energy efficiencies of existing technologies, that yield to lower energy consumption, can help minimize the effect of fossil fuel air pollution and its environmental consequences along with the implementation of more renewable energy technologies in the future.

1.2 Membrane-Based Energy Recovery for Fresh Air Building Ventilation

In the US, residential and commercial buildings account for almost 40% of total energy consumption in 2021 and around 38% of total carbon dioxide (CO_2) emissions [1]. From this total consumed energy, around half of it is related to heating, ventilation, and air-conditioning (HVAC) for buildings [3-4]. Furthermore, the energy footprint of buildings may increase in the near future as recent guidance calls for additional fresh air ventilation to mitigate risks associated with COVID-19 and other respiratory diseases. Therefore,

improving the energy efficiency of HVAC systems is important for the cost-effectiveness, health, and sustainability of buildings.

Membrane-based energy recovery ventilation (ERV) systems have been proposed as a solution to reduce the energy consumption of fresh air ventilation, while still maintaining the indoors thermal comfort by preconditioning inlet air before it enters the HVAC unit [5-7]. As shown in Figure 1.1, a membrane-based ERV unit will allow simultaneous heat and moisture transfer between fresh air and exhaust air while eliminating direct contact so as to prevent contamination of the airflow. Thereby, the membrane-based ERV system is capable of recovering valuable latent and sensible energy from building exhaust to pre-cool and pre-dry incoming fresh air in the summer, and to pre-heat and pre-humidify incoming fresh air in the winter, without compromising fresh air quality.

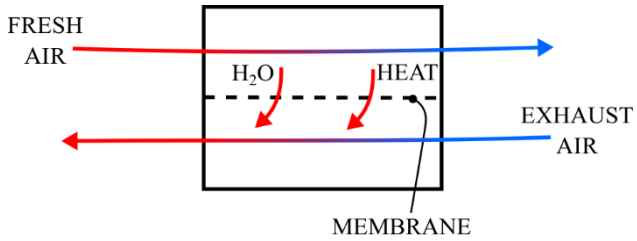

Figure 1.1 Latent and sensible energy can be recovered from building exhaust via water vapor and heat transfer across membrane-based energy recovery ventilation (ERV) systems.

In 2019, our laboratory group at Oakland University proposed a membrane-based ERV system in response to the DTE E-Challenge program. The project is on-going and operation and performance of the proposed membrane-based ERV technology is being retrofitted in the OU Campus Police Building's ventilation system, as shown in Figure 1.2. The proposed energy conservation measure is expected to reduce electricity used for summer cooling by nearly 50 %, and to reduce thermal energy used for winter heating by nearly 70 %.


Figure 1.2 The Oakland University Campus Police & Support Services Building with the roof-top unit on the left and the membrane-based energy recovery ventilation system being installed on the right.

As a result of our group's work on membrane-based ERV, we were inspired to introduce two novel spin-off concepts using dense membrane-based systems, which are the focus of this dissertation: (1) a membrane-based system for converting energy from gradients of exhaust gases to useful power, and (2) a membrane-based dehumidification system that uses fertilizer liquid desiccant to efficiently control indoor plant environment conditions. The goal of this work is to introduce these novel concepts in order to improve energy efficiency and help support a sustainable future.

1.3 Power Generation from Gas Permeate

With the increasing challenge of meeting growing needs for energy for the global population, the introduction of new alternative energy technology as well as the improvement of existing state of the art technologies are required, both in terms of their efficiency and their environmental impact. Certain projections suggest that coal-fired power capacity will continue to increase by as much as 50 % in the next 10 years [9]. The rapid expansion of natural gas power plants is also expected to continue, and in fact now accounts for the majority of carbon emissions in the United States [10]. This challenge led

to the first proposed spinoff, which is that of a membrane-based system which uses the chemical potential of gas mixture gradients across a selective membrane to generate mechanical work using an expander or a turbine. For this system, my research focused on the energy potential of the flue gas of power plants that is currently wasted when the exhaust gas is released into the atmosphere. While the implementation of CO_2 capture technologies has been previously proposed, the chemical potential available from gas mixing between exhaust sources and the atmosphere has so far been mostly overlooked. From evaluating the Gibbs energy of mixing, the energy available from both CO_2 and water vapor contained in coal-fired and gas-fired plant exhaust is equivalent to roughly 1-2 % of the plant power capacity. Thus, harvesting this energy and converting it to useful work can help support a sustainable energy future by improving the efficiency of thermal power plants and thereby reducing harmful emissions per unit of electricity generated. Only recently a few systems for capturing this energy and converting it to useful work have been proposed. These include a CO_2 powered capacitive mixing process studied by Hamelers et al. [11,12] and Porada et al [13], and a CO_2 powered flow cell proposed by Kim et al. [14]. Such electrochemical processes, however, require preparation of working solutions of dissolved CO_2, which is limited by the relatively modest tendency of CO_2 to dissolve in water. Also, these processes ignore the potential of other concentrated gas species that are also available in exhaust streams, such as water vapor.

In order to increase the potential energy recovered, this work introduces a novel membrane process that converts the energy from gas concentration gradients of water vapor, CO_2, or other gases to mechanical work, in the form of an expanding volume of pressurized gas. In this process, a membrane is used to separate a concentrated feed gas

from some exhaust source with a diluted sweep gas of ambient air, which is mechanically pressurized. Driven by the partial pressure gradients between the gases, permeable gas species such as water vapor and CO_2 will cause the volume of pressurized sweep gas to expand, even against some load such as a turbine, and thus convert the chemical gradient to mechanical work. Although membranes have been already introduced for energy conversion [15-18], this is the first study of a gas permeation process for power production.

In Chapter Two, I introduce the first demonstration of energy production from water vapor permeate against an applied pressure. In this study, I first establish the thermodynamic limit and the real maximum energy density that can be recovered from the available Gibbs energy of mixing. The non-ideal transport dynamics across the membrane, such as reverse flux and membrane boundary effects, are also studied, and a numerical model is defined. The effect of the non-ideal transport dynamics on the amount of energy density potential is studied. Simulation results of the numerical model are then compared to a series of experimental results, validating the model.

In Chapter Three, I perform a study on the power generation potential of gradients of carbon dioxide available between power plant exhaust flue and ambient air. I establish the fundamental transport dynamics for the membrane system that are then used in the numerical model. Next, simulation results from a numerical model are compared against experimental observations. Performance is evaluated over a range of flow rates and concentrations, and analysis of critical operating conditions is provided. Finally, the effect of turbine and compressor efficiency on net power density is analyzed and the requirements for maintaining a favorable energy balance are discussed.

1.4 Fertilizer-Based Liquid Desiccants for Dehumidification

The second spinoff, that was inspired by the DTE E-Challenge ERV project, was the use of fertilizer solution as a liquid desiccant for humidity control and water recovery in indoor plant environments. This novel concept will help to lower the energy and water footprint of crops while providing food to the rapidly growing populations. Indoor plant environments such as greenhouses and vertical farms, have the potential to improve crop yields and considerably lower plant water consumption and to nearly close the water cycle of crops. Studies have shown 15-fold increases in specific yield for a variety of common food crops cultivated in indoor farms as compared to field production, due largely to the highly accurate microclimate control that is supported by indoor agriculture [19-22]. Other reports have indicated 80% reductions in chemical pesticide and herbicide use, due to effective protection to pathogens and contaminants that are offered by the controlled environment [23]. In addition, drastic reductions in the water footprint of crops are possible, as compared to field agriculture where much of the water used for irrigation is lost to soil evaporation and surface runoff. For example, up 95% lower water consumption has been achieved in hydroponic cultivation systems that employ water vapor recovery [24,25]. These and other advantages are responsible for the current rapid growth in controlled environment agriculture, and such developments can be part of a sustainable food production future.

Among the requirements of operating indoor plant environments is the need to regulate indoor humidity levels as excessive humidity can lead to inadequate nutrient uptake, poor flowering and fruiting, and disease, while on the other hand, insufficient humidity can lead to high plant transpiration and wilting. A simple and low-tech strategy involves exhausting

the humid air and replacing it with dry outdoor air [26-28]. However, such ventilation involves a large operational cost to heat or cool the incoming fresh air, and undermines certain functionality of the controlled environment, such as CO_2 enrichment, pest control, and water vapor recycling. Conventional dew-point condensers, which are commonly used for building air-conditioning, can be applied to plant environments, but these are energy intensive, requiring significant work to cool air to its dewpoint [29,30]. This inability to regulate humidity without changing temperature, means that additional energy to reheat the air is often required. In addition, condensation on the cooling coils may favor bacteria and mold growth, compromising the quality of the air that is conditioned and of the water that is recovered. More recently, liquid desiccant dehumidification has been proposed as an alternative for humidity removal and control [31]. However, these liquid desiccant solutions, normally made from salts such as lithium chloride (LiCl), magnesium chloride ($MgCl_2$) or lithium bromide (LiBr), require regeneration, and care must be taken to avoid releasing the typically toxic and corrosive desiccant into either the water supply or the ambient air of the plant environment. Recent regulations are posed to limit the energy consumption related to the dehumidification of the indoor plant environment [32]. Tang et al [33], recently evaluated dehumidification with a vapor compression cycle and found a specific energy of dehumidification to be between 0.36-0.94 kWh/kg for air relative humidity between 38-80%. In addition, a study conducted by Zhang et al [34], on a dehumidification system with a heat pump coupled to a membrane desiccant unit, obtained specific energy of dehumidification between 0.52-0.80 kWh/kg.

In Chapter Four, I introduce the novel concept of using fertilizer-based liquid desiccant to dehumidify indoor plant environments and recycle water vapor. Until now, the

possibility of using fertilizer rather than a typical desiccant to drive dehumidification has not been mentioned in the literature. The introduction of fertilizer solution as a desiccant is expected to not only help control humidity inside the greenhouse, but to recover water while diluting the fertilizer solution to be send to the plants without the need of regeneration, thus lowering the related energy. This study illustrates the theoretical and practical limitations in dehumidification potential of multiple fertilizer compared to a typical magnesium chloride desiccant. Fundamental transport dynamics are defined, and simulation results from a numerical model are generated for several common fertilizers across a range of typical greenhouse conditions, and across a range of possible operating conditions. The laboratory-scale prototype is presented along with the test protocol of the membrane-based dehumidification process, and the experimental results are compared against the simulations results to validate the numerical model. This study shows the first demonstration of fertilizer potential as a driving force for dehumidification.

In Chapter Five, the energy analysis on the system is performed to verify the capability of dehumidification while keeping low energy consumption. Specific energy is the ratio between the rates of energy use for desiccant and water vapor removal, and for a given set of conditions there will be some unique liquid desiccant temperature that balances these two rates to achieve the minimum specific energy. Therefore, a theoretical analysis is performed, and a numerical model is built and used to carry the energy analysis over a range of operational conditions.

Chapter Six concludes by summarizing my key contributions to the scientific literature, and by outlining future work. I outline possible future improvements on the performance of power generation that could be achieved from gas permeation from multi gas exhaust

sources, and from heat gain from hot exhaust sources. And for the second proposed system, the possible application of fertilizer as a desiccant for greenhouse dehumidification applications considering a batch process for a specific crop and greenhouse area, and all the related challenges.

1.5 Publications

This work has produced a total of 3 journal papers with another one in preparation, 1 conference oral presentations, 3 conference poster presentations, and 1 technical report.

1.5.1 Journal Papers

1. S. Moussaddy, S. Aryal and J. Maisonneuve, "Controlled Plant Environment Sustainability: A Specific Energy Analysis of Fertilizer-Based Liquid Desiccant Dehumidification", in preparation.

2. S. Moussaddy, S. Pushparajah, J. Maisonneuve, "Fertilizer-Based Liquid Desiccants: A Novel Concept for Energy Efficient Dehumidification and Water Vapor Recycling in Indoor Plant Environments," Applied Thermal Engineering, vol. 219 Part B, 119529, 2022.

3. S. Moussaddy and J. Maisonneuve. "Energy from carbon dioxide: Experimental and theoretical analysis of power generation from membrane-based sweep gas permeation". Journal of Membrane Science. Vol. 644: 120053, 2021.

4. S. Moussaddy, G. Yuan, and J. Maisonneuve. "A new concept for generating mechanical work from gas permeation". Journal of Membrane Science. Vol. 614: 118489, 2020.

1.5.2 Conference Presentations

1. S. Moussaddy and J. Maisonneuve, "Specific Energy Analysis of Fertilizer-Based Liquid Desiccant Dehumidification", poster presentation at the incoming North American Membrane Society (NAMS) Annual Meeting, Tuscaloosa, AL, May 2023.

2. S. Moussaddy and J. Maisonneuve, "Fertilizer-Based Liquid Desiccants for Efficient Dehumidification and Water Vapor Recycling in Indoor Plant

Environments", poster presentation at the North American Membrane Society (NAMS) Annual Meeting, Tempe, AZ, May 2022.

3. S. Moussaddy and J. Maisonneuve, "Energy from Carbon Dioxide via Membrane-Based Sweep Gas Permeation", poster and oral presentation at the North American Membrane Society (NAMS) Annual Meeting, Estes Park, CO, August 2021.

4. S. Moussaddy and J. Maisonneuve, "A new concept for generating mechanical work from gas permeation", poster presentation at the North American Membrane Society (NAMS) Virtual Annual Meeting, May 2020.

1.5.3 Technical Reports

1. S. Moussaddy, S. Aryal, J. Caldwell, O. Racette, J. Maisonneuve "Membrane-Based Energy Recovery Ventilation," Oakland University DTE Challenge 5, 2023.

CHAPTER TWO

A NEW CONCEPT FOR GENERATING MECHANICAL WORK FROM GAS PERMEATION

2.1 Original publication

Chapter 2 is based primarily on a paper that was published in the Journal of Membrane Science1[1]. This study was the first in literature to use the water vapor gradient across a membrane in a gas process to convert it to useful work. We experimentally validate the concept and demonstrate the use of membrane system, using a binary gas mixture of water vapor and N_2, for water vapor permeation into a pressurized sweep that can be used to generate mechanical work.

2.2 Introduction

Developing sustainable power infrastructure for a rapidly growing population will likely require both the introduction of new alternative energy technology, as well as the improvement of existing power plants, both in terms of their efficiency and their environmental impact. Capturing CO_2 from exhaust gases and improving power plant efficiency has received increasing attention in efforts to mitigate greenhouse gas emissions [35-39].

[1] S. Moussaddy, G. Yuan, and J. Maisonneuve. "A new concept for generating mechanical work from gas permeation". Journal of Membrane Science. Vol. 614: 118489, 2020.

DOI: 10.1016/j.memsci.2020.118489.

Currently, large amounts of energy are wasted from thermal plants when exhaust gases are released into the atmosphere. While the thermal potential of these exhaust streams has been previously considered [40], the chemical potential available from gas mixing has so far been mostly overlooked. As shown further on, we estimate that 3-4 Wh of energy are available from CO_2 and water vapor contained in every m^3 of coal-fired and gas-fired plant exhaust that is released to ambient air at 20 °C and atmospheric pressure. This is equivalent to roughly 1-2 % of plant capacity.

In this paper, we propose a novel membrane-based process for converting gas concentration gradients (including water vapor, CO_2, and other gases) to mechanical work, in the form of an expanding volume of pressurized gas. The process is illustrated in Figure 2.1. A selective membrane is used to separate concentrated feed such as exhaust gas, from a diluted sweep stream such as ambient air which is pressurized against a load. Driven by the partial pressure gradients between the gases, permeable gas species such as water vapor and CO_2 will cause the volume of pressurized sweep gas to expand against some load such as a turbine [41]. In this way, the chemical gradient is converted to mechanical work.

The goal of this study is to introduce and validate the concept of power generation from gas permeation. In this paper, we establish the theoretical limits of energy recovery from common exhaust gradients, introduce the fundamental transport dynamics for the proposed gas permeation process including non-ideal effects such as polarization and axial dilution, and experimentally validate the concept by demonstrating power generation using a simple binary gas mixture of nitrogen and water vapor across a commercial polydimethylsiloxane (PDMS) hollow fiber membrane. While membranes have previously been used for energy conversion [15-18,42], so far as we are aware, this is the first time a gas permeation process

has been suggested for power production, and also the first time that water vapor gradients in gas processes have been used for membrane-based power generation.

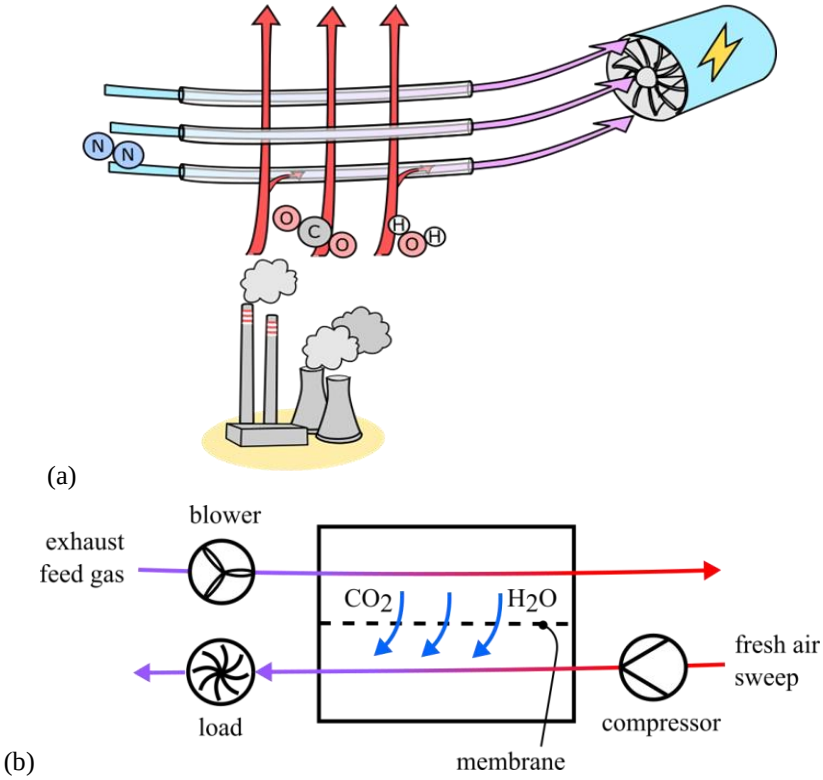

Figure 2.1. (a) Exhaust gas chemical potential gradient with the ambient air can be converted to useful work (b) An expanding volume of pressurized air is generated (with the potential to do mechanical work) via membrane-based gas permeation, in which diluted sweep gas is used to draw water vapor and CO_2 towards a load.

2.3 Theory

2.3.1 Limits to Energy Recovery

The thermodynamic limit to energy recovery from mixing two or more gases is described by the Gibbs energy of mixing. For gas species *i* contained in feed and sweep streams at constant temperature, the Gibbs energy of mixing is obtained from [43,44] (see Supplementary Note 2.1 for derivation):

$$\Delta G = -R\,T\left(x_{i_{F_{in}}}.\,n_{F_{in}}\ln\left(\frac{x_{i_{F_{OUT}}}}{x_{i_{F_{IN}}}}\right) + x_{i_{S_{in}}}.\,n_{S_{in}}\ln\left(\frac{x_{i_{S_{OUT}}}}{x_{i_{S_{IN}}}}\right)\right) \quad (2.1)$$

Where R is the gas constant, T is the absolute temperature, x_i is the mole fraction of species i and n_i is the amount of gas species i on the feed and sweep stream respectively. For convenience, the Gibbs energy can be normalized per unit of rich feed volume, and rewritten as [11]:

$$\frac{\Delta G}{V_F} = p_F\,x_{i,F}\left(\ln\gamma + \left(\frac{\beta}{\gamma}+1\right)\ln\left(\frac{1+\beta}{\gamma+\beta}\right)\right) \quad (2.2)$$

Where p_F is the pressure of the rich feed stream, which can be assumed to be atmosphere. The relative concentration of feed and sweep streams is expressed using $\gamma = p_{i,F} / p_{i,S}$, and the mixing ratio between feed and sweep streams is expressed using $\beta = n_{Sin} / n_{Fin}$.

Figure 2.2 provides a summary of the Gibbs energy of mixing common exhaust sources of concentrated water vapor and CO_2 (see Supplementary Note 2.2 for concentrations) with typical ambient air (1 vol.% water vapor and 0.03 vol.% CO_2). As shown, nearly 3.6 Wh of energy is available from the concentrated water vapor and CO_2 contained in each m^3 of natural gas-fired flue gas, as it mixes with fresh outdoor air. Given exhaust rates of a typically sized gas power plant, this energy can be normalized over the plant capacity, revealing that water vapor and CO_2 gradients from flue gas have energy potential of approximately 1.1 % of plant capacity. In addition, about 0.4 Wh/m^3 of energy is available from water vapor gradients in cooling tower exhaust. This is much lower than the energy density of flue gas, due to the relatively modest water vapor gradients available from the lower temperature cooling tower plumes. However, the sheer volume of cooling tower

exhaust makes this source quite significant relative to plant capacity (equivalent to another 0.4 % of plant capacity).

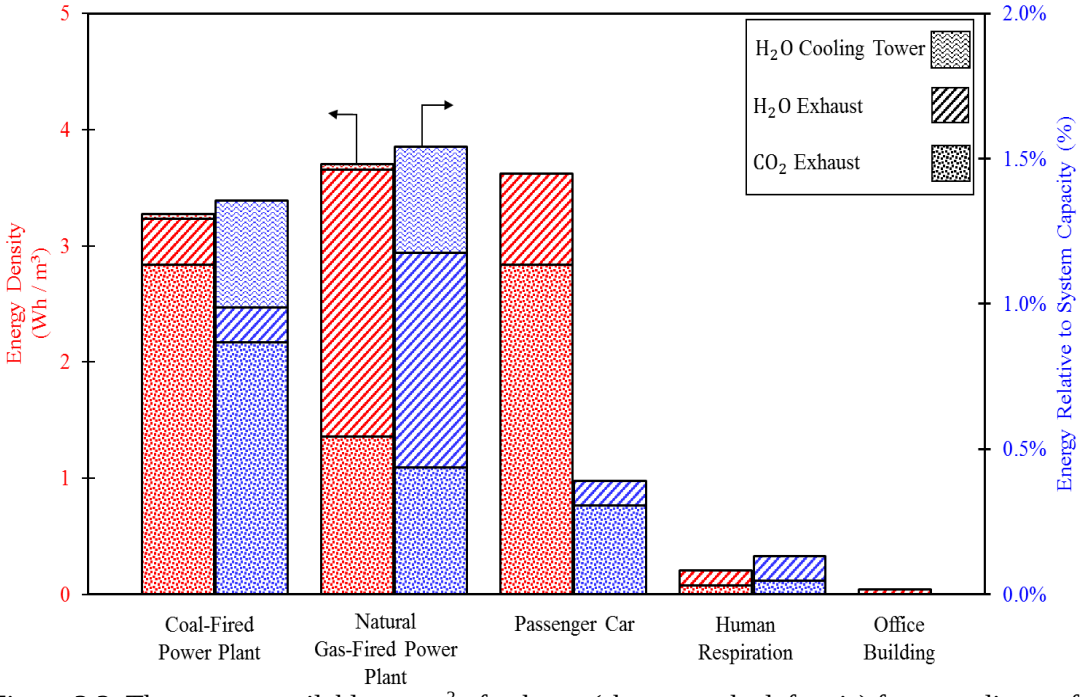

Figure 2.2. The energy available per m^3 of exhaust (shown on the left axis) from gradients of water vapor and CO2 available from various industrial, transportation, and biological sources. This energy density is related to the capacity of each system and expressed as a potential improvement in energy efficiency (shown on the right axis). Assumes exhaust is mixed with an unlimited volume of ambient air (1 vol.% water vapor and 0.03 vol.% CO_2) at 20 °C and atmospheric pressure.

Such energy potential represents possible increases in power plant efficiency that are non-trivial. Figure 2.2 also shows the potential of other common exhaust sources, including passenger vehicle exhaust, breath, and office building ventilation, and these hint at other broader applications of such energy recovery. However, recovering the Gibbs energy of mixing assumes a perfectly reversible process. In the proposed membrane-based gas permeation process, such reversibility would require that applied pressure be varied throughout the mixing process (for example along the length of the membrane) to maintain an infinitesimal partial pressure gradient, which is not practical. It also assumes a perfectly

selective membrane that is only permeable to species *i*, and a mixing ratio that approaches infinity wherein the concentration of species *i* in the feed would be maintained constant and only negligibly diluted throughout the mixing process. Furthermore, Figure 2.2 does not consider the potential of the whole exhaust stream and the gradients of each species, but rather provides only a measure of potential for water vapor and CO_2 gradients. The thermal characteristics of exhaust sources are also neglected. In the following sections, we outline several practical limitations to the process and illustrate their influence on performance.

2.3.2 Ideal Maximum Power

In order to be economically viable, energy conversion by gas permeation must not only be able to generate significant amounts of work, but also able to do so at cost-effective rates. A key metric in this regard is power density. Power density provides a measure of both the process performance and the membrane ability to rapidly convert potential energy to useful work. Power from species *i* is obtained from the volumetric expansion of that species observed on the sweep side $\Delta\dot{V}_{i,S}$ and the pressure difference applied across the membrane Δp. This pressure difference can be approximated as simply to $\Delta p = p_S - p_F$. When normalized over membrane surface area *A*, power density $\dot{W}$ and sweep side volumetric flux J_S provide a measure of system performance relative to size and hence cost.

$$\dot{W}_i = J_{i,S}\,\Delta p = \frac{\Delta\dot{V}_{i,S}}{A}\,\Delta p \tag{2.3}$$

Permeate flux of gas species *i* across a dense membrane with permeability B_i and thickness *l* is defined by Fick's Law modified in the solution-diffusion model, where the partial pressure gradient Δp_i of *i* acts as the driving force [45]. Permeate can then be

expressed as sweep side volumetric flux by assuming ideal gas behavior [46] (see Supplementary Note 2.3 for additional detail).

$$J_{i,S} = \frac{R\,T}{p_S}\frac{B_i}{l}\,\Delta p_i \qquad (2.4)$$

Where R is the gas constant, T is absolute temperature, and p_s is the pressure of the pressurized sweep gas.

Together, equation (2.3) and (2.4) describe a relationship between force, flow, and power that is illustrated with several examples in Figure 2.3. Considering feed with water vapor and CO_2 concentrations that approach those of (a) coal-fired flue gas, (b) natural gas-fired flue gas, and (c) cooling tower exhaust, and using ambient air for sweep gas (1 vol.% water vapor and 0.03 vol.% CO_2), we obtain the series of ideal flux and power curves shown. Impressive power densities of nearly 30 W/m^2 are observed. High power is obtained from polyether block amide (PEBA) membranes that are highly permeable to water vapor (B_{H2O} = 160,000 barrer), and that yield impressive flux even though partial pressure gradients of water vapor are relatively modest. The importance of membrane permeability to flux and power is illustrated by contrast between PEBA and PDMS. The latter PDMS membrane shows much lower permeability to water vapor (B_{H2O} = 40,000 barrer) and hence much lower power. In response to gradients of CO_2, the PDMS membrane shows better performance than PEBA, but the permeability in both cases (B_{CO2} = 3,000 barrer for PDMS and B_{CO2} = 300 barrer for PEBA) is much lower than for water vapor, and hence CO_2 power density is orders of magnitude less.

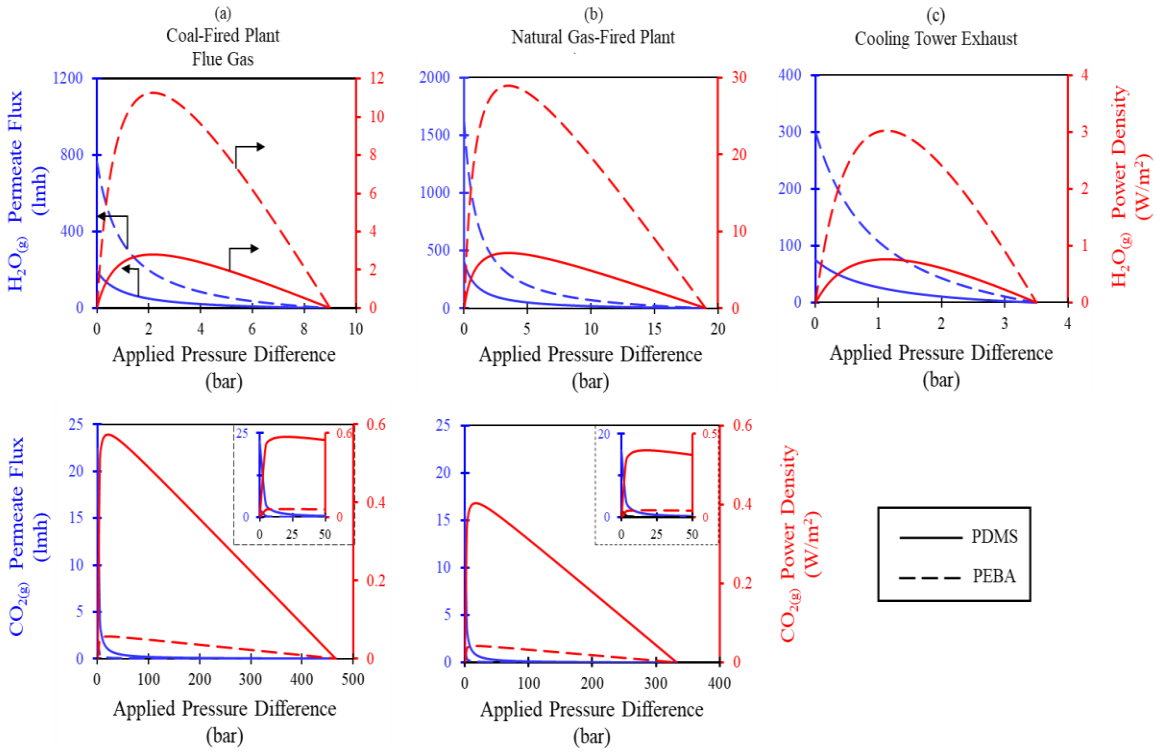

Figure 2.3. Gas permeate flux J and power density $\dot{W}$ of water vapor and CO2 given a number of feed gas concentrations including (a) flue gas from coal-fired plant, (b) flue gas from natural gas-fired plant, and (c) exhaust from cooling tower. In all cases mixing occurs with sweep gas of ambient air with 1 vol.% water vapor, 0.03 vol.% CO2 at 20°C. Polydimethylsiloxane (PDMS) is considered with water vapor permeability of BH2O = 40,000 barrer and CO2 permeability BCO2 = 3,000 barrer. Polyether block amide (PEBA) is considered with permeability of BH2O = 160,000 barrer and BCO2 = 300 barrer [40, 47]. Membrane thickness is l = 55 μm.

Figure 2.3 also illustrates the non-linear relationship between applied pressure and flux. As described in equation (2.4), increasing pressure on the sweep stream not only has the effect of reducing partial pressure gradients, but also of compressing the sweep stream and hence reducing volume of permeate. Maximum power is therefore achieved at applied pressures between 1 and 5 bar for the cases of water vapor gradients, and around 15 bar for the cases of CO_2 gradients.

The maximum power $\dot{W}_{max}$ from the membrane permeation process can be obtained analytically from equation (2.3) and (2.4), by considering the exact solution to $d\dot{W}/d\Delta p = 0$ (see Supplementary Note 2.3 for derivation).

$$\dot{W}_{i,max} = R\,T\,\frac{B_i}{l}\,p_F\left(\sqrt{x_{i,F}} - \sqrt{x_{i,S}}\right)^2 \tag{2.5}$$

Where x_F and x_S are the feed and sweep mole fractions of i, and where p_F is the feed pressure, which in an ideal frictionless system is atmosphere. This maximum power is obtained by applying the appropriate load pressure $\Delta p^{\dot{W}max}$, which is also determined from the exact solution to equation (2.3) and (2.4).

$$\Delta p^{\dot{W}max} = p_F\left(\sqrt{\frac{x_{i,F}}{x_{i,S}}} - 1\right) \tag{2.6}$$

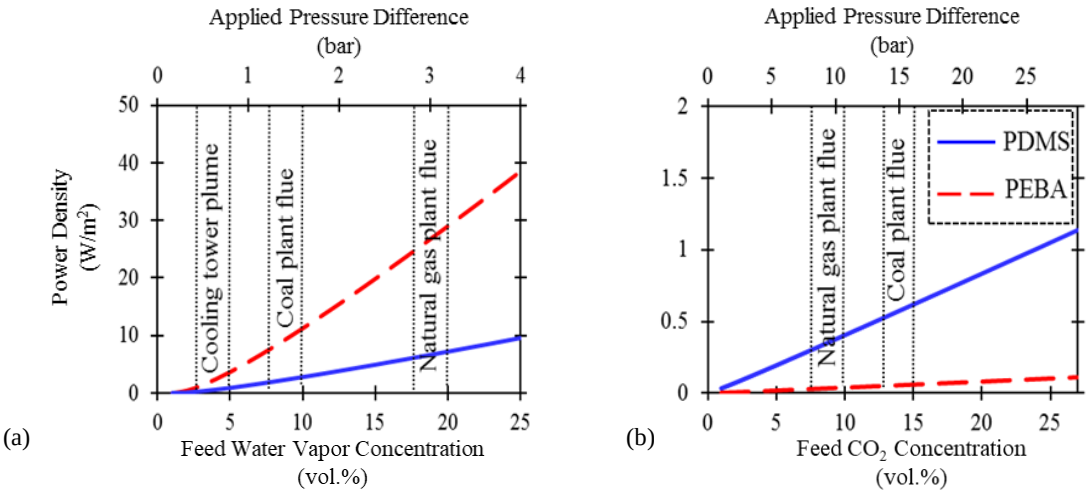

Figure 2.4. Maximum power can be obtained from the membrane permeation process by applying the appropriate pressure (load) on the sweep stream in response to the available concentration gradient. A range of (a) water vapor and (b) CO2 concentrations are shown, with concentrations of various sources highlighted. In all cases mixing occurs with ambient air at 1 vol.% water vapor and 0.03 vol.% CO2 at 20 °C. Polydimethylsiloxane (PDMS) is considered with water vapor permeability of BH2O = 40,000 barrer and CO2 permeability BCO2 = 3,000 barrer. Polyether block amide (PEBA) is considered with permeability of BH2O = 160,000 barrer and BCO2 = 300 barrer [40,47]. Membrane thickness is l = 55 μm.

Maximum power available over a range of water vapor and CO_2 feed concentrations is shown in Figure 2.4 (relative to ambient air at 1 vol.% water vapor and 0.03 vol.% CO_2). Power density of nearly 30 W/m^2 is again shown for the case where water vapor feed approaches 20 vol.% (as would be expected in natural gas-fired flue gas). The applied pressure required for maximum power is also shown. For the previously mentioned natural gas case, maximum power is obtained with reasonable applied pressure of 3 bar. This is within the structural limitations of current commercial membranes [48-50]. CO_2 permeation is again shown to generate much less power that water vapor, while also requiring application of much larger pressures on the order of 10 bar. Compression at such large pressures may be costly and even prohibitive (as discussed later in the Discussion section. This requirement for higher pressure is attributed to the larger CO_2 gradient (as described in equation (2.6)) while the lower power is attributed to the much lower membrane permeability to CO_2.

Achieving such power densities would require an ideal membrane that is perfectly selective, and an ideal process with very low recovery rates that mitigate spatial variations in concentration. The effects of such non-ideal phenomena are considered next.

2.3.3 Non-Ideal Transport Dynamics

Permeate flux and power from gas permeation are significantly influenced by several non-ideal effects that we introduce and analyze here. These include the effect of axial variations in concentration, the effect of reverse gas flux, and the effect of concentration polarization. Each of these dynamics is described in this section, and their influence on flux and power is illustrated with case studies.

2.3.4 Reverse Gas Flux

In the proposed gas permeation process, power is developed by the flux of species *i* towards the pressurized sweep stream as described in equation (2.7). However, because non-ideal membranes will exhibit imperfect selectivity, the leakage of other species *j* towards the feed stream will simultaneously act to reduce power. The volumetric flux of each species as observed from the sweep side can be described by the solution-diffusion model and assuming ideal gas behavior are given as (see Supplementary Note 2.4 for additional detail):

$$J_{i,S} = \frac{R\,T}{p_S}\frac{B_i}{l}\left(p_{i,F} - p_{i,S}\right) \tag{2.7}$$

$$J_{j,S} = \frac{R\,T}{p_S}\frac{B_i/l}{\alpha_{i/j}}\left(p_{j,S} - p_{j,F}\right) \tag{2.8}$$

α is the selectivity of the membrane, which is defined as the ratio of permeability *i* to permeability *j*.

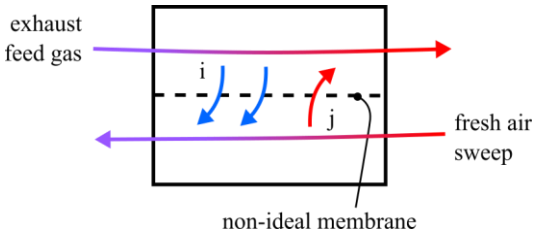

Figure 2.5. Reverse gas flux J_j away from the pressurized sweep stream is a non-ideal effect caused by limited selectivity in the membrane. The result is a reduction in power, as net flux (= $J_{i,S} - J_{j,S}$) towards the pressurized stream is reduced.

This phenomenon is known as reverse gas flux and is illustrated in Figure 2.5. We note that this phenomenon is observed in many other membrane processes including various sweep gas permeation processes [50,51], however in this case the dynamic is unique in that

reverse gas flux is exacerbated by the application of pressure to the sweep gas, leading to an increase in the reverse partial pressure gradient of j [52].

The net flux towards the sweep stream is therefore reduced to $J_{net} = J_{i,S} - J_{j,S}$, and a drop in power from the gas permeation process ensues. The effect of reverse gas permeate on net flux and power is illustrated in Figure 2.6, which shows the case of a binary gas mixture of nitrogen with 10 vol.% water vapor content, approximating the humidity of coal-fired flue gas. For a highly selective membrane such as PEBA with $\alpha_{H2O/N2} = 200{,}000$, little to no difference is observed as nitrogen leakage is negligible, and maximum power is maintained at 11.2 W/m^2. However, for a modestly selective material such as PDMS with $\alpha_{H2O/N2} = 140$, the maximum power point is significantly reduced from 2.8 W/m^2 from water vapor flux to 2.3 W/m^2 from net gas flux. The term $\dot{W}_{net}$ is introduced here and defined as power density from net gas flux and is distinguished from $\dot{W}_{H2O}$ which is power density from only water vapor flux.

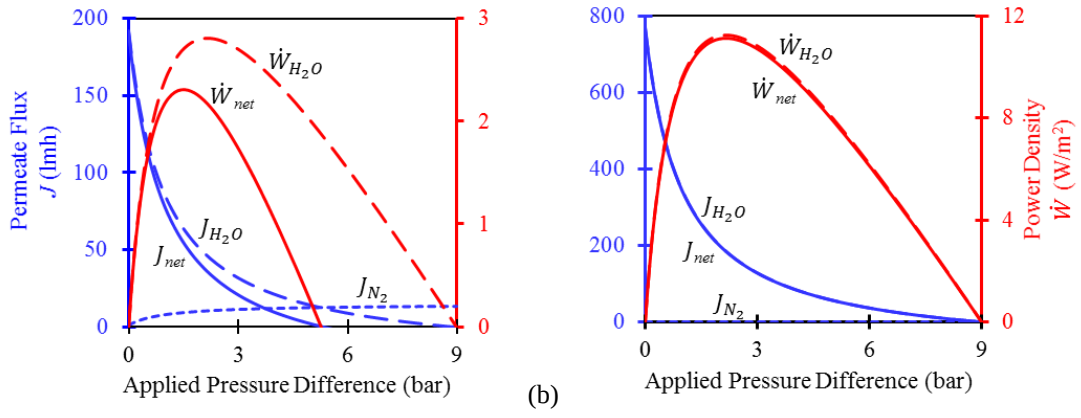

Figure 2.6. The effect of reverse nitrogen flux on net gas permeate towards the pressurized sweep stream, and on power density of the gas permeation process. Assuming binary gas mixture of nitrogen with 10 vol.% water vapor content approximating humidity in coal-fired flue gas, and sweep gas of ambient air at 1 vol.% water vapor at 20°C. Influence of membrane properties is illustrated with two cases: (a) polydimethyl siloxane (PDMS) with water vapor permeability of $B_{H2O} = 40{,}000$ barrer and nitrogen selectivity $\alpha_{H2O/N2} = 140$, and (b) polyether block amide (PEBA) with permeability of $B_{H2O} = 160{,}000$ barrer and selectivity $\alpha_{H2O/N2} = 200{,}000$ [40,47]. Membrane thickness is $l = 55$ μm.

When the effect of reverse gas permeate on power is considered, the solution for maximum power is reduced from equation (2.5) to the following equation (2.9). This expression is obtained analytically as an exact solution to $d\dot{W}_{net}/d\Delta p = 0$ (see Supplementary Note 2.4 for detailed solution).

$$\dot{W}_{net,max} = -R\,T\,\frac{B_i/l}{\alpha_{i/j}}\,p_F\,x_{i,F}\left(\frac{x_{i,S}}{x_{i,F}}\left(\alpha_{i/j} + \frac{1-x_{i,S}}{x_{i,S}}\right)\left(\sqrt{\frac{1-x_{i,F}(1-\alpha_{i/j})}{1-x_{i,S}(1-\alpha_{i/j})}}-1\right) + \left(\alpha_{i/j} + \frac{1-x_{i,F}}{x_{i,F}}\right)\left(\sqrt{\frac{1-x_{i,S}\,(1-\alpha_{i/j})}{1-x_{i,F}\,(1-\alpha_{i/j})}}-1\right)\right) \tag{2.9}$$

Where applied pressure for maximum power $\Delta p^{Wnet,max}$ is defined as,

$$\Delta p^{\dot{W}net,max} = p_F\left(\sqrt{\frac{1-x_{i,F}(1-\alpha_{i/j})}{1-x_{i,S}(1-\alpha_{i/j})}}-1\right) \tag{2.10}$$

Figure 2.7 shows the maximum power available from net flux (water vapor flux minus reverse flux of nitrogen) over a range of water vapor gradients. As compared to Figure 2.4 (a), we observe here a significant drop in power for the case of PDMS membrane, and only negligible change for the highly selective PEBA membrane.

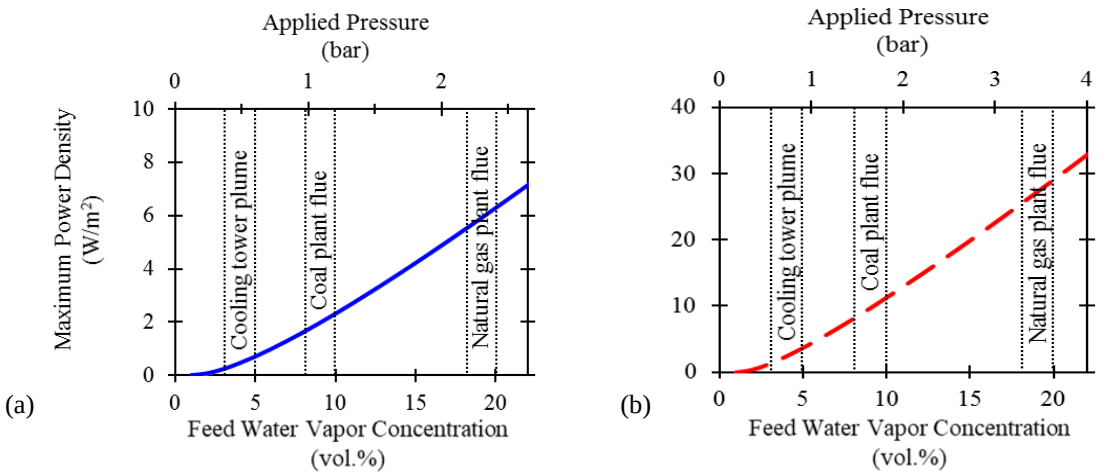

Figure 2.7. The effect of reverse nitrogen flux on net gas permeate towards the pressurized sweep stream, and on power density of the gas permeation process. Assuming binary gas mixture of nitrogen with 10 vol.% water vapor content approximating humidity in coal-fired flue gas and sweep gas of ambient air at 1 vol.% water vapor at 20°C. Influence of membrane properties is illustrated with two cases: (a) polydimethylsiloxane (PDMS) with water vapor permeability of B_{H2O} = 40,000 Barrer and nitrogen selectivity $\alpha_{H2O/N2}$ = 140, and (b) polyether block amide (PEBA) with permeability of B_{H2O} = 160,000 Barrer and selectivity $\alpha_{H2O/N2}$ = 200,000 [40,47]. Membrane thickness is l = 55 μm.

2.3.5 Concentration Polarization

As gas permeates across a dense membrane it accumulates at the surfaces of the material, forming a boundary layer characterized by a non-linear concentration profile [53]. This phenomenon of concentration polarization is illustrated in Figure 2.8. The result is a drop in the effective concentration difference and hence partial pressure driving force across the membrane, which thereby reduces gas flux. The severity of polarization is largely dependent on the diffusivity of the permeate species within the gas mixture, as well as the permeability of the membrane itself. For example, lower gas permeation and higher diffusivity of the species within the bulk stream will minimize polarization.

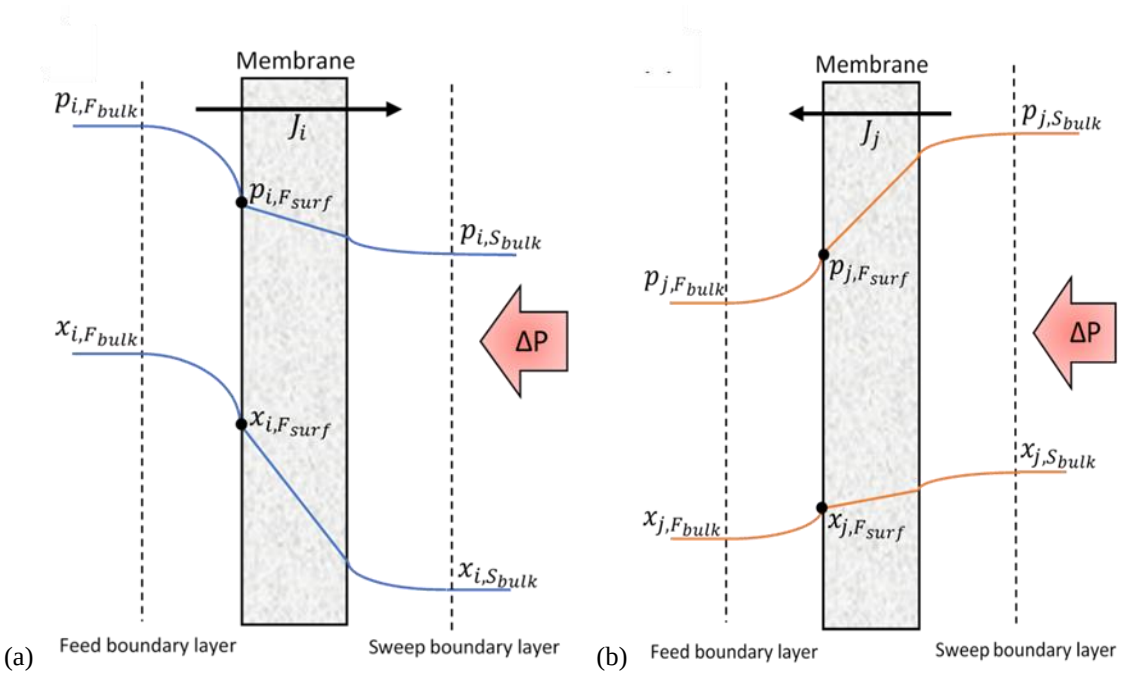

Figure 2.8. Illustration of concentration polarization of (a) gas species *i* and (b) gas species *j* across a dense gas permeation membrane. Non-linear concentrations gradient *x* are drawn across stagnant boundary layers at the feed and sweep membrane surfaces. The resulting partial pressure gradients *p* are drawn as a function of concentration as well as pressure applied to the sweep stream Δ*p*.

Concentration polarization is common to many mass transport phenomena and has been widely studied for permeation with sweep gases [46-47,52-54]. While the literature is extensive, the proposed gas permeation process is unique because rarely the sweep stream is pressurized, as it is in this case, so as to generate mechanical work. Pressurizing the sweep stream has the effect of exacerbating polarization. This is illustrated in Figure 2.8 which shows concentration and partial pressure gradients across the membrane and boundary layers. As shown, a drop in concentration difference across the boundary layer will translate to a more important drop in partial pressure difference when the sweep stream is pressurized. Applied pressure on the sweep stream, which is neglected in most gas permeation models, is considered in the polarization equations below.

The effect of polarization on flux can be determined by considering steady state mass conservation, in which case flux across the membrane is equal to flux through the boundary layers. For the case of a binary mix of gases *i* and *j*, the following expression describes volumetric flux through the boundary layers [46,54].

$$J_{i,S} = k_i \left(x_{i,F,bulk} - x_{i,F,surface}\right) + x_{i,F,bulk} \left(J_i - J_j\right) \tag{2.11}$$

$$J_{j,S} = k_i \left(x_{i,F,surface} - x_{i,F,bulk}\right) + \left(1 - x_{i,F,bulk}\right)\left(J_i - J_j\right) \tag{2.12}$$

Where *k* is the overall mass transfer coefficient at standard temperature T_o and pressure p_o.

The concentration of species *i* at the membrane surface $x_{i,F,surface}$ can then be obtained by considering equations (2.7,8,11 and 12) together (see Supplementary Note 2.5).

$$x_{i,F,surface} = x_{i,F,bulk} \left(\frac{k_i \frac{p_F}{R\,T} + \frac{B_i}{l}\, p_S \left(x_{i,S,bulk} \left(\frac{1}{\alpha_{i/j}} - 1 \right) + \frac{1}{\alpha_{i/j}} \left(\frac{p_F}{p_S} - 1 \right) + \frac{x_{i,S,bulk}}{x_{i,F,bulk}} \right)}{k_i \frac{p_F}{R\,T} + \frac{B_i}{l}\, p_F \left(1 + x_{i,F,bulk} \left(\frac{1}{\alpha_{i/j}} - 1 \right) \right)} \right) \tag{2.13}$$

For a binary gas mix of water vapor and nitrogen used in a hollow fiber membrane process, the overall mass transfer coefficient at standard temperature T_o = 273 K and pressure p_o = 1 bar can be estimated from [46,47]:

$$k_{H2O} = 0.0732 \frac{p}{p_o} \frac{T_o}{T} \frac{D_{H_2O}}{d_o^{0.4}} Re^{0.6}\, Sc^{0.33} \tag{2.14}$$

Where *Re* is the Reynolds number (= $d_h\, u\, /\, v$), *Sc* is the Schmidt number (= $v\, /\, D$), d_0 is the fiber outer diameter, d_h is the hydraulic diameter, *u* is the flow velocity, and *v* is the kinematic viscosity. *D* is the diffusivity of species *i* within the bulk stream, which for the case of water vapor in nitrogen gas is given by [55]:

$$D_{H_2O} = D_{o,H_2O}\left(\frac{p_o}{p}\right)\left(\frac{T}{T_o}\right)^{1.81} \quad (2.15)$$

Where $D_{o,H2O} = 2.178\times10^{-5}$ m^2/s at standard temperature T_o and pressure p_o [55].

Figure 2.9 illustrates the effect that polarization has on gas permeation power. Results are shown for the case of binary gas feed with 10 vol.% water vapors in nitrogen (approximating the water vapor content of coal-fired flue gas) and sweep gas of ambient air at 1 vol.% water vapor**.** Overall, we observe a drop in maximum power from 1.8 W/m^2 down to 0.8 W/m^2 for PDMS. For PEBA, the drop in maximum power from 11.2 to 2 W/m^2 is much more significant, due to high membrane permeability and selectivity.

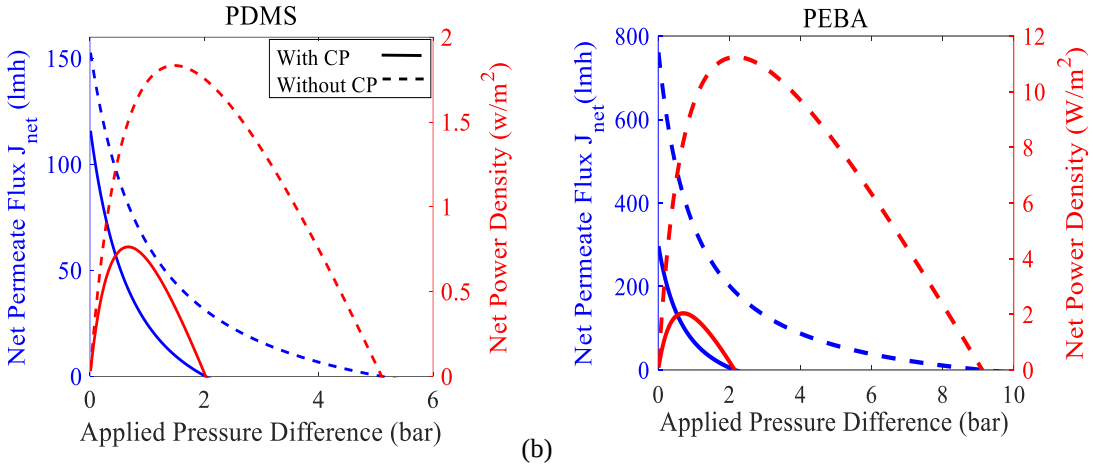

Figure 2.9. Effect of concentration polarization on the net permeate flux and power density for (a) polydimethylsiloxane (PDMS) membrane (water vapor permeability of B_{H2O} = 36,000 Barrer and nitrogen selectivity $\alpha_{H2O/N2}$ = 125) and (b) polyether block amide (PEBA) membrane (permeability of B_{H2O} = 160,000 Barrer and selectivity $\alpha_{H2O/N2}$ = 200,000). Membrane thickness is l = 55 μm. Assuming binary gas mixture of nitrogen with 10 vol.% water vapor content approximating humidity in coal-fired flue gas and sweep gas of ambient air at 1 vol.% water vapor at 20°C. Also, assuming inlet velocities are balanced at 4 cm/s.

Figure 2.9 also illustrates that polarization is more significant at higher applied pressure. This is because higher applied pressure has the effect of exacerbating polarization, as small concentration gradients at the sweep surface boundary layer will translate to magnified

partial pressure gradients. Additionally, the diffusion coefficient is inversely proportional to pressure as shown in equation (2.15), and therefore more severe polarization will be observed at higher pressure. The result is that maximum power point shifts to the left, such that for the cases considered the required pressure for maximum power is on the order of 1 bar.

2.3.6 Axial Dilution

The gas permeation process is also affected by axial variations in bulk stream concentrations as feed is diluted and sweep is enriched due to the accumulation of permeate. This dynamic is common to mass transfer as well as heat transfer systems [29,32].

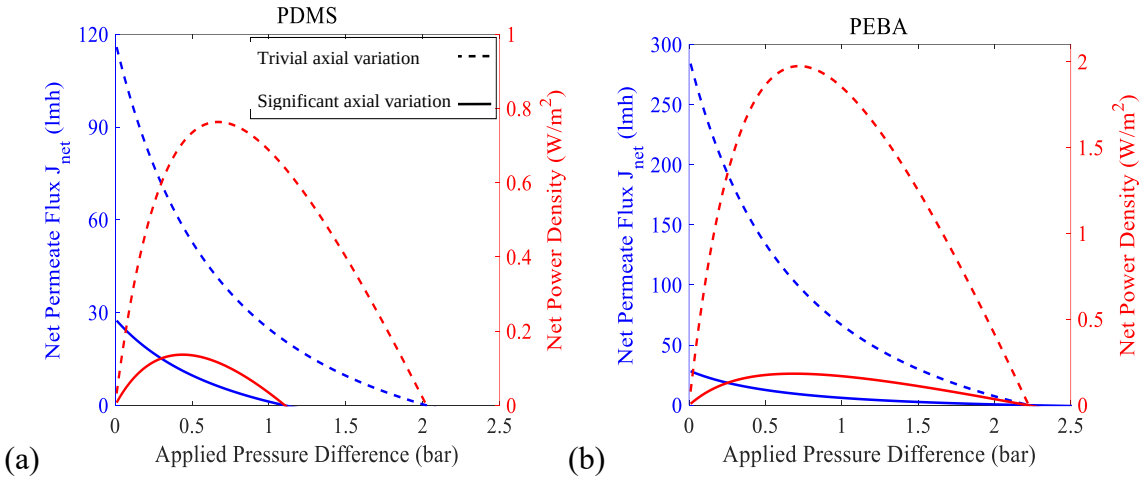

Figure 2.10. Effect of axial variations on the net permeate flux and net power density for (a) polydimethylsiloxane (PDMS) membrane (water vapor permeability of B_{H2O} = 36,000 Barrer and nitrogen selectivity $\alpha_{H2O/N2}$ = 125) and (b) polyether block amide (PEBA) membrane (permeability of B_{H2O} = 160,000 Barrer and selectivity $\alpha_{H2O/N2}$ = 200,000). Membrane thickness is l = 55 μm. Trivial axial variations (dashed line) are shown for case where bulk circulation volumes approach infinity, and membrane area is infinitesimal. The significant axial variation (solid line) include the effect of feed concentration change due to permeation obtained with finite element analysis when inlet feed and sweep flow rates are balanced $\dot{V}_F = \dot{V}_S$ = 1 lpm. Assuming binary gas mixture of nitrogen with 10 vol.% water vapor content approximating humidity in coal-fired flue gas and sweep gas of ambient air at 1 vol.% water vapor at 20°C.

Allowing feed and sweep circulation volumes to approach infinity, and selecting an infinitesimal membrane, makes axial variations trivial. However, in real practical cases, such as illustrated in Figure 2.10, axial variations can have a significant effect on net flux and power. In this paper, we employ a finite element mass balance approach to simulate axial variations under counter flow operation as further described in Section 2.4.2. [17,56,57]. For the case simulated in Figure 2.10, we observe a drop in power from 0.8 W/m^2 to 0.14 W/m^2 for PDMS, and from 2 W/m^2 to 0.19 W/m^2 for PEBA.

2.4 Methods and Materials

2.4.1 Experimental Analysis

Experimental validation was done using the custom laboratory test bench illustrated in Figure 2.11. The experimental setup consists of two gas lines, each equipped with mass flow controllers (Aalborg, Orangeburg, NY, ± 0.125 lpm) and supplied by compressed nitrogen cylinders (Praxair, Danbury, CT). One of the streams is humidified by circulating gas through a series of humidifying flasks containing deionized water. With this arrangement, humidity of the gas stream is able to approach saturation at room temperature. Water vapor content of the gas stream is precisely controlled by regulating mixing of parallel dry and humid streams. Relative humidity and temperature sensors (AM2315 i2C for Arduino, ± 2% RH and ± 0.3 °C) and pressure sensors (Cole-Parmer, Vernon Hills, IL, ± 62.21 Pa) were installed at each of the four membrane ports. A back-pressure regulator (Marsh Bellofram, Newell, WV) was used to control pressure applied to the sweep stream. A series of test trials were conducted during which permeate flux was evaluated in response to a range of applied pressures.

A summary of the test conditions is provided in Table 2.1. The bench was operated at room temperature (19 ± 0.3 °C) and membranes were supplied with nearly saturated (94.3 ± 2 % relative humidity) and nearly dry (0.1 ± 2 % relative humidity) nitrogen gas streams. Although this is the maximum water vapor gradient that can be established at room temperature, it nonetheless represents fairly conservative conditions with partial pressure gradients of only 2.1 kPa. Volumes of feed and sweep streams were balanced at rates of 1 ± 0.125 lpm and circulated through the membrane module in counter flow arrangement.

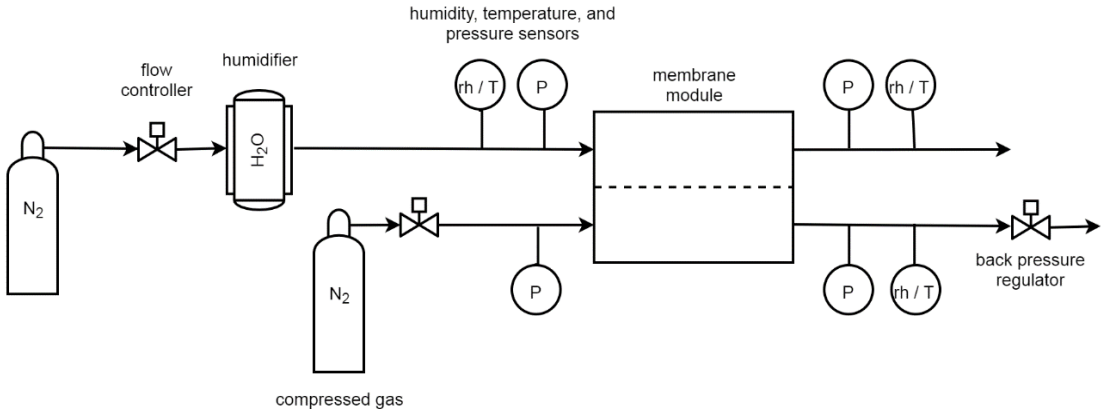

(a)

(b)

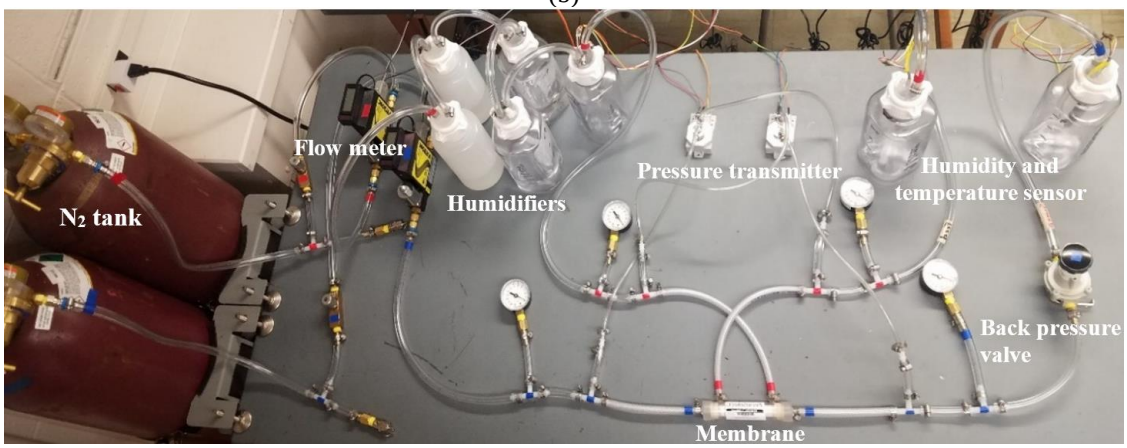

Figure 2.11. (a) Schematic and (b) picture showing the gas permeation laboratory test bench. Compressed nitrogen gas is supplied to each side of the membrane module. One stream is humidified through a series of flasks, approaching saturation at room temperature, while the other is kept dry. Humidity and temperature sensors are used to measure inlet and outlet conditions. Mass flow controller and back-pressure regulator are used to control operating conditions.

Table 2.1. Test conditions

Test Operating Conditions	
Temperature	19 ± 0.3 °C
Feed and sweep flow	1 ± 0.125 lpm
Feed stream relative humidity	94.3 ± 2 %
Sweep stream relative humidity	0.1 ± 2 %
Flow orientation	Counter flow

A commercially available PDMS membrane with hollow fiber configuration was selected for proof-of-concept testing. The homogeneous silicone-based dense membrane is characterized by high water vapor permeability B_{H2O} = 36,000 barrer and modest selectivity $\alpha_{H2O/N2}$ = 125.

Table 2.2. Membrane parameters

Membrane Characteristics	
Membrane material	polydimethylsiloxane (non-porous dense)
Module type	hollow fiber
Membrane surface area ***A***	0.1 m^2
Module length	16 cm
Fiber outer diameter	300 μm
Fiber wall thickness ***l***	55 μm
Number of fibers	1280
Water vapor permeability B_{H2O}	36,000 Barrer
Selectivity $\alpha_{H2O/N2}$	125
Maximum transmembrane pressure	3 bar applied to fiber 1 bar applied to shell

Key membrane specifications provided by the manufacturer (PermSelect, Ann Arbor, MI) are summarized in Table 2.2.

Water vapor flux across the membrane was evaluated using a mass balance approach and assuming ideal gas behavior. Using feed side measurements of humidity, temperature, pressure, and flow rate, the molar permeate flux $\Delta\dot{n}$ is obtained from the following expression.

$$\Delta\dot{n}_{H_2O} = \frac{p_F \dot{V}_{F,in}}{R\,T}\left(\frac{x_{F,in}}{1-x_{F,in}} - \frac{x_{F,out}}{1-x_{F,out}}\right) \tag{2.16}$$

The same result should be obtained by considering the mass balance of the sweep stream water vapor. To verify, the following expression for permeate is obtained based on humidity, temperature, pressure, and flow rate measurements from the sweep stream.

$$\Delta\dot{n}_{H_2O} = \frac{p_S \dot{V}_{S,in}}{R\,T}\left(\frac{x_{S,out}}{1-x_{S,out}} - \frac{x_{s,in}}{1-x_{S,in}}\right) \tag{2.17}$$

Change in the water vapor volume $\Delta\dot{V}$ observed from the sweep side is then obtained from this mass balance and can be normalized over membrane surface area *A* to give flux *J*.

$$J_{H_2O,S} = \frac{\Delta\dot{V}_{H2O,S}}{A} = \frac{R\,T}{p_S}\frac{\Delta\dot{n}_{H_2O}}{A} \tag{2.18}$$

2.4.2 Numerical Analysis

Experimental results were validated against the theoretical model previously described in Section 2.3, and simulation was then used to extend analysis to other membrane materials and test conditions. As discussed, the model assumes ideal gas behavior and considers transport dynamics including axial variations in concentration, reverse gas flux, and concentration polarization. The model was implemented in Matlab software using a

finite element approach, wherein conservation of mass was applied to each element to consider variations in concentration and flow [17,53,57]. Obtaining a solution for counter-flow operation involved an iterative numerical approach. A summary of the key parameters and assumptions included in the simulation is provided in Table 2.3. Default conditions for the simulation were based on membrane geometry and operating conditions from the experimental trials previously described in Section 2.4.1.

Table 2.3. Simulation parameters*

Gas Properties		
Kinematic viscosity ν (m^2/s)	15.3×10^{-6}	
Standard diffusivity $D_{o,H2O}$ (m^2/s)	2.178×10^{-5}	
Membrane Characteristics [34,35]	polydimethylsiloxane (PDMS)	polyether block amide (PEBA)
Permeability B_{H2O} (Barrer)	36,000	160,000
Selectivity $\alpha_{H2O/N2}$	125	200,000

*Unless specified, default simulation parameters match experimental conditions specified in Section 3.1.

2.5 Results and Discussion

2.5.1 Experimental Demonstration under Conservative Conditions

Experimental results from gas permeation against an applied pressure are summarized in Figure 2.12. Generation of mechanical work in the form of an expanding volume of pressurized gas is successfully observed. Up to 57 mW/m^2 of power is experimentally recorded, for the case where volumetric water vapor flux 1.8 $l/m^2/h$ is observed from the sweep stream that is pressurized to 1.2 bar above feed. This is near the maximum water vapor power predicted by simulation, which is 63 mW/m^2 at 2 bar applied pressure. As

shown, the simulation results show reasonable agreement with experimental data. Figure 2.12 also shows the result of reverse nitrogen flux from the sweep towards the feed stream. This leakage leads to a drop in the net volume of sweep gas, and hence the net power density produced by the gas permeation process.

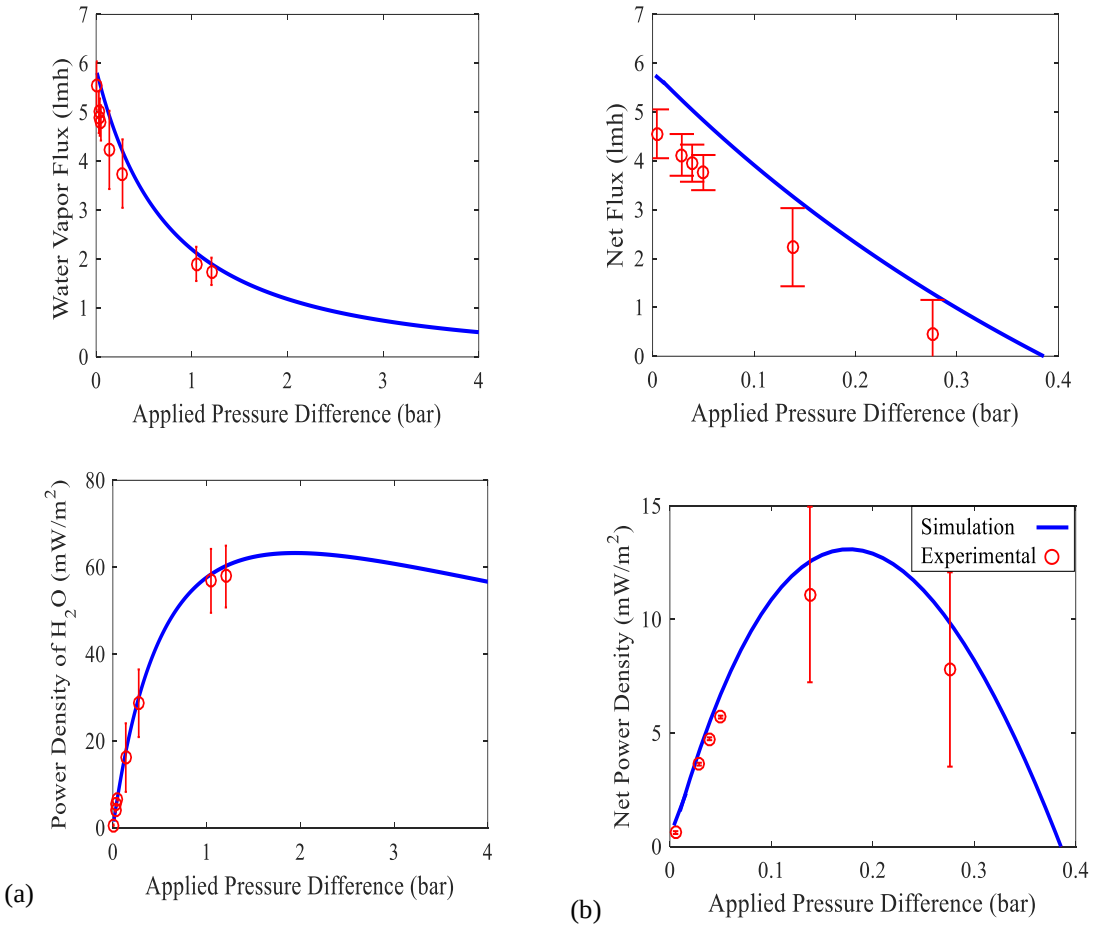

Figure 2.12. (a) Water vapor flux and (b) power density from water vapor permeation across a polydimethylsiloxane (PDMS) membrane supplied by humid feed (2 vol.% water vapor in pure nitrogen at T= 19°C) and dry sweep. Experimental results are identified by red data points and simulation results by solid blue lines. Test and simulation conditions are summarized in Tables 2.1. and 2.3.

As shown, maximum of only 13 mW/m^2 of net power remains once this is considered. Experimentally, maximum net power of 11.5 mW/m^2 was observed at applied pressure of 0.14 bar above feed. The significant drop in power illustrated between Figures 2.12. (a) and 2.12 (b) occurs as a result of the modest membrane selectivity of PDMS $\alpha_{H2O/N2} = 125$.

Low membrane selectivity is exacerbated in this process by the application of pressure to the sweep stream, thereby favoring reverse nitrogen flux. Using highly selective membranes can effectively mitigate this non-ideal dynamic and allow for net flux to approach water vapor flux. This is illustrated in Figure 2.13, which shows power density for the simulated case of highly selective PEBA membrane ($\alpha_{H2O/N2}$ = 200,000) and compares results against the experimentally verified PDMS case.

As shown, the curve for power density from net flux approaches the curve for power from water vapor flux. Net power of up to 73 mW/m^2 is expected from application of PEBA membrane to the feed and sweep streams specified.

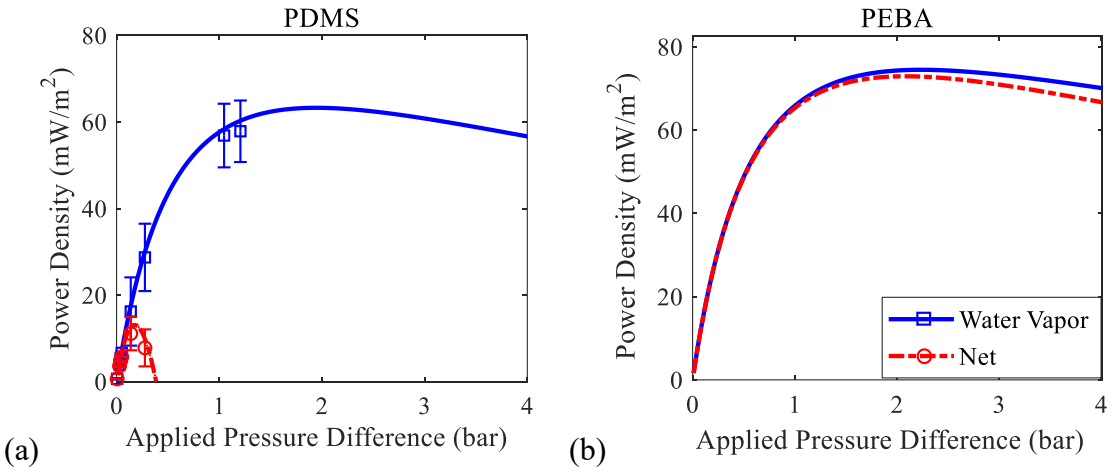

Figure 2.13. Power density from water vapor permeation (solid blue curve with square date points) and net gas permeation (hatched red curve with circle data points) across (a) polydimethylsiloxane (PDMS) membrane and (b) a polyether block amide (PEBA) membrane. Test and simulation conditions are summarized in Tables 2.1 and 2.3.

2.5.2 Expected Performance under Range of Conditions

The experimental results reported in Section 2.5.1 demonstrate the concept of generating mechanical work from gas permeation, however the scenarios considered are by no means optimal. While many variables can be considered for improved performance, in this section we provide a brief illustration of the potential for the process when operated with higher concentration gradients.

As mentioned previously, the feed and sweep streams used in our laboratory experiments involved relatively modest water vapor of only 2 vol.%, equivalents to partial pressure of less than 2.1 kPa. By contrast the water vapor content observed in natural gas-fired exhaust (~ 20 %) and coal-fired exhaust (~ 10 %), and cooling tower vapor concentration (~ 5 %) are much greater. Even slightly expanding the water vapor capacity of gas can lead to significant improvements in power density, however our conservative test conditions were necessary due to limitation of operating at room temperature with current laboratory equipment.

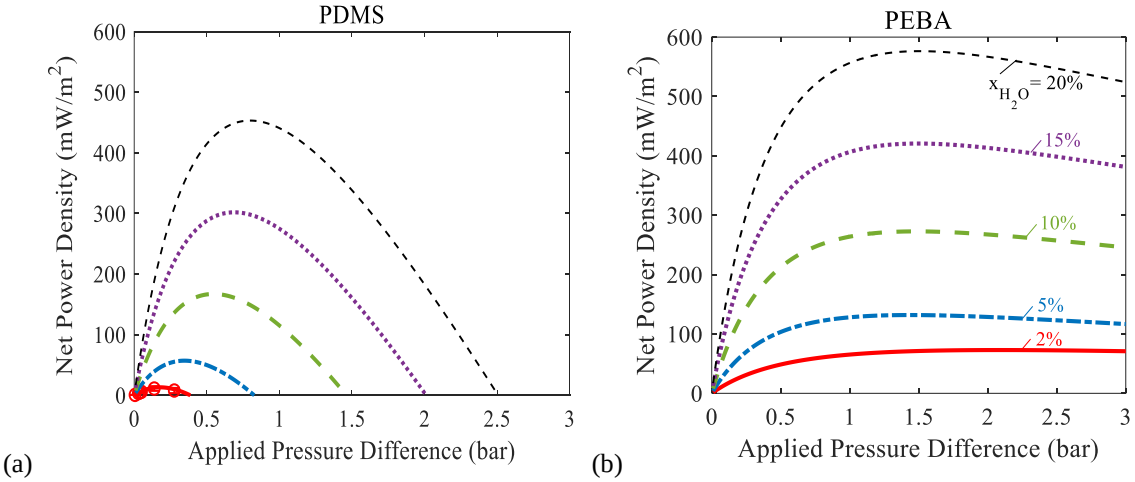

Figure 2.14. Power density from net gas permeation across (a) a polydimethylsiloxane (PDMS) membrane and (b) a polyether block amide (PEBA) membrane, given a range of water vapor feed concentrations between 2 and 20 vol.%. Test and simulation conditions are summarized in Tables 2.1 and 2.3.

Figure 2.14 shows simulation results for power density from net flux expected from the bench system given supply of high concentration feed. As feed approaches 20 vol.% we observe an almost 10 times increase in power density relative to the 2 vol.% case tested in the laboratory. Again, we also observe the advantages of high permeability and selectivity demonstrated with the PEBA membrane. Maximum power density of nearly 600 mW/m^2 is expected for the case of high humidity feed circulated through PEBA membrane system with dry sweep pressurized to 1.5 bar above feed.

2.5.3 Design Considerations

The overall energy recovered from the pressurized sweep gas process will be the difference between the energy recovered from the permeate gas, and the energy required to operate the compressor and to circulate feed and sweep through the membrane module. This energy balance is illustrated in Figure 2.15, with a case study showing application of the process to the flue gas of a 1 MW coal-fired power plant. The plant produces 3,000 m^3/h of exhaust at 50 °C, 10 vol.% water vapor concentration, and atmospheric pressure. This feed gas is supplied to a 2,000 m^2 PDMS membrane system along with fresh outdoor air available at 20 °C and 0.5 vol.% humidity, which is used as sweep gas.

As shown in figure 2.15, the sweep is sent to an adiabatic compressor to increase the sweep pressure up to 1 bar above atmosphere before entering the membrane. The power required by the compressor is about 55 kW using a single stage compressor with 80% efficiency [58,59]. Based on the validated simulation results, net volumetric flux of 2.7×10^{-2} $m^3/h/m^2$ is anticipated on the sweep side pressurized to 1 bar above atmosphere. The resulting humid pressurized sweep gas (6 vol.% humidity) is then delivered to the turbine, from which work is recovered, after which gas is exhausted to the environment at an

expanded volume of 3,050 m^3/h, 24 °C, 3 vol.% humidity, and atmospheric pressure. Considering an adiabatic operation across the single stage turbine and assuming 80 % mechanical efficiency, an output power of 72 kW is estimated. The overall energy balance of the process is summarized in Figure 2.15 and yields 5 kW or roughly 0.5 % of power plant capacity.

While it is beyond the scope of this study to optimize the operating conditions and membrane sizing of the system, this example does provide insight into the potential of this new concept. To achieve the most favorable energy balance possible, it is necessary to minimize friction through the membrane module such that pressure drop is negligible, and parasitic loads on the blower and compressor are minimized. Achieving this requires careful consideration of the operating volumes because while processing small volumes of gas with large membranes will mitigate friction, other non-ideal effects will be exacerbated, such as polarization and axial dilution as mentioned previously. These tradeoffs have been investigated for analog processes [18,56].

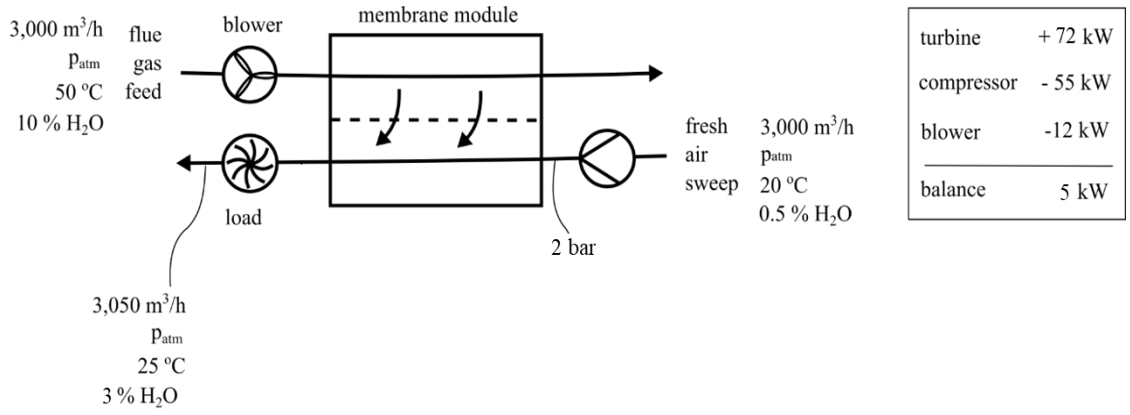

Figure 2.15. Process flow diagram and energy balance for the sweep gas energy recovery system applied to the flue gas of a 1 MW coal-fired power plant.

In addition, maximizing energy requires high efficiency rotating machines. Operating at approximately 1-3 bar of applied pressure, as suggested throughout this study, is non-trivial for compression machinery, and may be costly. The energy supplied to the compressor can theoretically be recovered by the turbine, however in practice each machine will have associated losses. To reduce such losses, a design variation of the system may include a pressure exchanger for more efficient recycling of compressor energy, however at applied pressures around 1-3 bar such exchangers tend to have low efficiency [60]. Alternatively, Figure 2.16 shows a design variation that does not involve a compressor. Rather, sweep gas is used to draw permeate through a turbine and across a membrane, from a feed stream that is maintained under vacuum. The advantages of operating gas permeation processes under compression or vacuum have been previously considered for other applications and require further investigation for this case [9]. These design considerations provide insight into avenues for future research and development, and we anticipate that optimized designs will be specific to individual applications.

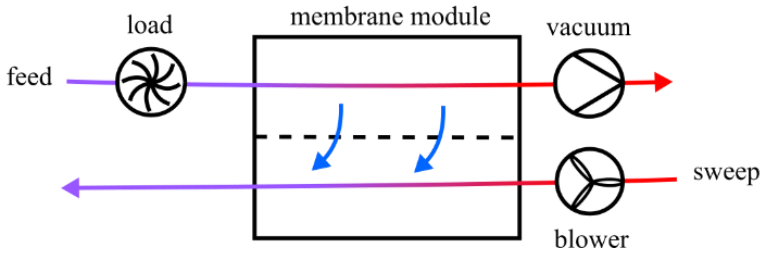

Figure 2.16. Design variations for the sweep gas power generating process can be considered in future work and may offer advantages for certain applications. For example, this alternative (b) generates power by using drawing permeate gas from a vacuum feed source.

2.6 Conclusions

This study introduces and experimentally validates the novel concept of using gas permeation to generate mechanical power in the form of compressed gas flow. Using a

commercial PDMS membrane and modest water vapor gradients of 2 vol.% concentration, we observe power density of 57 mW/m^2 from water vapor flux, and power density of 11.5 mW/m^2 from net gas flux, at low applied pressures of 1 bar or less. These results provide the first ever demonstration of power from membrane-based gas permeation with gas concentration gradients.

A finite element mass transport model is described and validated against the experimental data. This model is used to illustrate the significance of membrane permeability and selectivity, as well as feed concentration, on power density. Simulation results indicate an order of magnitude improvement in power (nearly 600 mW/m^2) when highly permeable and selective PEBA membranes are supplied with feed at 20 vol.% water vapor. Nevertheless, whether such power densities are sufficient to justify capital investment remains questionable.

Our motivation in introducing this concept to the extensive gas permeation literature, is that it may lead to further innovation related to energy efficiency and sustainability. For example, thermodynamic analysis suggests that energy limits of gas concentration gradients from certain power plant exhaust, represents 1-2 % of power capacity. Such application however would require further consideration of multi-gas transport dynamics and membrane material stability. In addition, heat transfer dynamics between hot exhaust feed and cool ambient sweep must be considered, especially in cases such as water vapor where phase change dynamics may be significant.

2.7 Acknowledgment

Research reported in this publication was supported in part by funding provided by DTE Energy Co. under the E-Challenge program. We also acknowledge Graduate Fellowships to Sarah Moussaddy and Gucheng Yuan made by the School of Engineering and Computer Science, Oakland University.

2.8 Nomenclature

A	membrane surface area (m^2)
B	membrane permeability (Barrer)
D	diffusivity ($m^2\ s^{-1}$)
d_o	Fiber outer diameter (m)
d_h	hydraulic diameter (m)
G	Gibbs Energy (J)
J	permeate flux ($l\ m^{-2}\ h^{-1}$)
k	mass transfer coefficient (m/s)
l	membrane thickness (m)
m	mass (kg)
n	Number of mol (mol)
p	pressure (Pa)
R	gas constant ($J\ mol^{-1}\ K^{-1}$)
Re	Reynold Number
Sc	Schmidt number
T	temperature (K)
u	velocity ($m\ s^{-1}$)
V	volume (m^3)
$\dot{W}$	power density (W/m^2)
x	mole fraction

Greek symbols:

α	membrane selectivity
γ	partial pressure ratio
β	mixing ratio
v	kinematic viscosity (m^2/s)

Subscripts:

i	gas species i
j	gas species j
S	sweep side
F	feed side

2.9 Supplementary Notes

2.9.1 Supplementary Note 2.1: Limits to Energy Recovery

The Gibbs energy of mixing solutions is defined by the change in Gibbs energy from initial to final state.

$$\Delta G = G_{final} - G_{initial} \tag{S2.1}$$

Where the initial potential of feed *F* and sweep *S* mixtures of binary gases can be defined as:

$$\begin{aligned} G_{initial} = \sum G^{o}_{i,initial} \\ + R\,T\left(n_{i,F,initial}\ln\left(p_{i,F,initial}\right) + n_{j,F,initial}\ln\left(p_{j,F,initial}\right)\right. \\ \left. + n_{i,S,initial}\ln\left(p_{i,S,initial}\right) + n_{j,S,initial}\ln\left(p_{j,S,initial}\right)\right) \end{aligned} \tag{S2.2}$$

And the final potential of these same gas streams can be defined as:

$$G_{final} = \sum G^{o}_{I,final} + R\,T\left(n_{I,F,final}\ln\left(p_{I,F,final}\right) + n_{j,F,final}\ln\left(p_{j,F,final}\right) + n_{I,S,final}\ln\left(p_{I,S,final}\right) + n_{j,S,final}\ln\left(p_{j,S,final}\right)\right) \quad \text{(S2.3)}$$

G^o is the reference Gibbs energy at standard conditions, R is the gas constant, T is the absolute temperature, p_i and p_j are the partial pressures of species i and j, and n_i and n_j are the amounts of species i and j.

The Gibbs energy of mixing can then be written as was shown in eq. (1) of Section. 2.2. given the following assumptions (1) mixing occurs across a perfectly selective membrane that is impermeable to species j, such that $n_{j,F,initial} = n_{j,F,final}$ and $n_{j,S,initial} = n_{j,S,final}$; (2) the diluted sweep stream is infinitely large such that $p_{j,S,initial} = p_{j,S,final}$; and (3) the mixing process is allowed to process towards equilibrium, such that $p_{i,F,final} = p_{i,S,final}$.

$$\frac{\Delta G}{RT} = -\left(x_{i_{F_{in}}}.n_{F_{in}}\ln\left(\frac{x_{i_{F_{OUT}}}}{x_{i_{F_{IN}}}}\right) + x_{i_{S_{in}}}.n_{S_{in}}\ln\left(\frac{x_{i_{S_{OUT}}}}{x_{i_{S_{IN}}}}\right)\right) \quad (2.1)$$

The energy per unit of species i contained in the concentrated stream is then,

$$\frac{\Delta G}{n_{i,F,initial}} = R\,T\left(\ln\left(\frac{p_{i,F,initial}}{p_{i,F,final}}\right) + \frac{n_{i,S,initial}}{n_{i,F,initial}}\ln\left(\frac{p_{i,S,initial}}{p_{i,S,final}}\right)\right) \quad \text{(S2.4)}$$

Neglecting friction through the energy conversion system such that the mixing process occurs at constant pressure $p_F = p_S$,

$$\frac{\Delta G}{n_{i,F,initial}} = R\,T\left(\ln\left(\frac{p_{i,F,initial}}{p_{i,F,final}}\right) + \frac{n_{S,initial}}{n_{F,initial}}\frac{p_{i,S,initial}}{p_{i,F,initial}}\ln\left(\frac{p_{i,S,initial}}{p_{i,S,final}}\right)\right) \quad \text{(S2.5)}$$

The Gibbs energy per unit feed can then be written in terms of initial concentrations and pressures, as defined by $\gamma = p_{i,F,initial} / p_{i,S,initial}$, and $\beta = n_{S,initial} / n_{F,initial}$.

$$\frac{\Delta G}{n_{i,F,initial}} = R\,T\left(\ln\gamma + \left(\frac{\beta}{\gamma}+1\right)\ln\left(\frac{x_{i,S,initial}}{x_{i,S,final}}\right)\right) \quad \text{(S2.6)}$$

$$\frac{\Delta G}{n_{i,F,initial}} = R\,T\left(\ln\gamma + \left(\frac{\beta}{\gamma}+1\right)\ln\left(\frac{n_{i,S,initial}\,n_{S,final}}{n_{S,initial}\,n_{i,S,final}}\right)\right) \quad \text{(S2.7)}$$

As the mixing process reach equilibrium at the end, the total inlet concentration will mix to have at the end equal concentration on both sides.

$$\frac{\Delta G}{n_{i,F,initial}} = R\,T\left(\ln\gamma + \left(\frac{\beta}{\gamma}+1\right)\ln\left(\frac{1+\beta}{\gamma+\beta}\right)\right) \quad \text{(S2.8)}$$

We note that this expression has previously been reported in the literature [11]. Gibbs energy can finally be normalized per unit volume of rich feed exhaust to obtain equation (2.2) as reported in Section 2.3.1.

$$\frac{\Delta G}{V_{F,initial}} = p_F\,x_{i,F,initial}\left(\ln\gamma + \left(\frac{\beta}{\gamma}+1\right)\ln\left(\frac{1+\beta}{\gamma+\beta}\right)\right) \quad \text{(2.2)}$$

2.9.2 Supplementary Note 2.2: Gas Concentrations of Common Sources

The concentration of water vapor and CO_2 in several common exhaust streams are considered throughout the paper. The assumed values for these sources are summarized in Table S2.1.

Table S2.1. Concentration of water vapor and CO_2 in common gas streams

Feed Source	Concentration (vol.%)		Sweep Source	Concentration (vol.%)	
	H_2O	CO_2		H_2O	CO_2
Coal-fired flue gas	10	14	Ambient air (typical day)	1	0.03
Natural gas-fired flue gas	20	10			
Cooling tower plume	4.5	0.04			
Passenger car exhaust	13	14			
Human respiration	6.7	4			
Ambient air (humid day)	4.5	0.03	Building exhaust	1	0.03

2.9.3 Supplementary Note 2.3: Ideal Maximum Power

From solution-diffusion model, molar permeate flux $\dot{n}$ of species i across a dense membrane with permeability B_i is driven by the partial pressure gradient of that species Δp_i [45].

$$\Delta \dot{n}_i = \frac{B_i}{l} \Delta p_i \tag{S2.9}$$

Assuming ideal gas behavior, the associated volumetric flux observed on the sweep side at pressure p_S can be written as eq. (2.4) (as stated in Section 2.3.2.).

$$J_{i,S} = \frac{R\,T}{p_S} \frac{B_i}{l} \Delta p_i \tag{2.4}$$

Where R is the gas constant and T is the absolute temperature.

Power density is then the product of this volumetric flux and the pressure applied to the sweep side $\Delta p = p_S - p_F$ (as stated in eq. (2.3) from Section 2.3.2.).

$$\dot{W}_i = J_{i,S} \Delta p \tag{2.3}$$

Combining eqs. (2.3) and (2.4) power density from permeation of gas species i across a dense membrane can be written as follows,

$$\dot{W}_i = \frac{R\,T}{p_S} \frac{B_i}{l} \Delta p_i \Delta p \tag{S2.10}$$

$$\dot{W}_i = \frac{R\,T}{p_S} \frac{B_i}{l} \left(p_F\, x_{i,F} - p_S\, x_{i,S}\right) \Delta p \tag{S2.11}$$

Maximum power density $\dot{W}_{i,max}$ from the gas permeation process can be then be obtained from the exact solution to $d\dot{W}_i / d\Delta p = 0$.

$$\frac{d\,\dot{W}_i}{d\,\Delta p} = \frac{d}{d\,\Delta p} R\,T\, \frac{B_i}{l} \left(\frac{p_F\, \Delta p}{p_F + \Delta p}\, x_{i,F} - \Delta p\, x_{i,S} \right) \tag{S2.12}$$

$$0 = \mathrm{R\,T}\,\frac{\mathrm{B_i}}{l}\left(\frac{{\mathrm{p_F}}^2}{(\mathrm{p_F}+\Delta\mathrm{p})^2}\mathrm{x_{i,F}} - \mathrm{x_{i,S}}\right) \tag{S2.13}$$

We therefore obtain the solution for applied pressure that satisfies the condition for maximum power, as stated in Section 2.3.2. eq. (2.6).

$$\Delta\mathrm{p}^{\dot{\mathrm{W}}_{i,max}} = \mathrm{p_F}\left(\sqrt{\frac{\mathrm{x_{i,F}}}{\mathrm{x_{i,S}}}} - 1\right) \tag{2.6}$$

Substituting the result for applied pressure eq. (2.6) into the expression for power eq. (S2.11) gives the maximum power that can be obtained from gas permeation across a given membrane, as stated in Section 2.3.2. eq. (2.5).

$$\dot{\mathrm{W}}_{\mathrm{i,max}} = \mathrm{R\,T}\,\frac{\mathrm{B_i}}{l}\,\mathrm{p_F}\left(\sqrt{\mathrm{x_{i,F}}} - \sqrt{\mathrm{x_{i,S}}}\right)^2 \tag{2.5}$$

2.9.4 Supplementary Note 2.4: Reverse Gas Flux

For binary mixtures of gas, mass diffusion of species *i* and *j* across a polymeric dense membrane is described by Fick's Law modified in the solution-diffusion model [45].

$$\Delta\dot{\mathrm{n}}_\mathrm{i} = \frac{\mathrm{B_i}}{l}\,\Delta\mathrm{p_i} \tag{S2.14}$$

$$\Delta\dot{\mathrm{n}}_\mathrm{j} = \frac{\mathrm{B_i}/l}{\alpha_{\mathrm{i/j}}}\,\Delta\mathrm{p_j} \tag{S2.15}$$

Where $\alpha_{i/j}$ is the ratio of membrane permeability *i* to permeability *j*.

The net flux across the membrane is then the difference between species *i* and *j*, and can be expressed as volumetric flux observed from the pressurized sweep side by assuming ideal gas behavior.

$$\mathrm{J_{net,S}} = \mathrm{J_{i,S}} - \mathrm{J_{j,S}} \tag{S2.16}$$

$$J_{i,S} = \frac{R\,T}{p_S}\frac{B_i}{l}\left(p_{i,F} - p_{i,S}\right) \tag{S2.17}$$

$$J_{j,S} = \frac{R\,T}{p_S}\frac{B_i/l}{\alpha_{i/j}}\left(p_{j,S} - p_{j,F}\right) \tag{S2.18}$$

The net power is then the result of net volumetric flux observed from the pressurized sweep stream.

$$\dot{W}_{net} = J_{net,S}\,\Delta p \tag{S2.19}$$

When eqs. (S2.16) to (S2.19) are combined, net power density can be stated as,

$$\dot{W}_{net} = \frac{R\,T}{p_S}\frac{B_i}{l}\left(\left(x_{i,F}\,p_F - x_{i,S}\,p_S\right) - \frac{1}{\alpha_{i/j}}\left(\left(1-x_{i,s}\right)p_S - \left(1-x_{i,F}\right)p_F\right)\right)\Delta p \tag{S2.20}$$

$$\dot{W}_{net} = \frac{R\,T}{(p_F+\Delta p)}\frac{B_i}{l}\left(\left(x_{i,F}\,p_F - x_{i,S}\,(p_F+\Delta p)\right) - \frac{1}{\alpha_{i/j}}\left(\left(1-x_{i,s}\right)(p_F+\Delta p) - \left(1-x_{i,F}\right)p_F\right)\right)\Delta p \tag{S2.21}$$

Now the maximum power that can be obtained from the non-ideal permeation process $\dot{W}_{net,max}$ can be determined analytically by considering $d\dot{W}_{net} / d\Delta p = 0$.

$$\frac{d\,\dot{W}_{net}}{d\,\Delta p} = \frac{d}{d\,\Delta p}R\,T\,\frac{B_i}{l}\left(x_{i,F}\,p_F\,\frac{\Delta p}{(p_F+\Delta p)} - x_{i,S}\,\Delta p - \frac{\left(1-x_{i,s}\right)}{\alpha_{i/j}}\Delta p + \frac{\left(1-x_{i,F}\right)p_F}{\alpha_{i/j}}\frac{\Delta p}{(p_F+\Delta p)}\right) \tag{S2.22}$$

$$0 = R\,T\,\frac{B_i}{l}\left(x_{i,F}\,\frac{{p_F}^2}{(p_F+\Delta p)^2} - x_{i,S} - \frac{\left(1-x_{i,s}\right)}{\alpha_{i/j}} + \frac{\left(1-x_{i,F}\right)}{\alpha_{i/j}}\frac{{p_F}^2}{(p_F+\Delta p)^2}\right) \tag{S2.23}$$

Thus, we obtain an exact solution for the applied pressure that satisfies maximum net power density (as shown in eq. (2.10) Section 2.3.3.1.).

$$\Delta p^{\dot{W}net,max} = p_F \left(\sqrt{\frac{1 - x_{i,F}\left(1 - \alpha_{i/j}\right)}{1 - x_{i,S}\left(1 - \alpha_{i/j}\right)}} - 1 \right) \tag{2.10}$$

Substituting eq. (2.10) in (S2.21) we obtain the solution for maximum power that can be obtained from net flux of species *i* and *j* across a gas permeation membrane (as shown in eq. (2.9) Section 2.3.1.).

$$\begin{aligned} \dot{W}_{net,max} = -R\,T\,\frac{B_i/l}{\alpha_{i/j}}\,p_F\,x_{i,F}\Bigg(& \frac{x_{i,S}}{x_{i,F}}\Bigg(\alpha_{i/j} \\ & + \frac{1 - x_{i,S}}{x_{i,S}}\Bigg)\left(\sqrt{\frac{1 - x_{i,F}\left(1 - \alpha_{i/j}\right)}{1 - x_{i,S}\left(1 - \alpha_{i/j}\right)}} - 1 \right) \\ & + \left(\alpha_{i/j} + \frac{1 - x_{i,F}}{x_{i,F}} \right)\left(\sqrt{\frac{1 - x_{i,S}\left(1 - \alpha_{i/j}\right)}{1 - x_{i,F}\left(1 - \alpha_{i/j}\right)}} - 1 \right)\Bigg) \end{aligned} \tag{2.9}$$

2.9.5 Supplementary Note 2.5: Concentration Polarization

The effect of polarization on flux can be determined by considering steady state mass conservation, in which case flux across the membrane is equal to flux through the boundary layers.

Diffusion of gas species i across the feed side boundary layer can be described as the equilibrium between diffusion and convection as described elsewhere [45,53].

$$\Delta\dot{n}_i = k_i\,\frac{p_F}{R\,T}\left(x_{i,F,bulk} - x_{i,F,surface}\right) + x_{i,F,bulk}\left(\Delta\dot{n}_i - \Delta\dot{n}_j\right) \tag{2.11}$$

Mass permeate across the dense membrane layer has been previously described in the solution-diffusion model.

$$\Delta\dot{n}_i = \frac{B_i}{l}\left(p_F\, x_{i,F,surface} - p_S\, x_{i,S,bulk}\right) \tag{S2.9}$$

By conservation of mass for binary gas mixtures of species *i* and *j*, the two expressions are equal at steady state.

$$\frac{B_i}{l}\left(p_F\, x_{i,F,surface} - p_S\, x_{i,S,bulk}\right) = \frac{k_i\, p_F}{R\,T}\left(x_{i,F,bulk} - x_{i,F,surface}\right) + x_{i,F,bulk}\left(\Delta\dot{n}_i - \Delta\dot{n}_j\right) \tag{S2.24}$$

Solving the equation for $x_{i,F,surface}$ we obtain the expression below:

$$x_{i,F,surface} = x_{i,F,bulk}\left(\frac{k_i \frac{p_F}{R\,T} + \frac{B_i}{l}\, p_S\left(x_{i,S,bulk}\left(\frac{1}{\alpha_{i/j}} - 1\right) + \frac{1}{\alpha_{i/j}}\left(\frac{p_F}{p_S} - 1\right) + \frac{x_{i,S,bulk}}{x_{i,F,bulk}}\right)}{k_i \frac{p_F}{R\,T} + \frac{B_i}{l}\, p_F\left(1 + x_{i,F,bulk}\left(\frac{1}{\alpha_{i/j}} - 1\right)\right)}\right) \tag{2.13}$$

CHAPTER THREE

ENERGY FROM CARBON DIOXIDE:

EXPERIMENTAL AND THEORETICAL ANALYSIS OF POWER GENERATION

FROM MEMBRANE-BASED SWEEP GAS PERMEATION

3.1 Original publication

Chapter Three is based primarily on a paper that was originally published in the Journal of Membrane Science2[2]. This publication was the first in literature to study the possibility of using a rich flue of carbon dioxide for power generation in a binary gas process using a membrane module. Experimental validation of the process and numerical model was carried across a range of applied pressure and with different concentration of CO_2 in the feed. Simulation results from the model were then used to evaluate the effect of machine efficiency on the net power balance of the energy conversion process.

3.2 Introduction

Providing clean energy to a rapidly growing and developing global population, while also protecting the environment, is one of the great challenges of our time [61-64]. The development of sustainable power infrastructure will require innovation in many areas, including the introduction of new energy conversion technologies and the improvement of

[2] S. Moussaddy and J. Maisonneuve. "Energy from carbon dioxide: Experimental and theoretical analysis of power generation from membrane-based sweep gas permeation". Journal of Membrane Science. Vol. 644: 120053, 2021. DOI: 10.1016/j.memsci.2021.120053.

existing thermal power plants. For some time, efforts to capture and sequester carbon from major point source emissions such as from coal or natural gas plants, have received significant attention [10,35-39,65,66]. However, from these same exhaust sources, there exists a significant energy resource that has been mostly overlooked, namely the chemical potential available from gradients of gas mixtures between exhaust sources and the atmosphere. Harvesting this energy and converting it to useful work can help support a sustainable energy future by improving the efficiency of thermal power plants and thereby reducing harmful emissions per unit of electricity generation. As such, exhaust energy recovery can be one piece of a clean energy future.

In this work, we introduce a novel membrane-based process for converting potential energy from gas mixture gradients to useful mechanical work. The proposed system is illustrated in Figure 3.1. As shown, a selective membrane is used to separate rich feed gas from a diluted sweep stream, and thereby establish a partial pressure gradient capable of driving mass transfer of the permeable gas species (carbon dioxide CO_2 in this case). When the sweep gas is compressed up to some applied pressure above atmosphere, the increasing mass can be used to do net positive work on a load, and thereby generate power. In many ways, the process is analogous to a Brayton cycle engine cycle which is driven by a temperature gradient [67], or an osmotic power process which is driven by a salinity gradient [16,56,68].

Other efforts to convert CO_2 to power have so far been limited. A first concept was demonstrated by Hamelers et al [11-13] in 2014, in which dissolved carbon dioxide was used to generate electric current through a capacitive cell composed of ion selective membranes. Shortly thereafter, Kim et al [14] demonstrated operation of an

electrochemical flow cell, similarly powered by CO_2 dissolved in water. Power densities of up to 4.5 mW/m^2 were obtained in the first case, and 820 mW/m^2 in the latter.

The process introduced here differs fundamentally from these previous concepts, in that it is a mechanochemical conversion process rather than an electrochemical one. Also, the process can be used to convert potential energy from not only CO_2 but from any concentrated gas mixture that generates a partial pressure gradient (so long as an appropriately selective membrane is available). In this regard, our previous work has experimentally validated this concept for the case of water vapor, where a humid feed source is supplied to a module equipped with a membrane that is favorably permeable to water vapor [69]. In that study, power density of up to 57 mW/m^2 was observed from water vapor permeate. To date, the potential for this process to convert CO_2 gradient energy has not been considered in the literature.

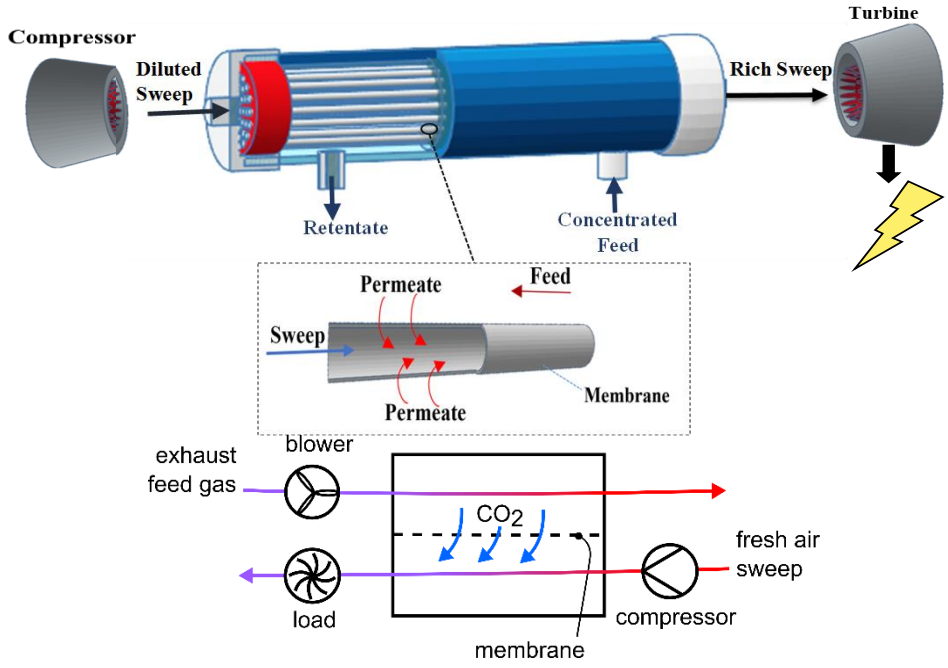

Figure 3.1. An increasing mass of pressurized air can be generated via membrane-based gas permeation. In the proposed system, fresh air acts as a diluted sweep gas to draw CO_2 permeate from a concentrated exhaust feed source and deliver it to a load for useful energy conversion.

In this study we provide the first-ever experimental demonstration of power generation from a membrane-based CO_2 sweep gas process. A laboratory-scale prototype and test protocol are detailed, and experimental results are presented. Fundamental transport dynamics are outlined and simulation results from a numerical model are compared, against experimental observations. Performance is evaluated over a range of flow rates and concentrations, and analysis of critical operating conditions is provided. Finally, the effects of turbine and compressor efficiency on net positive power are analyzed and the requirements for a favorable energy balance are outlined. The idea that CO_2 permeate can be used to produce an expanding mass of pressurized gas is a novel concept that has the potential for power generation, and as far as the authors are aware, this is the first demonstration of net gas permeation against an applied pressure.

3.3 Theory

The diffusion of gas species *i* through a polymeric dense membrane of thickness *l* is a function of the partial pressure difference of that species Δp_i across the membrane, and the membrane's characteristic permeability to that species B_i. The resulting rate of permeate $\Delta \dot{m}_i$ is often normalized per unit membrane surface area *a*, to obtain permeate mass flux J_i [45-53].

$$\mathrm{J_i} = \frac{\Delta \dot{\mathrm{m}}_\mathrm{i}}{\mathrm{a}} = \frac{\mathrm{B_i\ M_i}}{\mathrm{l}}\ \Delta \mathrm{p_i} = \frac{\mathrm{B_i\ M_i}}{\mathrm{l}}\ \left(\mathrm{p_F\ x_{i,F}} - \mathrm{p_S\ x_{i,S}}\right) \tag{3.1}$$

Where *M* is the molar mass, p_F and p_S are the feed and sweep pressures, and $x_{i,F}$ and $x_{i,S}$ are the mole fractions of species *i* at the feed and sweep membrane interface.

When non-linear concentration profiles are considered as a result of dissimilar diffusion rates in binary gas mixes, the resulting feed side concentration of species *i* on the membrane surface is obtained. A detailed derivation of this expression was developed in our previous paper [69].

$$x_{i,F} = x_{i,F,bulk}\left(\frac{k_i + B_i M_i p_S\left(x_{i,S,bulk}\left(\frac{1}{\alpha_{i/j}} - 1\right) + \frac{1}{\alpha_{i/j}}\left(\frac{p_F}{p_S} - 1\right) + \frac{x_{i,S,bulk}}{x_{i,F,bulk}}\right)}{k_i + B_i M_i p_F\left(1 + x_{i,F,bulk}\left(\frac{1}{\alpha_{i/j}} - 1\right)\right)}\right) \quad (3.2)$$

Where $x_{i,F,bulk}$ and $x_{i,S,bulk}$ are the concentrations of species *i* in the bulk feed and sweep gas mixtures, k_i is the overall mass transfer coefficient of *i* at standard conditions, and $\alpha_{i/j}$ is the permeability of species *i* relative to species *j*, a term also referred to as the membrane selectivity.

The overall mass transfer coefficient k_i can be estimated using the following expression for a binary gas mix circulated in a hollow fiber membrane [46-47],

$$k_i = 7.32\ 10^{-4}\ \frac{D_i}{d_h}\ Re^{0.6}\ Sc^{0.33}\ \frac{p\ M_i}{R\ T} \quad (3.3)$$

Where *Re* is the Reynolds number ($= d_h\ u\ /\ v$), *Sc* is the Schmidt number ($= v\ /\ D_i$), d_h is the hydraulic diameter, *u* is the flow velocity, *v* is the kinematic viscosity and D_i is the diffusivity of species *i* within the bulk stream.

As a result of the imperfect selectivity of real membranes, the diffusion of multiple gas species will occur simultaneously and in opposite directions as driven by the partial pressure gradients of each particular species. The net rate at which mass permeate is accumulated on the sweep side and hence delivered towards the turbine, will then be the sum of each individual species flux.

$$J_{net} = \frac{1}{a} \sum \Delta \dot{m}_i \tag{3.4}$$

Net power density from the gas permeation process is then a function of the net permeate flux that is delivered to the turbine for energy conversion, where power extracted from an adiabatic process and isentropic expansion is given as follows [58].

$$\frac{\dot{W}_{net}}{a} = J_{net} \frac{R\,T}{M} \left(\frac{K}{K-1}\right)\left(\left(\frac{p_S}{p_F}\right)^{\frac{K-1}{K}} - 1\right) \tag{3.5}$$

Where K is the heat capacity ratio.

This power that is obtained from the net balance of all flux towards the sweep side turbine, will be a fraction of the theoretical power that could be obtained from the permeate of only a single species *i*, if a perfectly selective ideal membrane were used, in which case power density is described as follows.

$$\frac{\dot{W}_i}{a} = J_i \frac{R\,T}{M_i} \left(\frac{K}{K-1}\right)\left(\left(\frac{p_S}{p_F}\right)^{\frac{K-1}{K}} - 1\right) \tag{3.6}$$

We note that both equations (3.5) and (3.6) express only the thermodynamic work of permeate. This power potential is equivalent to mechanical or electric power only when ideal machines with turbine and compressor efficiencies of 100 % are assumed for perfect energy conversion. Despite this simplification, equations (3.5) and (3.6) nonetheless provide a useful measure of the thermodynamic limit for energy conversion and an upper bound for this concept. A detailed analysis of the effect of machine efficiencies is provided further on in the Discussion section of this paper.

3.4 Materials and Methods

3.4.1 Numerical Analysis

The theoretical performance of CO_2 power generation was simulated in Matlab (R2018a, Mathworks, Natick, MA) using a model developed from the transport equations described in Section 2. The model uses a finite element approach to solve the mass balance in a 2-dimensional space. Differential diffusion rates of multiple gas species are considered to describe concentration variations in the direction normal to the membrane surface, and differential permeation rates of multiple gases across the membrane are considered to describe concentration variations in the axial direction. A detailed flow chart of the modelling approach is provided in Supplementary Note 3.1 and MATLAB script is provided in Supplementary Note 3.5. Also, a similar modelling approach has been described in our previous work [69].

A summary of the modelling inputs is provided in Table 3.1. Ideal gas behavior is assumed, and a binary gas mixture of nitrogen and carbon dioxide is considered. Permeability to CO_2 and nitrogen N_2 gases for a dense polydimethylsiloxane membrane were specified by the manufacturer and confirmed in the literature [70]. Additional membrane characteristics and process parameters were consistent with experimental test conditions, as described further on in Section 3.2. Gas properties of viscosity and heat capacity were assumed constant. Although axial variations in concentration will lead to minor changes in these properties along the membrane length, these changes have a very minor effect on simulated flux, and therefore they were treated as constant for simplicity. Axial variations in density on the other hand have a much more significant effect on flux

and therefore updated values were used for each finite element by considering the composition of gases and the density of pure species.

Table 3.1. Simulation input parameters

CO_2 permeability B_{CO2}	3200 Barrer
N_2 permeability B_{N2}	300 Barrer
Membrane thickness l	55 μm
Hydraulic diameter d_h	1.4 mm
Kinematic viscosity ν [32]	15.3×10^{-6} m^2/s
Diffusivity of CO_2 D_{CO2}	1.64×10^{-6} m^2/s
Heat capacity ratio K [32]	1.29

3.4.2 Experimental Analysis

CO_2 power potential was experimentally demonstrated, and the proposed transport model was validated using a series of laboratory tests. The test bench is shown in Figure 3.2.

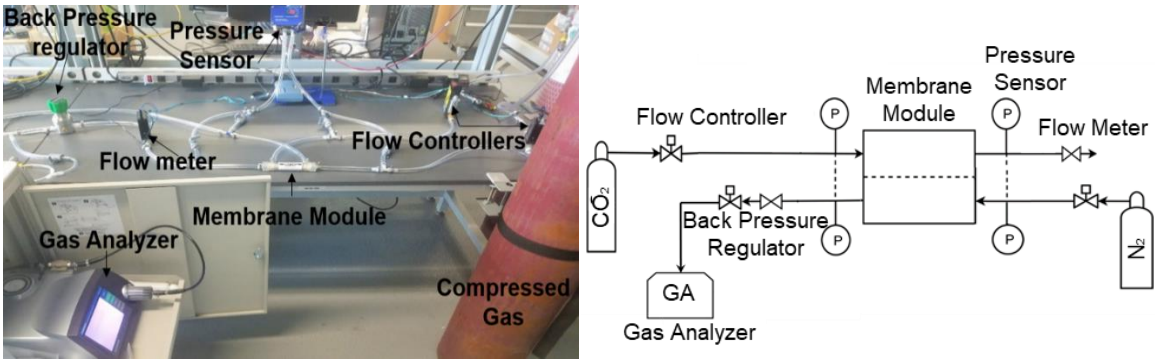

Figure 3.2. Laboratory test bench installed at Oakland University. The bench houses a 4-port membrane module that is supplied by sweep and feed gas lines, both of which are equipped with flow and pressure controls and sensors. Feed and sweep are supplied by compressed gas cylinders, and outlet gas composition is measured by an emission analyzer.

The bench consists of a membrane module that is supplied by two lines that deliver feed and sweep gases respectively from compressed gas cylinders. Pressure from the feed cylinder is controlled by a single stage regulator (PRS20023351320, Praxair, Danbury, CT) and delivered to the membrane at approximately atmospheric pressure. Pressure on the sweep line is controlled by the combination of a single stage regulator (TPR250500580, Praxair, Danbury, CT) and a back-pressure regulator (KBP1F0D4A5A20000, Swagelok, Solon, OH), and delivered at a range of pressures. Pressure across both lines is monitored and recorded using a differential pressure transducer (GC557F0142CD, Ashcroft, Stratford, CT) mounted between the inlet and outlet ports of the sweep and feed respectively. Flow rate to the membrane module is regulated by mass flow controllers including a high-precision meter on the sweep side (GH-32907-69, Masterflex, Vernon Hills, IL) and a medium-precision meter on the feed (GFMS-010009, Aalborg, Orangeburg, NY). A high-precision mass flow meter is also mounted on the sweep outlet (EW-32908-69, Masterflex, Vernon Hills, IL), and the difference in mass flow is recorded to evaluate permeate. Sweep gas is exhausted to a gas analyzer (MEXA-584L, Horiba, Kyoto, Japan) to determine CO_2 concentrations and distinguish between net permeate flux and CO_2 permeate flux.

All data is recorded by an automated acquisition system (USB-1608G, MO Measurement Computing, Contoocook, NH) connected to a PC.

A dense polydimethylsiloxane (PDMS) membrane (PermSelect, Ann Arbor, MI) was selected for this study, and mounted on the test bench. Key membrane specifications as provided by the manufacturer are summarized in Table 3.2.

Table 3.2. Membrane parameters

Material	polydimethylsiloxane
Module type	hollow fiber
Membrane area *a*	0.1 m^2
Fiber length	0.16 m
Fiber outer diameter d_o	300 μm
Fiber thickness l	55 μm
Number of fibers	1280
Flow orientation	counter flow

Tests were conducted across a range of conditions, to observe the effects of feed and sweep supply rates, CO_2 feed concentration, and applied pressure.

Table 3.3. Experimental test conditions

Feed Source	
CO_2 / N_2 concentration $x_{i,F}$	20 / 80 % mol
	99.9 / 0 % mol
Mass flow rate	1 – 4.5 slpm
Temperature	20 °C
Pressure p_F	1 bar
Sweep Source	
CO_2 / N_2 concentration $x_{i,S}$	0 / 99.9 % mol
Mass flow rate	1 – 4.5 slpm
Temperature	20 °C
Pressure p_S	1 – 3 bar

The feed line was supplied by CO_2 gas with 20 % concentration (NI CD20C-K, Praxair, Danbury, CT) to approximate coal-fired flue gas, and then nearly pure CO_2 gas (99.9 % CO_2, CD 4.0IS-KS, Praxair, Danbury, CT) to approach the limits of the process. The sweep line was supplied by nearly pure N_2 gas (99.9 % CO_2, PX NI5.0UH-T, Praxair, Danbury, CT) to approximate ambient air. A summary of the test conditions is provided in Table 3.3.

Equations (3.7) – (3.10) were used to analyze the experimental data and obtain results for flux and power potential of both CO_2 and net permeate. Mass flow rates of sweep gas at the membrane inlet and outlet, $\dot{m}_{S,in}$ and $\dot{m}_{S,out}$, are measured respectively by the GH-32907-69 mass flow controller (5 slpm ± 0.8 % of reading and 0.2 % of full scale) and the EW-32908-69 mass flow meter (5 slpm ± 0.8 % of reading and 0.2 % of full scale). The CO_2 mass fraction of sweep at the membrane outlet $\omega_{S,out,CO2}$ is measured by the MEXA-584L gas analyzer (20 ± 0.17 % vol CO_2). Sweep and feed pressures, p_S and p_F, are measured by the GC557F0142CD transducer (75 psi ± 0.38 psi). A detailed sample of raw data, analysis, and uncertainty analysis is provided in Supplementary Note 3.2 and 3.4, and a complete raw dataset of all measurements is provided in Supplementary Note 3.3.

$$J_{CO2} = \frac{\dot{m}_{S,out}\,\omega_{S,out,CO2}}{a} \tag{3.7}$$

$$J_{net} = \frac{\dot{m}_{S,out} - \dot{m}_{S,in}}{a} \tag{3.8}$$

$$\frac{\dot{W}_{CO2}}{a} = J_{CO2}\,\frac{R\,T}{M_{CO_2}}\left(\frac{K}{K-1}\right)\left(\left(\frac{p_s}{p_F}\right)^{\frac{K-1}{K}} - 1\right) \tag{3.9}$$

$$\frac{\dot{W}_{net}}{a} = J_{net}\,\frac{R\,T}{M}\left(\frac{K}{K-1}\right)\left(\left(\frac{p_s}{p_F}\right)^{\frac{K-1}{K}} - 1\right) \tag{3.10}$$

3.5 Results

3.5.1 Power Potential of CO_2 Gas Permeate

Figures 3.3 and 3.4 show the experimental and theoretical results obtained from CO_2 permeate under a range of conditions. These results show the first ever demonstration of power potential from CO_2 sweep gas permeation, with up to 6.35 W/m^2 generated from 192 g/m^2/h of CO_2 flux observed at 2 bar applied pressure difference, when supply flow rates of feed and sweep are at their greatest, and when feed concentration is pure CO_2. Simulation results show reasonable agreement with experimental data accounting for major trends and correctly identifying dominant transport dynamics. Simulation results indicate that greater power density approaching 10 W/m^2 can be obtained from CO_2 permeate when operated at higher applied pressure difference, however in this case experiments were limited by laboratory equipment specifications. We note that the conversion of observed mass flux to equivalent power density here assumes that compressor and turbine energy conversion is ideal and 100 % efficient. This assumption is made throughout the Results Section, however the effect of reducing machine efficiencies is examined in detail in the Discussion Section.

We note also that these results involve the use of a 99.9 % pure CO_2 feed. This source is used only for demonstration purposes, however real applications will not involve pure CO_2 feed. Recovering energy from a purified CO_2 feed stream would defeat the purpose of the proposed system and would represent a thermodynamic contradiction. Figure 3.4 shows more realistic conditions with a 20 % CO_2 feed meant to approximate a likely application to coal-fired flue gas. As expected, lower CO_2 concentrations in the feed, lead to a reduction in permeate flux and therefore power density. Interestingly, this drop in flux does not

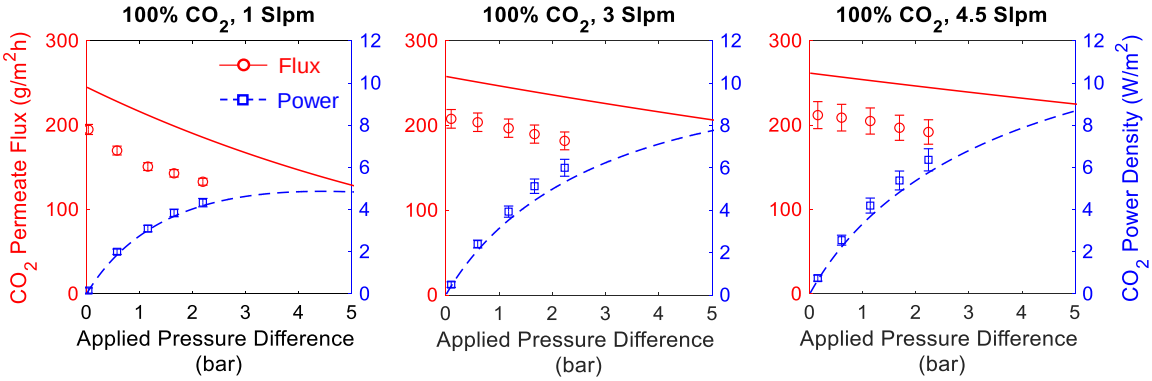

Figure 3.3. CO_2 permeate flux and the resulting power density when nearly pure CO_2 gas (99.9 %) is supplied as feed. Experimental results are identified by data points and simulation results by solid and hatched lines. Conditions are summarized in Tables 3.1-3. Assuming that compressor and turbine energy conversion is ideal and 100 % efficient. Raw data and analysis are provided in Supplementary Note 3.2.

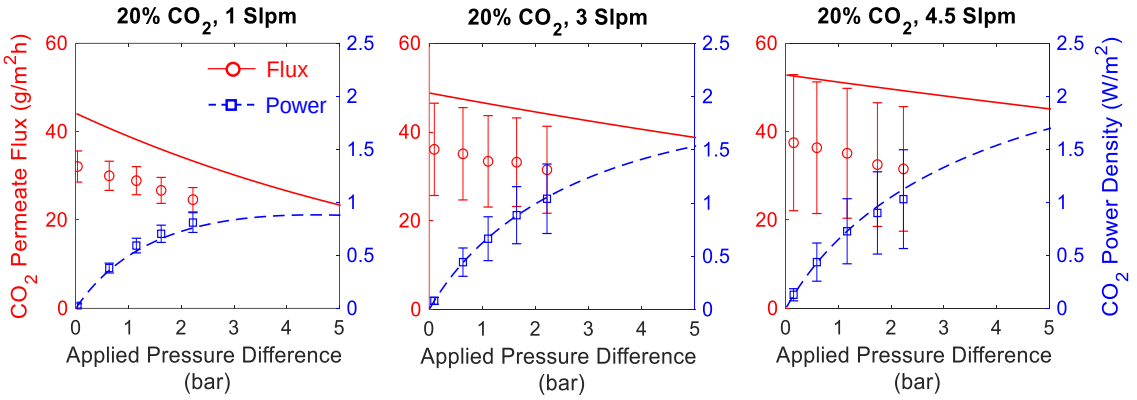

Figure 3.4. CO_2 permeate flux and the resulting power density when the feed line is supplied by CO_2 gas with 20 % concentration to approximate coal-fired flue gas. Experimental results are identified by data points and simulation results by solid and hatched lines. Test and simulation conditions are summarized in Tables 3.1-3. Assuming that compressor and turbine energy conversion is ideal and 100 % efficient.

appear linearly proportional to the drop in concentration. More realistic CO_2 feed concentrations of 20 % considered in Figure 3.4 generated about half the flux as the exaggerated case of pure 99.9 % CO_2 that is considered in Figure 3.3. Also expected, increasing feed and sweep supply flow rates had the effect of increasing permeate flux and therefore power density. This is due to a reduction in axial dilution, as well as improved mixing that mitigates polarization, as is well documented elsewhere [17,70-72]. Also of note is the relatively high experimental uncertainty observed for test trials at higher supply flow rates and at lower CO_2 feed concentrations. This is because the sweep outlet gas tends to have lower CO_2 concentrations under these conditions, and therefore uncertainty of the gas analyzer measurement will appear relatively greater. Nevertheless, experimental results across all trials generally show only minimal uncertainty and agree reasonably well with numerical simulations.

3.5.2 Power Potential of Net Gas Permeate

As CO_2 permeate is accumulated by the pressurized sweep stream, an imperfectly selective membrane will allow reverse leakage of N_2 gas to be lost towards the feed, thereby reducing the net permeate flux received by the sweep. Figures 3.5 and 3.6 show the net permeate flux and the resulting net power potential that was observed from the laboratory tests described previously. The effect of reverse gas leakage is evident especially at high applied pressures. This is expected, as higher pressures reduce the partial pressure difference of CO_2, while exacerbating the partial pressure difference of N_2. The result is a dramatic shift in the tail of the flux curve, with net reversal expected at less than 10 bar for the cases shown. Similarly, the maximum power point is shifted to the left so that maximum power is obtained at less than 5 bar. The highest net power potential observed from

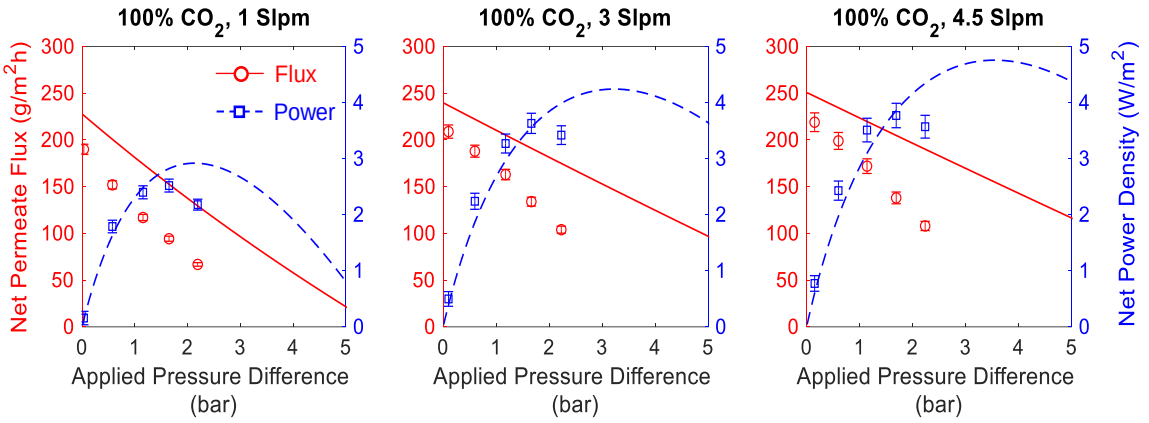

Figure 3.5. Net permeate flux and the resulting power density when nearly pure CO_2 gas (99.9 %) is supplied as feed. Experimental results are identified by data points and simulation results by solid and hatched lines. Test and simulation conditions are summarized in Tables 3.1-3. Power density calculated from observed permeate flux assumes that compressor and turbine energy conversion is ideal and 100 % efficient. Raw data and analysis are provided in Supplementary Note 3.2.

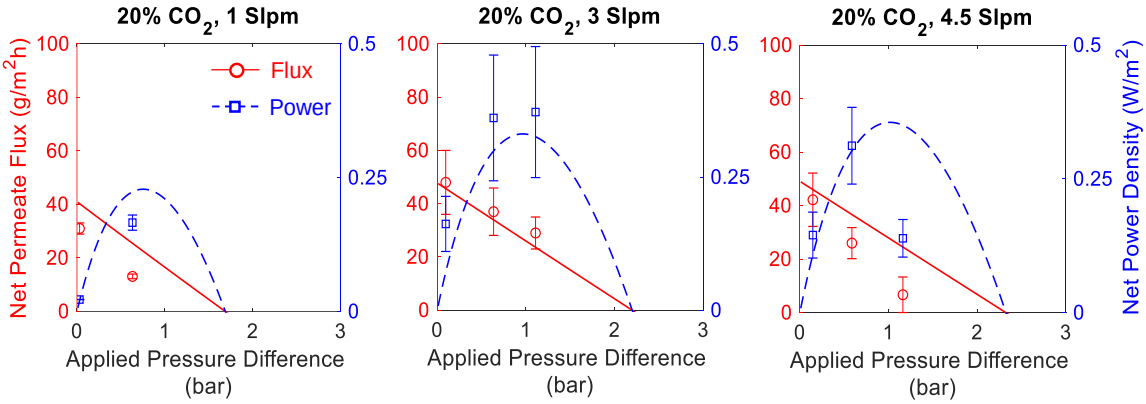

Figure 3.6. Net permeate flux and the resulting power density when the feed line is supplied by CO_2 gas with 20 % concentration to approximate coal-fired flue gas. Experimental results are identified by data points and simulation results by solid and hatched lines. Test and simulation conditions are summarized in Tables 3.1-3. Power density calculated from observed permeate flux assumes that compressor and turbine energy conversion is ideal and 100 % efficient.

experimental testing is 3.77 W/m^2, which is obtained from 138 g/m^2/h of flux at 2 bar applied pressure difference. This is roughly half the power observed from CO_2 flux only, which is the power that might be expected from a perfectly selective membrane.

More realistic exhaust CO_2 concentrations of 20 % are considered in Figure 3.6. These again show significantly less power potential than the exaggerated case of pure 99.9 % CO_2 feed from Figure 3.5. This is expected as the driving CO_2 partial pressure gradient is significantly less. Somewhat unexpected is that the drop between CO_2 power and net power appears greater when comparing Figures 3.3 and 3.5 for high CO_2 feed than when comparing Figure 3.4 and 3.6 for low CO_2 feed. This is surprising, because the undesirable N_2 gradient is significantly less for the case of low CO_2 feed concentrations, and therefore so is any undesirable reverse N_2 leakage. However, it can be shown by analysis that an increase in applied pressure and therefore an increase in sweep side N_2 pressure, will more severely increase the N_2 pressure gradient when N_2 feed concentrations are high (i.e. when CO_2 feed concentrations are low). The result of this is observed by the sharp drop in the tail of the flux curve. For example, in Figure 3.6 negative net flux is observed at only about 2 bar applied pressure, much less than for the case of high CO_2 feed.

3.6 Discussion

Experimental and simulation results reported above describe the power potential of an expanding mass of pressurized gas, as driven by CO_2 permeate and net permeate across a semi-permeable membrane. However, this power potential is only equivalent to mechanical or electric power in the hypothetical case that energy conversion is done by ideal machines. In reality, compression and expansion of the sweep gas will be done by a

compressor and turbine with significant losses. Without careful consideration, it is possible that these losses will overwhelm any potential work available from the pressurized mass permeate, and result in a negative energy balance. In this section we provide energy balance analysis for the sweep gas power system with consideration for machine inefficiencies. While other parasitic loads can be included, we limit our analysis to losses at the compressor and turbine.

The balance between power generated at the turbine and power consumed by the compressor is given for an adiabatic and isothermal process as follows (detailed derivation is provided in Supplementary Note 3.4):

$$\dot{W}_{balance} = \dot{W}_{turbine} - \dot{W}_{compressor} \tag{3.11}$$

$$\dot{W}_{balance} = R\,T\left(\frac{K}{K-1}\right)\left(\left(\frac{p_s}{p_F}\right)^{\frac{K-1}{K}} - 1\right)\left(\eta_{turbine}\,\dot{n}_{S,out} - \frac{\dot{n}_{S,in}}{\eta_{compressor}}\right) \tag{3.12}$$

η is the efficiency (i.e. for compressor or turbine). $\dot{n}_S$ is the sweep flow, and the difference between sweep flow rate at the membrane inlet and outlet is the permeate flow rate $\Delta\dot{n}$ defined previously in eq. (3.1).

Using the previously validated transport model, the energy balance of the sweep gas power system was determined for a range of system efficiencies, assuming that both the compressor and turbine efficiencies are equal, $\eta_{compressor} = \eta_{turbine}$. Figure 3.7 shows the net power density results for the same PDSM membrane and operating conditions considered in Section 3.4.2. The curves shown for machine efficiencies of 100 % match the ideal net power curves previously shown in Figures 3.5 and 3.6. However, as lower efficiencies are considered, a severe drop in the energy balance is observed. For example, for the case of pure CO_2 feed supplied at flow rates of 1 slpm, the net power drops from a maximum of 3

W/m^2 with ideal machines, to 1.4 W/m^2 for an efficiency of 95 %. Under other conditions the drop is even more severe and leads to a negative energy balance. For example, when more realistic CO_2 feed concentrations of 20 % are supplied, maintaining a positive energy balance is only possible with very high machine efficiencies of ~ 98 %. These exceed the typical efficiencies reported for utility scale compressors and turbines, which tend to be on the order of 85 % [58].

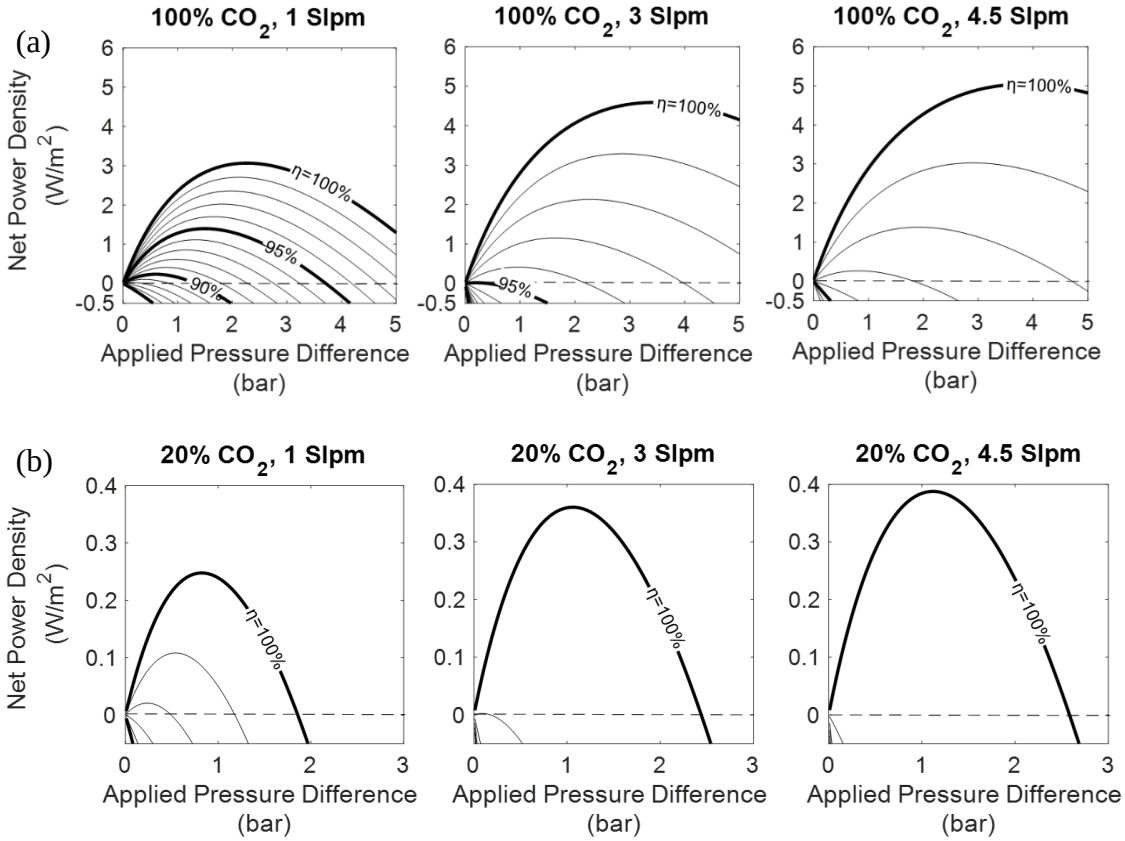

Figure 3.7. Net power density obtained from the balance of power generated at the turbine and power consumed at the compressor given a range of machine efficiencies $\eta_{compressor} = \eta_{turbine}$ (with curves shown at intervals of $\Delta\eta$ = 1 %). Simulation results are generated with the validated transport model described in Section 3.4, for a range of feed and sweep flow rates, and for CO_2 feed concentrations of (a) 99.9 % and (b) 20 %. Other simulation parameters are summarized in Tables 3.1-3.

Improving the overall energy balance of the process can be achieved with high machine efficiencies, but also with improved mass transport dynamics across the membrane. Figure 3.8 shows the net power density results obtained when a high performance Polaris^{TM} Gen-2 membrane is used, which has permeance B_{CO2} / l = 2000 gpu and selectivity $\alpha_{CO2/N2}$ = 49 [73]. As shown, the higher permeability and selectivity of the membrane yield higher power densities with up to 40 W/m^2 for the cases shown. These higher power densities help to compensate for energy conversion losses at the compressor and turbine. For example, when realistic CO_2 feed concentrations of 20 % are supplied, maintaining a positive energy balance can now be achieved with machine efficiencies as low as ~ 95 %.

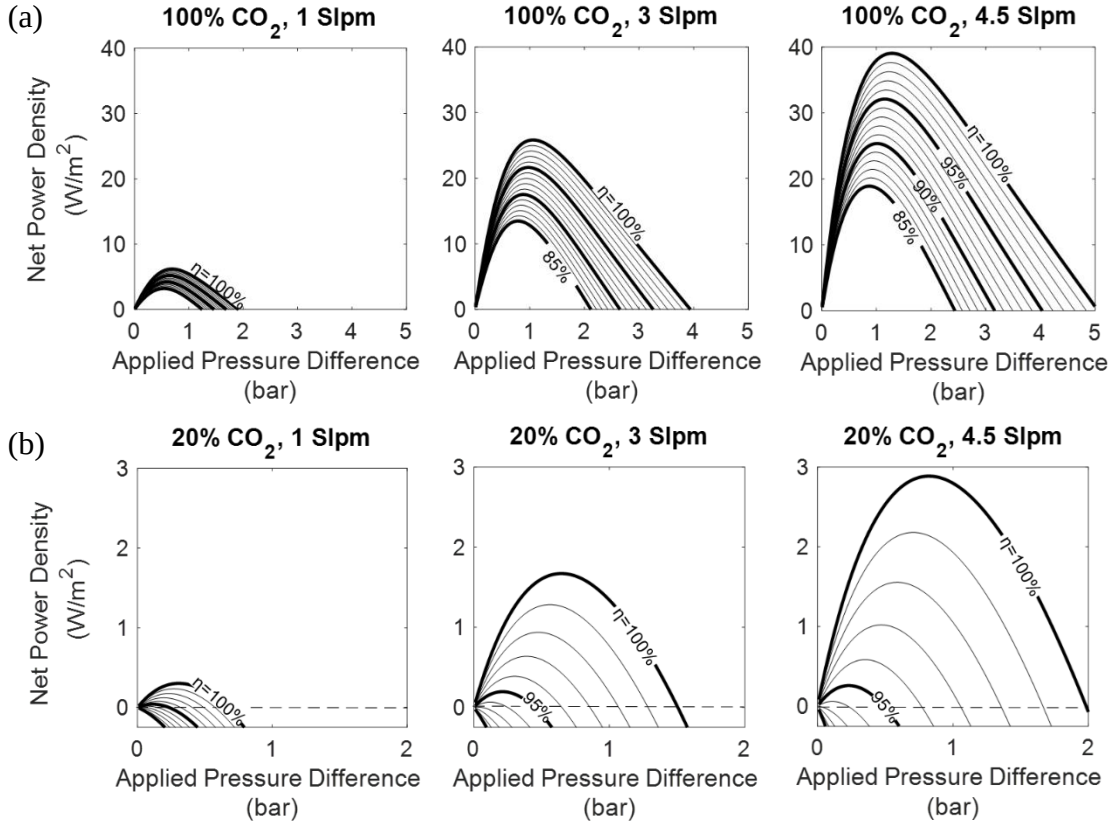

Figure 3.8. Net power density from Polaris^{TM} Gen-2 membrane (B_{CO2} / l = 2000 gpu and $\alpha_{CO2/N2}$ = 49) given a range of machine efficiencies $\eta_{compressor} = \eta_{turbine}$ (with curves shown at intervals of $\Delta\eta$ = 1 %). Simulation results are generated using the model described in Section 3.3, for a range of feed and sweep flow rates, and for CO_2 feed concentrations of (a) 99.9 % and (b) 20 %. Other simulation parameters are summarized in Tables 3.1-3.

Figures 3.7 and 3.8 also reveal the importance of carefully setting feed and sweep flow rates to achieve a most favorable energy balance. While high flow rates reduce undesirable polarization and dilution, and therefore favor net power from an ideal system ($\eta = 100$ %), these same high flow rates exacerbate machine losses. Therefore, for the PDMS membrane shown in Figure 3.7 we see that low feed and sweep flow rates of 1 slpm yield a more favorable energy balance than high flow rates of 4.5 slpm when machine efficiencies are less than 98 %. For the Polaris^{TM} Gen-2 membrane shown in Figure 3.8 the best flow rates are greater and may in fact be greater than 4.5 slpm even for machine efficiencies as low as 85 %. In general, it is clear that operating flow rates should be optimized to suit membrane and site conditions, and thereby optimize the net energy balance of the power system. Whereas lower machine efficiencies will move the best flow rates lower, high-performance membranes with greater permeability and selectivity will move the best flow rates higher to a certain optimum.

To illustrate, Figure 3.9 shows the energy balance as a function of feed and sweep flow rates, for the specific case of a feed stream with 20 % CO_2 concentration and a system with machine efficiencies of 95 %. Because net power density is also a function of applied pressure, each data point shows the maximum power that can be obtained from the best applied pressure. As shown, there is a clear peak power at flow rates of 5 Slpm, where the balance between turbine and compressor power is maximized.

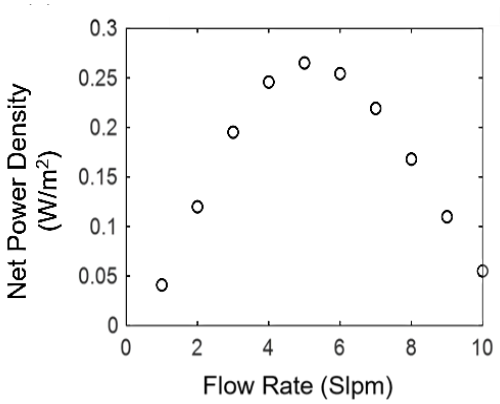

Figure 3.9. Maximum net power density obtained from the balance of power generated at the turbine and power consumed at the compressor, for across a range of feed and sweep supply flow rates. Simulation results are generated with the validated transport model described in Section 3.3, and assuming machine efficiencies $\eta_{compressor} = \eta_{turbine} = 95$ %, feed stream CO_2 concentrations of 20 %, and Polaris™ Gen-2 membrane with permeance of $B_{CO2} / l = 2000$ gpu and selectivity of $\alpha_{CO2/N2} = 49$ obtained. Other simulation parameters are summarized in Tables 3.1-3.

3.7 Conclusions

In this study we have introduced and experimentally validated the novel concept of using CO_2 gas permeation to generate an expanding mass of pressurized gas for potential power generation. While the general concept was introduced in our previous work [69], this is the first ever demonstration of power from CO_2 sweep gas permeation. In addition, while the literature includes many examples of flux driven *by an applied pressure* or vacuum, this work provides the first ever demonstration of CO_2 permeate *against an applied pressure* sweep. Similarly, while some few examples in the literature have documented *slow gas* flux leakage against an applied pressure [10], this is the first ever demonstration of *fast gas* permeation and *net gas* permeation against an applied pressure.

Up to 6.35 W/m^2 of power potential was observed from CO_2 permeate flux, and up to 3.77 W/m^2 from net flux when pure CO_2 was used as the feed source. When more realistic CO_2 feed concentrations of 20 % were used, maximum power potential of 1.08 W/m^2 was observed from CO_2 flux, and 0.37 W/m^2 from net flux. These compare very favorably with

power levels reported for other CO_2 energy conversion processes in the literature, which range from 4.5 mW/m^2 to 0.82 W/m^2 [11-14].

The power densities reported here are based on observed mass flux but assume ideal machines with 100 % efficient energy conversion at the compressor and turbine. To analyze the significance of machine efficiencies as well as other parameters such as membrane permeability and selectivity, a mass transport model of the process was described and validated against experimental data. Simulation results from the model were then used to evaluate the effect of machine efficiency on the net power balance of the energy conversion process. Losses at the compressor and turbine are shown to significantly reduce net power, even yielding negative energy balances for the process unless operating conditions such as feed and sweep flow rates are carefully optimized. To offset these losses, improvements in membrane performance, such as high permeability and selectivity are shown to greatly increase power. For example, the Polaris^{TM} Gen-2 membrane may yield power of up to 40 W/m^2 from pure CO_2 feed sources, or up to 2.9 W/m^2 from more realistic feed sources with 20 % CO_2 concentrations assuming ideal machines. When machine losses are considered however, these power densities shift downward significantly and maintaining a positive energy balance remains challenging and requires high efficiency machines of approximately greater than 90 %.

In addition, other pathways for improving performance and favoring a positive net energy balance should be considered in future work. First, other concentrated gases available in the exhaust feed can be drawn to the sweep stream along with CO_2, thereby increasing net permeate flux and hence net power density. For example, our previous analysis of this concept demonstrated power generation from water vapor permeate.

Simultaneously recovering permeate from multiple gas species, for example from both water vapor and CO_2 permeate, has the potential to double or triple power density. In other words, this same concept can be applied to any number of exhaust gases so long as partial pressure gradients are available together with appropriately selective membranes. This means that energy recovery can be compatible with carbon capture, and a system could be conceived that separates and concentrates CO_2 from the feed, requiring work input, while also diluting and mixing other rich gas permeate such as water vapor, providing useful work output. Various process arrangements and integration strategies should be carefully considered in future work.

Other important dynamics for further consideration should include analysis of thermal dynamics. In most applications exhaust feed is expected to be hot, and therefore mass transfer to the compressed sweep will be coupled with heat transfer. This will have the effect of increasing enthalpy exchange to the sweep stream and thus increasing power generation from the turbine.

In conclusion, the primary contributions of this work have been achieved, which have been to analytically and experimentally demonstrate CO_2 and net gas permeation against an applied pressure, and to thereby demonstrate the potential for power generation. While significant obstacles and questions remain for viable energy recovery from exhaust gases, such challenges are expected with early-stage development of a new concept. Furthermore, several promising pathways for future analysis have been identified, including the possibility of simultaneously recovering energy from multiple gas species and from heat transfer. These suggest that energy potential may in fact be significantly greater than evaluated here and may allow positive energy balances to be achieved even when non-ideal

energy conversion is done by real machines. By improving the energy efficiency of existing thermal power infrastructure, and thereby reducing specific emissions per unit of electricity generation, it is hoped that exhaust energy recovery and other related efforts will contribute to a green energy future.

3.8 Acknowledgment

We acknowledge the Graduate Fellowship to Sarah Moussaddy made by the School of Engineering and Computer Science, Oakland University.

3.9 Nomenclature

a	membrane surface area (m^2)
B	membrane permeability (mol m Pa^{-1} m^{-2} s^{-1})
D	diffusivity (m^2 s^{-1})
d_h	hydraulic diameter (m)
d_o	fiber outer diameter (μm)
J	permeate flux (g m^{-2} s^{-1})
k	mass transfer coefficient (g s^{-1})
K	heat capacity ratio
l	membrane thickness (m)
m	mass (kg)
$\dot{m}$	mass flowrate (g s^{-1})
M	molar mass (g mol^{-1})
n	amount of substance (mol)
$\dot{n}$	molar flow rate (mol s^{-1})
p	pressure (Pa)
R	gas constant (J mol^{-1} K^{-1})
Re	Reynold Number

Sc	Schmidt number
T	absolute temperature (K)
u	velocity (m s^{-1})
$\dot{V}$	flow rate at standard conditions (Sl min^{-1})
$\dot{W}$	power (W)
x	mole fraction (mol/mol)
ω	mass fraction (g/g)
η	efficiency

Greek symbols:

α	membrane selectivity
v	kinematic viscosity (m^2/s)

Subscripts:

CO_2	carbon dioxide
F	feed
i	gas species i
in	membrane inlet
j	gas species j
N_2	nitrogen
out	membrane outlet
S	sweep

3.10 Supplementary Notes

3.10.1 Supplementary Note 3.1: Numerical Modelling Methods

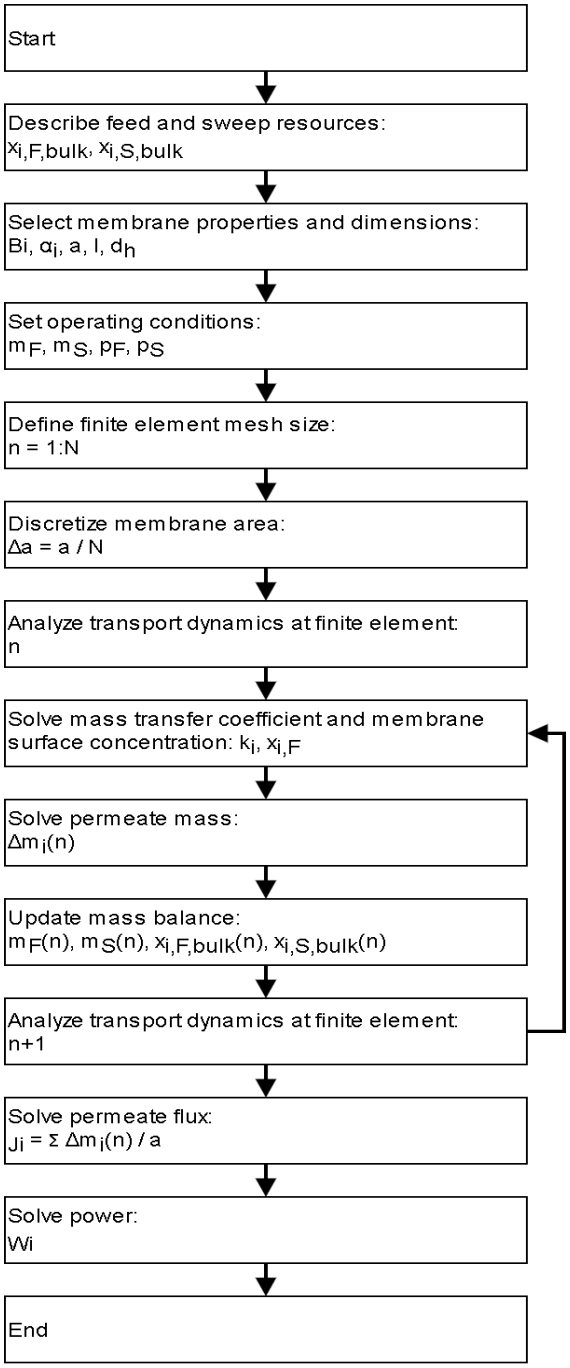

Figure S3.1. Finite element model describing mass balance at each element "n" as a function of the diffusion of gas species through the bulk mixture and across a selective membrane layer. The model was implemented in Matlab (R2018a, Mathwords, Natick, MA) and used to simulate the CO2 energy recovery process.

All experimental observations were verified against theoretical process performance as predicted by numerical simulation of a finite element transport model. The model solves the mass balance and resulting 2-D concentration gradients that are generated tangent and normal to the membrane surface.

3.10.2 Supplementary Note 3.2: Sample Test Data

CO_2 power generation was experimentally demonstrated, and the proposed transport model was validated using a series of tests performed on the Oakland University laboratory bench.

Prior to all testing, preliminary mass balance calibration was performed, wherein both the feed and sweep lines are separately pressurized to 28 psi and tested to compare flow in versus flow out. Leakage of less than 2 % was observed in all calibration testing. Such calibration was included because the laboratory test apparatus includes only 3 measurements of mass flux (namely at the feed inlet, sweep inlet, and sweep outlet) and therefore a complete closed mass balance could not be obtained otherwise during energy recovery test trials.

Energy recovery tests were conducted across a range of feed and sweep supply rates, CO_2 feed concentrations, and applied pressures. Figure S3.2 shows the raw data collected from a sample test when feed flow rate $\dot{V}_{F,in}$ = 2.65 slpm, sweep flow rate $\dot{V}_{S,in}$ = 1 slpm, feed CO_2 concentration $x_{F,in,CO2}$ = 99.9 %, and applied pressure Δp = 1 bar. Table S3.1 provides an outline of how raw data is analyzed, including how experimental uncertainty propagates throughout the analysis.

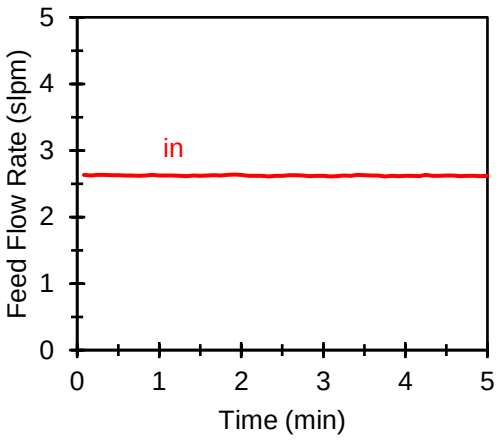

(a)

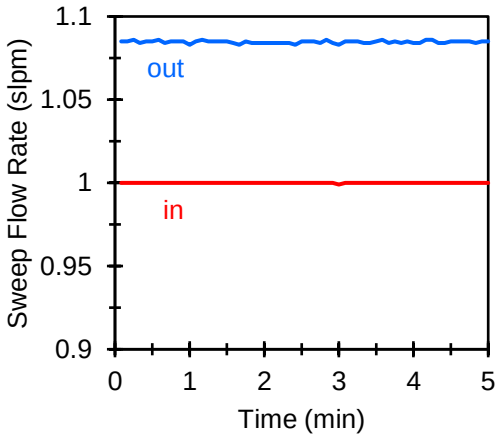

(b)

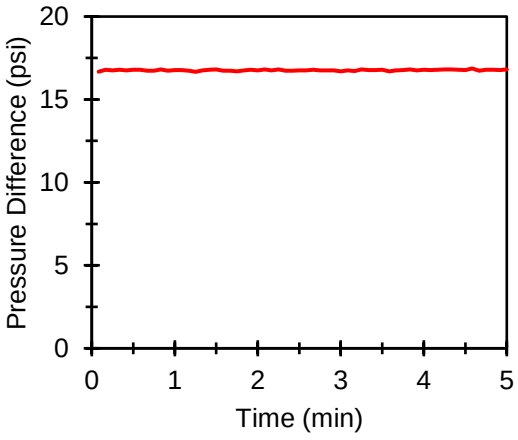

(c)

Figure S3.2. Raw test data. (a) Feed flow at the inlet mass flow controller . (b) Sweep flow rates at the inlet by a mass flow controller and at the outlet by a mass flow meter. (c) pressure difference between outlet feed and inlet sweep

Table S3.1. Analysis of test results.

Parameter	Value	Measurement or Analysis
Average trial measurements		
Inlet feed flow rate $\dot{V}_{F,in}$	2.62 slpm ± 1.9 %	Mass flow controller, GFMS-010009, Aalborg (Orangeburg NY), 5 ± 0.125 slpm
Inlet feed CO_2 conc. $x_{F,in,CO2}$	99.99 % vol	Compressed gas, Praxair (Danbury, CT), 99.99 % CO2
Inlet sweep flow rate $\dot{V}_{S,in}$	1 slpm ± 1.8 %	Mass flow controller, GH-32907-69, Cole Parmer (Vernon Hills, IL), 5 slpm ± (0.8 % reading + 0.2 % full scale)
Inlet sweep CO_2 conc. $x_{S,in,CO2}$	0	Compressed gas, Praxair, (Danbury, CT), 99.99 % N2
Outlet sweep flow rate $\dot{V}_{S,out}$	1.085 slpm ± 1.722 %	Flowmeter, EW-32908-69, Cole Parmer (Vernon Hills, IL), 5 slpm ± (0.8 % reading + 0.2 % full scale)
Outlet sweep CO_2 conc. $x_{S,out,CO2}$	12.08 ± 0.17 % vol	Gas Analyzer, MEXA-584L, Horiba (Kyoto, Japan), 20 %vol CO_2 ± 0.17 % vol
Pressure difference Δp	16.76 psi ± 2.24 %	Differential pressure transducer, GC557F0142CD, Ashcroft (Stratford, CT), 75 ± 0.38 psi
Mass balance analysis		
Inlet sweep flow rate $\dot{m}_{S,in}$	2.03×10^{-5} kg/s ± 1.8 %	$\dot{m}_{S,in} = \rho_{S,in}\,\dot{V}_{S,in}$, $\frac{\delta\dot{m}_{S,in}}{\dot{m}_{S,in}} = \sqrt{\left(\frac{\delta\rho_{S,in}}{\rho_{S,in}}\right)^2 + \left(\frac{\delta\dot{V}_{S,in}}{\dot{V}_{S,in}}\right)^2}$
Inlet sweep density $\rho_{S,in}$	1.218 kg/m^3	$\rho_{S,in} = \frac{p_o\,M_{S,in}}{R\,T_o}$, $M_{S,in} = M_{CO2}$, p_o = 100 kPa, T_o = 273 K
Outlet sweep flow rate $\dot{m}_{S,out}$	2.35×10^{-5} kg/s ± 2.23 %	$\dot{m}_{S,out} = \rho_{S,out}\,\dot{V}_{S,out}$, $\frac{\delta\dot{m}_{S,out}}{\dot{m}_{S,out}} = \sqrt{\left(\frac{\delta\rho_{S,out}}{\rho_{S,out}}\right)^2 + \left(\frac{\delta\dot{V}_{S,out}}{\dot{V}_{S,out}}\right)^2}$

Table S3.1 -Continued

Parameter	Value	Measurement or Analysis
Outlet sweep N_2 conc. $x_{S,out,N2}$	87.92 ± 0.17 % vol	$x_{S,out,N2} = (1 - x_{S,out,CO2})$, $\frac{\delta x_{S,out,N2}}{x_{S,out,N2}} = \frac{\delta x_{S,out,CO2}}{x_{S,out,CO2}}$
Outlet sweep mass $M_{S,out}$	29.93 g/mol ± 1.42 %	$M_{S,out} = x_{S,out,CO2} M_{CO2} + x_{S,out,N2} M_{N2}$, $\frac{\delta M_{S,out}}{M_{S,out}} = \sqrt{\left(\frac{\delta x_{S,out,CO2}}{x_{S,out,CO2}}\right)^2 + \left(\frac{\delta x_{S,out,N2}}{x_{S,out,N2}}\right)^2}$
Outlet sweep CO_2 conc. $\omega_{S,out,CO2}$	17.76 % w ± 2 %	$\omega_{S,out,CO2} = \frac{x_{S,out,CO2} M_{CO2}}{x_{S,out,CO2} M_{CO2} + x_{S,out,N2} M_{N2}}$, $\frac{\delta \omega_{S,out,CO2}}{\omega_{S,out,CO2}} = \sqrt{2\left(\frac{\delta x_{S,out,CO2}}{x_{S,out,CO2}}\right)^2 + \left(\frac{\delta x_{S,out,N2}}{x_{S,out,N2}}\right)^2}$
Net permeate rate $\Delta \dot{m}_{net}$	3.24×10^{-6} kg/s ± 2.87 %	$\Delta \dot{m}_{net} = \dot{m}_{S,out} - \dot{m}_{S,in}$, $\frac{\delta \Delta \dot{m}_{net}}{\Delta \dot{m}_{net}} = \sqrt{\left(\frac{\delta \dot{m}_{S,out}}{\dot{m}_{S,out}}\right)^2 + \left(\frac{\delta \dot{m}_{S,in}}{\dot{m}_{S,in}}\right)^2}$
Net permeate flux J_{net}	116.89 $g/m^2/h$ ± 2.87 %	$J_{net} = \frac{\Delta \dot{m}_{net}}{a}$, $\frac{\delta J_{net}}{J_{net}} = \frac{\delta \Delta \dot{m}_{net}}{\Delta \dot{m}_{net}}$ a = 0.1 m^2
CO_2 permeate rate $\Delta \dot{m}_{CO2}$	4.18×10^{-6} kg/s ± 3 %	$\Delta \dot{m}_{CO2} = \dot{m}_{S,out}\, \omega_{S,out,CO2}$, $\frac{\delta \Delta \dot{m}_{CO2}}{\Delta \dot{m}_{CO2}} = \sqrt{\left(\frac{\delta \dot{m}_{S,out}}{\dot{m}_{S,out}}\right)^2 + \left(\frac{\delta \omega_{S,out}}{\omega_{S,out}}\right)^2}$
CO_2 permeate flux J_{CO2}	150.57 $g/m^2/h$ ± 3 %	$J_{CO2} = \frac{\Delta \dot{m}_{CO2}}{a}$, $\frac{\delta J_{CO2}}{J_{CO2}} = \frac{\delta \Delta \dot{m}_{CO2}}{\Delta \dot{m}_{CO2}}$ a = 0.1 m^2

Table S3.2. Experimental Raw Data

Applied Pressure Difference ΔP	+/-	Inlet Feed Concentration $x_{F,in,CO2}$	Inlet Feed Flowrate $V_{F,in}$	+/-	Inlet Sweep Flowrate $V_{S,in}$	+/-	Outlet Sweep Flowrate $V_{S,out}$	+/-	Outlet Sweep Concentration $x_{S,out,CO2}$	+/-
kPa	%	%	Slpm	%	Slpm	%	Slpm	%	%	%
3	87.6	20	2.5	2.0	1.0	1.8	1.0	1.8	2.7	6.2
63	4.1	20	2.6	1.9	1.0	1.8	1.0	1.8	2.6	6.5
115	2.2	20	2.6	1.9	1.0	1.8	1.0	1.8	2.6	6.6
161	1.6	20	2.6	1.9	1.0	1.8	1.0	1.8	2.4	7.1
222	1.2	20	2.7	1.8	1.0	1.8	0.9	1.9	2.3	7.4
15	17.7	20	5.0	1.0	4.5	1.0	4.5	1.0	0.7	23.8
59	4.4	20	5.0	1.0	4.5	1.0	4.5	1.0	0.7	24.7
116	2.2	20	5.0	1.0	4.5	1.0	4.5	1.0	0.7	25
174	1.5	20	5.0	1.0	4.5	1.0	4.4	1.0	0.6	26.6
223	1.2	20	5.0	1.0	4.5	1.0	4.4	1.0	0.6	27.4
3	76.5	100	2.5	2.0	1.0	1.8	1.4	1.7	14.6	1.2
58	4.5	100	2.6	2.0	1.0	1.8	1.1	1.7	13.2	1.3
116	2.2	100	2.6	1.9	1.0	1.8	1.1	1.7	12.1	1.4
165	1.6	100	2.6	1.9	1.0	1.8	1.1	1.7	11.8	1.4
219	1.2	100	2.6	1.9	1.0	1.8	1	1.8	11.3	1.5
15	17	100	5.0	1.0	4.5	1.0	4.7	1.0	3.92	4.4
60	4.3	100	5.0	1.0	4.5	1.0	4.7	1.0	3.89	4.4
114	2.3	100	5.0	1.0	4.5	1.0	4.6	1.0	3.84	4.4
169	1.5	100	5.0	1.0	4.5	1.0	4.6	1.0	3.63	4.8
224	1.2	100	5.0	1.0	4.5	1.0	4.6	1.0	3.56	4.6

3.10.4 Supplementary Note 3.4: Energy Balance

The balance between power generated at the turbine and power consumed at the compressor can be determined by considering the standard definition for power in an adiabatic and isothermal process [58].

$$\dot{W}_{turbine} = \eta_{turbine}\, \dot{n}_{S,out}\, RT \left(\frac{K}{K-1}\right)\left(\left(\frac{p_S}{p_F}\right)^{\frac{K-1}{K}} - 1\right) \quad \text{(S3.1)}$$

$$\dot{W}_{compressor} = \frac{\dot{n}_{S,in}}{\eta_{compressor}}\, RT \left(\frac{K}{K-1}\right)\left(\left(\frac{p_S}{p_F}\right)^{\frac{K-1}{K}} - 1\right) \quad \text{(S3.2)}$$

Where η is the machine efficiency (i.e. compressor or turbine), $\dot{n}_S$ is the sweep flow rate at the membrane inlet and outlet respectively, and K is the heat capacity ratio.

And therefore, taking the difference between equations (S3.1) and (S3.2) we obtain the following energy balance equation, as was provided in the Discussion section.

$$\dot{W}_{balance} = \dot{W}_{turbine} - \dot{W}_{compressor} \quad (3.11)$$

$$\dot{W}_{balance} = R\, T \left(\frac{K}{K-1}\right)\left(\left(\frac{p_s}{p_F}\right)^{\frac{K-1}{K}} - 1\right)\left(\eta_{turbine}\, \dot{n}_{S,out} - \frac{\dot{n}_{S,in}}{\eta_{compressor}}\right) \quad (3.12)$$

3.10.5 Supplementary Note 3.5: MATLAB Code

```
%Sarah Moussaddy
% FEM for membrane dehumidification with concentration polarization

clear
clc

% constants
M_H2O=18; % (g/mol) molar mass of water
M_N2=28; % (g/mol) molar mass of air
R=8.314; % (J/mol/K) gas constant
Rc=0.1889; %(kJ/kg/K) CO2 gas constant
kc=1.29; % CO2 specific heat ratio
patm=101325; % (Pa) ambient pressure
T0=273; % (K) reference temperature
A=2.414e-5; % (Pa.s)constant for kinematic viscosity
B=247.8; %(K)constant for kinematic viscosity
```

```
C=140; %(K)constant for kinematic viscosity
h_CO2=231.5; %(kj/kg) CO2 enthalpy at 320K

% material properties for silicone hollow fiber membrane
k_CO2=(3.2*3.35*10^-13)/(55*10^-6); % (mol/s/m2/Pa) permeability to
CO2 (input is 3250 Barrer)
j0=k_CO2*(44e-3)/2; % (m3/m2/s/Pa)
b=1/12; %1/selectivity of silicone membrane for N2
k_N2=k_CO2*b; % (mol/s/m2/Pa) permeability to N2
a=0.1; % (m2) membrane surface area
n=1000; % number of nodes for finite element for the surface
d0=0.0003; %(m) OD of the fiber
Nf=1280; %number of hollow fibers
Dis=0.0254; %(m) ID of the shell side
Dh=((Dis^2)-(Nf*d0^2))/(Nf*d0); %(m) Hydraulic diameter on the shell
side
As=((Dis^2)-(Nf*d0^2))*3.14/4; %(m2) free flow area in the shell

%Initial Input condition
% ----------feed-------------
Tf=294; % (K) feed temperature
Vf_0=3/1000/60; % (m3/s) volume flow rate of air
Pf=patm; % (Pa) total pressure
x_CO2f_0=0.9; %initial feed CO2 molar fraction
Mu=15.314*10^-6;% (m2/s) kinematic viscosity
% ----------draw-------------
Vd_0=3/1000/60; % (m3/s) volume flow rate of air
Td=294; % (K) draw temperature
x_CO2d_0=0.00001; %initial draw CO2 molar fraction

% for Relative humidity input or different temperature is used to
calculate
% the molar fraction with certain humidity value
% RH=1; %relative humidity of the feed
% A=8.07131;% Antoine eq cst for water
% B=1730.63;% Antoine eq cst for water
% C=233.426;% Antoine eq cst for water
% Psat_H2O=(10^(A-B/(C+(T-273))))*133.32; % (Pa) water vapor
saturation pressure
% p_H2O=RH*Psat_H2O; % (Pa) partial pressure of the water vapor
% x_H2O=p_H2O/Pf; % molar fraction in the feed, for draw side xd=
pH2O/Pd.
    %diffusion D of CO2 in N2%
D0=1.44*10^-5; %(m2/s)
D=D0*(patm/Pf)*(Tf/T0)^1.75; % (m2/s) CO2 diffusion in N2
da=a/n; %area differential
deltapmax=1000; % (kPa) max pressure difference in the membrane


for i=1:deltapmax;
    deltap(i)=i*1000;
```

```
   % Initial molar flow rates on the draw and feed side
    nf_0=Vf_0*Pf/R/Tf; % (mol/s) feed molar flow rate
    nd_0=Vd_0*(Pf+deltap(i))/R/Td; % (mol/s) draw molar flow rate

   % Initial condition for feed and draw
    nf(i,1)=nf_0;
    nd(i,1)=nd_0;
    x_CO2f(i,1)=x_CO2f_0;
    x_N2f(i,1)=1-x_CO2f(i,1);
    x_CO2d(i,1)=x_CO2d_0;
    x_N2d(i,1)=1-x_CO2d(i,1);
    nf_CO2(i,1)=x_CO2f(i,1)*nf(i,1);
    nf_N2(i,1)=x_N2f(i,1)*nf(i,1);
    nd_CO2(i,1)=x_CO2d(i,1)*nd(i,1);
    nd_N2(i,1)=x_N2d(i,1)*nd(i,1);
    p_CO2f(i,1)=x_CO2f(i,1)*Pf;
    p_CO2d(i,1)=x_CO2d(i,1)*(Pf+deltap(i));
    p_N2f(i,1)=x_N2f(i,1)*Pf;
    p_N2d(i,1)=x_N2d(i,1)*(Pf+deltap(i));
    F=(1/patm)*(T0/Tf);
    f(i)=(Pf/(Pf+deltap(i)));
    uf=nf(i,1)*R*Tf/(Pf*As); % (m/s)Velocity of the gaz flux in the
shell side

k=0.0732*((Dh*100)^0.6)*((D*10000)^0.67)*((uf*100)^0.6)/(((d0*100)^0
.4)*((Mu*10000)^0.27)); %(cm/s)(overall mass transfer rate
coefficient)

    for j=1:n;
    xs(i,j)=(x_CO2f(i,j)*(k*0.01*F*f(i)+j0*(x_CO2d(i,j)*(b-1)+b*(f-
1)))+j0*x_CO2d(i,j))/(f*(k*0.01*F+j0*(1-x_CO2f(i,j)*(1-b))));

    % permeate flux per element da
    dn_CO2(i,j)=k_CO2*(Pf*xs(i,j)-p_CO2d(i,j))*da;%(mol/s)
    dn_N2(i,j)=abs(k_N2*(Pf*(1-xs(i,j))-p_N2d(i,j))*da);%(mol/s)

    %T_2(i)=Td*((Pf+deltap(i))/Pf)^((kc-1)/kc); %(K) temperature
after compression

    %Update the flux on the feed side
    nf_CO2(i,j+1)=nf_CO2(i,j)-dn_CO2(i,j); %(mol/s) feed CO2 molar
flux
    nf_N2(i,j+1)=nf_N2(i,j)+dn_N2(i,j);%(mol/s) feed N2 molar flux
    nf(i,j+1)=nf(i,j)-dn_CO2(i,j)+dn_N2(i,j); % total feed molar
flux
    x_CO2f(i,j+1)=nf_CO2(i,j+1)/nf(i,j+1); %feed CO2 molar fraction
    p_CO2f(i,j+1)=x_CO2f(i,j+1)*Pf;% (Pa)feed CO2 partial pressure
    x_N2f(i,j+1)=1-x_CO2f(i,j+1);
    p_N2f(i,j+1)=x_N2f(i,j+1)*Pf;

    %Update the flux on the draw side
```

```
    nd_CO2(i,j+1)=nd_CO2(i,j)+dn_CO2(i,j); %(mol/s) draw CO2 molar
flux
    nd_N2(i,j+1)=nd_N2(i,j)-dn_N2(i,j);%(mol/s) draw N2 molar flux
    nd(i,j+1)=nd(i,j)+dn_CO2(i,j)-dn_N2(i,j); % total draw molar
flux
    x_CO2d(i,j+1)=nd_CO2(i,j+1)/nd(i,j+1);%draw CO2 molar fraction
    p_CO2d(i,j+1)=x_CO2d(i,j+1)*(Pf+deltap(i));%(Pa)draw CO2 partial
pressure
    x_N2d(i,j+1)=1-x_CO2d(i,j+1);
    p_N2d(i,j+1)=x_N2d(i,j+1)*(Pf+deltap(i));
    xs(i,j+1)=(x_CO2f(i,j+1)*(k*0.01*F*f(i)+j0*(x_CO2d(i,j+1)*(b-
1)+b*(f-1)))+j0*x_CO2d(i,j+1))/(f*(k*0.01*F+j0*(1-x_CO2f(i,j+1)*(1-
b))));
    Cp(i,j)=xs(i,j)/x_CO2f(i,j);% concentration polarisation
    end
    m_CO2(i)=(sum(dn_CO2(i,:)))*44/1000/a; % (kg/s/m2) total CO2
(Mco2=44 g/mol) permeate mass flow density in the draw side
    ma_CO2(i)=(sum(dn_CO2(i,:)))*44/1000; % (kg/s) total CO2
(Mco2=44 g/mol) permeate mass flow in the draw side
    m_N2(i)=(sum(dn_N2(i,:)))*28/1000/a; % (kg/s/m2) total N2
(Mn2=28 g/mol) permeate mass flow density in the draw side
    m_tot(i)=(m_CO2(i)-m_N2(i))*a;%(kg/s) total flux

    P_ex_CO2(i)=m_CO2(i)*Rc*Td*(kc/(kc-1))
*(((Pf+deltap(i))/Pf)^((kc-1)/kc)-1)*1000; % (W/m2)CO2 flux expander
power density recovered
    P_ex(i)=m_tot(i)*Rc*Td*(kc/(kc-1))*(((Pf+deltap(i))/Pf)^((kc-
1)/kc)-1)*1000/a; % (W/m2)total flux expander power density
recovered

end
```

CHAPTER FOUR

FERTILIZER-BASED LIQUID DESICCANTS: A NOVEL CONCEPT FOR ENERGY EFFICIENT DEHUMIDIFICATION AND WATER VAPOR RECYCLING IN INDOOR PLANT ENVIRONMENTS

4.1 Original publication

Chapter Four is based primarily on a paper that was published in the Journal of Applied Thermal Engineering[3]. This publication was the first study to introduce and validate the use of fertilizer solution as a liquid desiccant in membrane-based dehumidification for indoor plant environment. While the use of liquid desiccant for dehumidification process was already proposed in the literature where a selective membrane is used to separate water vapor from a humid air feed stream into a concentrated desiccant solution, it is the first time that fertilizer is proposed as desiccant and a solution for energy saving.

4.2 Introduction

Indoor plant environments such as greenhouses and vertical farms, have the potential to improve crop yields, nutrition, and food security, while mitigating the environmental impacts of agriculture [74-78].

[3] S. Moussaddy, S. Pushparajah, J. Maisonneuve, "Fertilizer-Based Liquid Desiccants: A Novel Concept for Energy Efficient Dehumidification and Water Vapor Recycling in Indoor Plant Environments," Applied Thermal Engineering, 119529, 2022.

Among the requirements of operating indoor plant environments is the need to regulate indoor humidity levels for healthy plant physiology and production. More recently, liquid desiccant dehumidification has been proposed for indoor plant environments [79-81]. These have shown excellent performance for high precision humidity control. However, liquid desiccant solutions require energy intensive regeneration, and care must be taken to avoid releasing the typically toxic desiccant into either the water supply or the ambient air of the plant environment. For the potential of indoor plant environments to be fully realized, effective and energy efficient methods of controlling humidity and recovering water vapor are needed.

In this work, we introduce the novel concept of using fertilizer-based liquid desiccants to dehumidify indoor plant environments and recycle water vapor. Until now, the possibility of using fertilizer to drive dehumidification has not been mentioned in the literature. Figure 4.1 illustrates one embodiment of the concept applied to a membrane-based dehumidification cycle. In this process, concentrated fertilizer solution is circulated through a membrane contactor that is exposed to air from the ambient plant environment. The vapor pressure difference between the liquid desiccant and the air feed drives water vapor to permeate across the membrane, and hence water is recovered by the fertilizer as humidity is removed from the plant environment. When sufficiently diluted, fertilizer solution can be delivered directly to plants, closing the water cycle and eliminating the need for energy intensive regeneration of the desiccant. A detailed comparison with other dehumidification methods is provided in Supplementary Note 4.1.

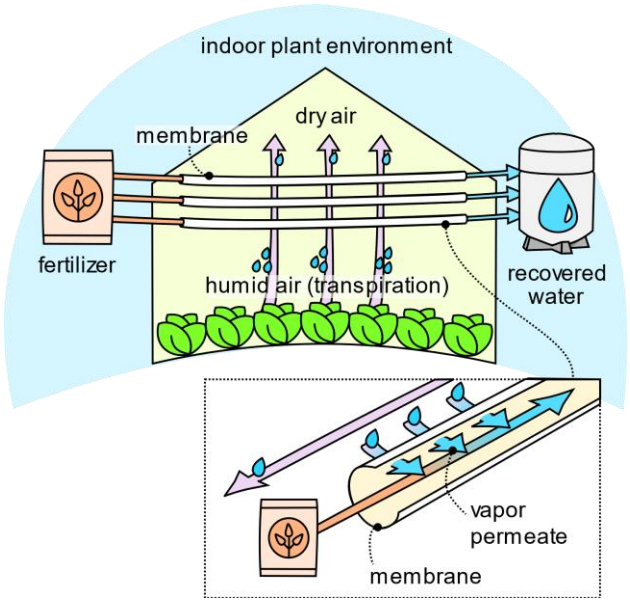

Figure 4.1. Water vapor permeate can be drawn from a humid air stream across a selective polymer membrane by a vapor pressure gradient established by a concentrated fertilizer-based liquid desiccant solution. This process can be used to dehumidify indoor plant environments and recycle water vapor for plant fertigation.

This study provides the first-ever experimental demonstration of dehumidification from fertilizer-based liquid desiccants. A laboratory-scale prototype of a membrane-based dehumidification process and test protocol are described, and the experimental results are presented here. Fundamental transport dynamics are outlined, and simulation results are compared against experimental observations. Performance is evaluated for a number of common fertilizers, across a range of typical greenhouse conditions, and across a range of possible operating conditions. While the chemical potential energy of concentrated fertilizer has previously been considered for other applications such as forward osmosis for water treatment [82-101] and pressure retarded osmosis for power generation [102-104], this is the first time that fertilizer energy has been considered as a driving force for dehumidification.

4.3 Theory

4.3.1 Dehumidification Potential of Concentrated Fertilizer Solutions

Concentrated fertilizer solutions exhibit high affinity to water vapor, just as typical liquid desiccant solutions do. As such, they tend to absorb water vapor across a range of conditions and therefore have potential for dehumidification applications. This tendency is described by the water vapor pressure of the solution, which when sufficiently low, drives water vapor absorption from the ambient air. Several methods for accurately modelling and predicting the vapor pressure of desiccant solutions can be considered, such as the Kohler equation which describes the vapor pressure of liquid desiccant solution $p_{H2O,D}$ as a function of the solution temperature T, hydraulic pressure p, and osmotic pressure π [105,106].

$$p_{H2O,D} = p_o \exp\left(\frac{V_m}{R\,T}(p - \pi)\right) \tag{4.1}$$

Where R is the gas constant and V_m is the molar volume of water. The osmotic pressure of the desiccant solution π can generally be described by the Van't Hoff equation. And the equilibrium vapor pressure of pure water p_o can generally be described by the Antonine equation.

$$\pi = i\,R\,T\,c \tag{4.2}$$

$$p_o = 10^{\left(A_o - \frac{B_o}{C_o + T}\right)} \tag{4.3}$$

Where i is the number of ions in the desiccant solution, c is the desiccant concentration, and A_o, B_o, and C_o are empirical coefficients.

Figure 4.2 provides an overview of the dehumidification potential of a range of common fertilizer solutions. The vapor pressure and equilibrium relative humidity are shown for

solutions at their solubility limit, assuming atmospheric pressure and room temperature. Several fertilizers such as ammonium nitrate NH_4NO_3 and calcium nitrate $Ca(NO_3)_2$ show significant potential, with vapor pressures that are comparable to that of conventional liquid desiccant such as magnesium chloride $MgCl_2$. As shown, the equilibrium of certain fertilizer solutions falls within the target humidity range of indoor plant environments.

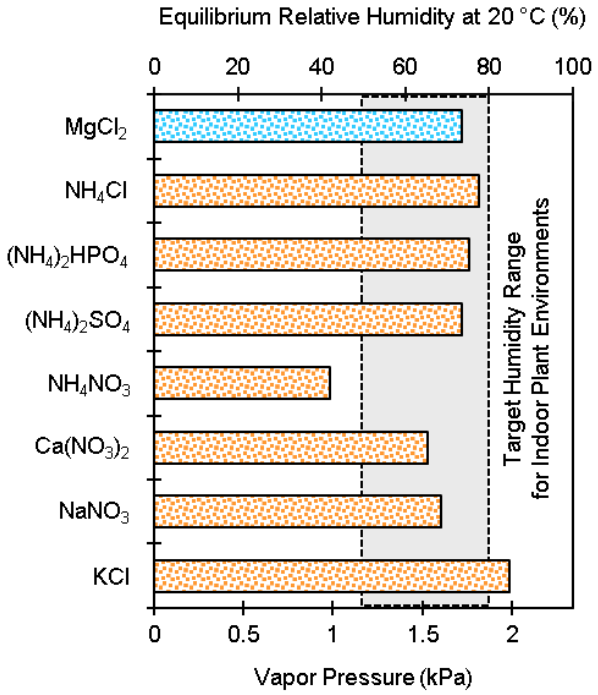

Figure 4.2. Vapor pressure and equilibrium humidity of common fertilizer solutions at their solubility limit, assuming atmospheric pressure and room temperature (101.3 kPa and 20 °C). For reference, potential is compared to that of conventional liquid desiccant solution magnesium chloride $MgCl_2$. The solubility limit of each salt is specified in Supplementary Note 4.2.

4.3.2 Vapor Permeate Across a Dense Membrane

The potential of fertilizer liquid desiccant can be exploited in a number of dehumidification processes, such as in a variety of desiccant spray systems and absorption columns [46-48]. In this study, we select a membrane-based dehumidification process to demonstrate the potential of fertilizer-based liquid desiccants. This process offers several

advantages, including protection of the conditioned environment from harsh desiccant droplets, which may carry-over in traditional direct contact liquid desiccant systems [107,108].

A membrane-based liquid desiccant dehumidification process uses a selective polymer core to separate concentrated desiccant solution from a humid air feed stream. In such a system, water vapor molecules from the air feed are driven by the vapor pressure gradient to absorb at the surface of the membrane, diffuse through the dense polymer, and then desorb and condense on the liquid desiccant surface.

The rate of water vapor mass transfer $\Delta\dot{m}$ can be defined as a function of the vapor pressure difference across the membrane Δp_{H2O}, and the mass transfer coefficient, K. When normalized per unit membrane area a, the water vapor flux J is expressed as follows:

$$J = \frac{\Delta\dot{m}}{a} = K\,\Delta p_{H2O} \tag{4.4}$$

In a simplified analysis, the vapor pressure difference across the membrane can be approximated by the balance between the bulk air feed and liquid desiccant vapor pressures, $p_{H2O,F} - p_{H2O,D}$. The vapor pressure of liquid desiccant solution $p_{H2O,D}$ was previously defined in equation (4.1). And the partial pressure of water vapor in the air feed $p_{H2O,F}$ can be expressed as a function of the mole fraction of water x_F and the hydraulic pressure of the air feed p_F as in equation (4.5), or of the relative humidity rh_F and saturation pressure p_o as in equation (4.6).

$$p_{H2O,F} = x_F\, p_F \tag{4.5}$$

$$p_{H2O,F} = rh_F\, p_o \tag{4.6}$$

In reality however, the vapor pressure difference across the membrane will be significantly less than the difference between the bulk fluids. Figure 4.3 illustrates the non-linear vapor pressure gradient that forms across the boundary layers at both surfaces of the membrane, as caused by temperature and concentration polarization (described in Sections 4.3.3. and 4.3.4.). The resulting vapor pressure difference across the membrane is then the balance between the air feed and liquid desiccant vapor pressures at the membrane surfaces, $\Delta p_{H2O} = p_{H2O,F,m} - p_{H2O,D,m}$.

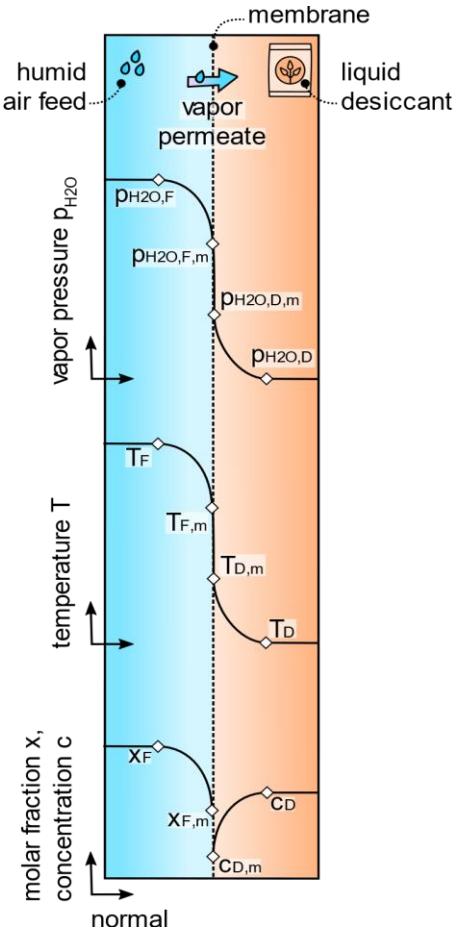

Figure 4.3. Vapor flux in a membrane-based liquid desiccant dehumidification process is driven by the water vapor pressure difference between liquid desiccant and humid air feed. The vapor pressure difference across the membrane will be a function of the non-linear temperature and concentration gradients.

4.3.3 Thermal Gradients and Heat Transfer Dynamics

The performance of liquid desiccant dehumidification is significantly affected by thermal and heat transfer dynamics. This is largely because the vapor pressure of liquid desiccants is strongly dependent on solution temperature. This is illustrated in Figure 4.4, which shows the theoretical vapor pressure of a selection of fertilizer solutions as a function of liquid desiccant temperature, as predicted by the Antoine and Kohler equations (4.1-3). For this reason, thermal gradients are often maintained between warm air and cool liquid desiccant to increase the driving vapor pressure difference between air feed and liquid desiccant, and thereby increase dehumidification [107,110]. Careful consideration of heat transfer dynamics and resulting temperature gradients is therefore needed to accurately describe the dehumidification process.

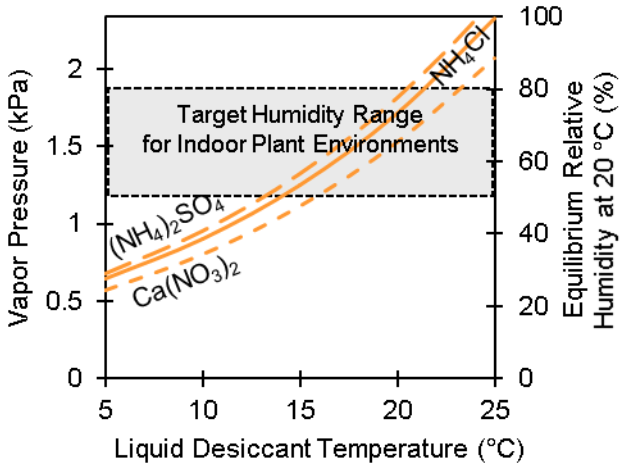

Figure 4.4. Vapor pressure as a function of temperature for fertilizer liquid desiccants at their solubility limit. For reference, the target vapor pressure of plant environments is provided, along with its equivalent relative humidity.

Thermal dynamics will be significant in two principal ways. First, heat transfer between warm air and cool liquid desiccant will introduce a temperature gradient normal to the membrane surface (i.e., in the direction of vapor permeate), such that temperatures on both

sides of the active membrane will be different from the bulk fluid temperatures. The resulting temperature profile was previously illustrated in Figure 4.3. Because vapor pressure is sensitive to temperature, these membrane surface temperatures will cause the driving vapor pressure difference across the membrane to be significantly less than the vapor pressure difference of the bulk fluids, ultimately resulting in lower water vapor transfer and dehumidification. Second, heat transfer between warm air and cool liquid desiccant will introduce a temperature gradient in the axial direction (i.e., in the direction of air feed and liquid desiccant circulation), such that circulating fluids will exit the membrane module at a different temperature than they entered, again resulting in lesser dehumidification performance.

To evaluate the temperature profiles that are axial and normal to the membrane surface, and their effect on water vapor transfer, it is necessary to define how heat is transferred across the membrane and its boundary layers. In such a system, heat transfer will be driven by three mechanisms: (1) thermal diffusion through the membrane and through the liquid and gas boundary layers, (2) heat that is carried by the mass transport of warm water vapor molecules across the membrane, and (3) heat of condensation that is released by the permeate phase change that occurs at the liquid desiccant surface. Each of these three heat transfer mechanisms is normalized per unit membrane area and expressed as heat flux $\dot{q}$ in equations (4.7-9).

$$\dot{q}_{diffusion} = \frac{\Delta T}{r} \tag{4.7}$$

$$\dot{q}_{sensible} = J\, c_p\, T \tag{4.8}$$

$$\dot{q}_{latent} = J\, H_c \tag{4.9}$$

Where c_p is the specific heat capacity of the fluid, H_c is the heat of condensation, and r is the thermal resistivity across a finite temperature difference ΔT. Thermal resistivity across the membrane will be r = L/k, where L and k are the membrane thickness and thermal conductivity. Thermal resistivity across the membrane boundary layers will be r = 1/h, where h_F and h_D are the thermal convection coefficients across the air feed and liquid desiccant boundary layers.

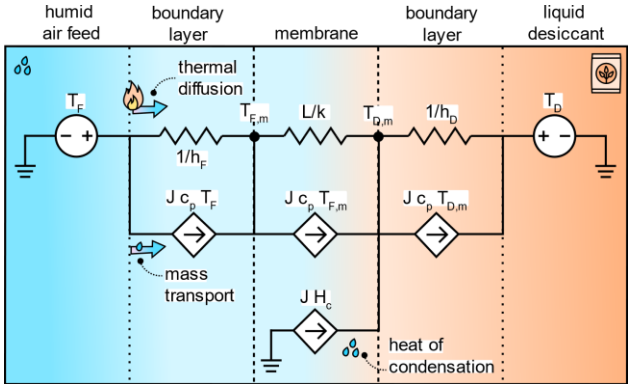

Figure 4.5. Thermal equivalent circuit showing heat transfer across the membrane and its thermal boundary layers. Mechanisms of heat transfer include diffusion, mass transport of vapor permeate, and heat of condensation at the liquid desiccant surface.

The temperature on both the air feed and liquid desiccant surfaces of the membrane $T_{F,m}$ and $T_{D,m}$ can then be described as a function of these heat transfer vectors by applying steady state conservation of energy to a control volume at both surfaces, and assuming no losses to the surroundings. A simplified thermal equivalent circuit of such an analysis is provided in Figure 4.5, and the resulting governing equations are provided in equations (4.10) and (4.11) [42,111-113].

$$\dot{q}_F = \left(T_F - T_{F,m}\right) h_F \; + \; J \, c_p \, T_F \; = \; \left(T_{F,m} - T_{D,m}\right) \frac{k}{L} + J \, c_p \, T_{F,m} \qquad (4.10)$$

$$\dot{q}_D = \left(T_{F,m} - T_{D,m}\right)\frac{k}{L} + J\, c_p\, T_{F,m} + J\, H_c$$
$$= \left(T_{D,m} - T_D\right) h_D + J\, c_p\, T_{D,m} \tag{4.11}$$

Where $\dot{q}_F$ is the rate at which heat is lost by the air feed and $\dot{q}_D$ is the rate at which heat is gained by the liquid desiccant. This rate of heat loss and gain will in turn define the axial variation in temperature observed in both the air feed and liquid desiccant as they circulate along the membrane. This change in temperature $T_{out} - T_{in}$ can be defined by considering the mass and energy balance over some finite membrane surface area Δa along the membrane, which yields equations (4.12) and (4.13).

$$\frac{T_{F,out} - T_{F,in}}{\Delta a} = -\frac{\dot{q}_F}{\dot{m}_F\, c_p} \tag{4.12}$$

$$\frac{T_{D,out} - T_{D,in}}{\Delta a} = \frac{\dot{q}_D}{\dot{m}_D\, c_p} \tag{4.13}$$

Where $\dot{m}$ is the circulation rate of either air feed or liquid desiccant.

4.3.4 Concentration Gradients and Mass Transfer Dynamics

The performance of liquid desiccant dehumidification will also be affected by concentration gradients that develop as a result of mass transfer dynamics. In particular, boundary layers at both the air feed and liquid desiccant sides of the membrane will develop as a function of the permeate diffusivity within the bulk fluids. These boundaries will introduce additional resistance to vapor permeate between fluids, and should be considered in the overall mass transfer coefficient, which is defined as:

$$K = \left(\frac{1}{K_F^{-1} + K_m^{-1} + K_D^{-1}}\right) \tag{4.14}$$

The mass transfer coefficient across the membrane K_m is the ratio of vapor permeability of the membrane B, and membrane thickness L (i.e. K_m = B/L). The mass transfer coefficient across the liquid desiccant boundary K_D is neglected, as water concentration of the liquid desiccant will change only negligibly [53]. And the mass transfer coefficient across the feed boundary layer K_F is defined by the following expression which has been proposed for gas flow in a hollow fiber membrane [46,69,114]:

$$K_F = 0.0732 \frac{p}{p'} \frac{T'}{T} \frac{D}{d^{0.4}} Re^{0.6} Sc^{0.33} \quad (4.15)$$

Where D is the diffusivity of water vapor in air, Re is the Reynolds number (=d_h u/ν), Sc is the Schmidt number (=ν/D), d is the fiber outer diameter, d_h is the hydraulic diameter, u is the flow velocity, ν is the kinematic viscosity, and T' = 0 °C and p' = 100 kPa are the standard temperature and pressure.

The resulting mass permeate across the membrane will in turn introduce axial variation in water concentrations observed in both the air feed and liquid desiccant, as they circulate along the membrane. The change in humidity mass ratio $w_{out} - w_{in}$ can be defined by considering the mass balance over some finite membrane surface area Δa along the membrane, which yields equations (4.16) and (4.17).

$$\frac{w_{F,out} - w_{F,in}}{\Delta a} = -\frac{J}{\dot{m}_F} \quad (4.16)$$

$$\frac{w_{D,out} - w_{D,in}}{\Delta a} = \frac{J}{\dot{m}_D} \quad (4.17)$$

4.4 Materials and Methods

4.4.1 Numerical Analysis

The performance of fertilizer-based dehumidification was simulated in Matlab (R2018a, Mathworks, Natick, MA) using a numerical model developed from the transport equations described in Section 4.3. The model takes a 2-D finite element approach to discretize a hollow fiber membrane in both the radial and axial dimensions, and then solve the energy and mass balance for a control volume defined at each element. In particular, temperature, concentration, and vapor pressures at the membrane surfaces are numerically solved and used to define the vapor pressure difference between liquid desiccant and air feed across each membrane element. More complete 3-D transport models are available in the literature [115,116], but because the primary objective of this study is to provide a proof of concept for the proposed dehumidification method, this 2-D modelling approach is sufficient for identifying the primary transport mechanisms responsible for the observed phenomena [69,117]. Additional detail of the modelling approach is provided in Supplementary Note 4.3. and the complete MATLAB script is provided in Supplementary Note 4.6.

A summary of the simulation input parameters is provided in Table 4.1-3. Vapor permeability and thermal conductivity of a dense polydimethylsiloxane membrane are specified by the manufacturer and confirmed in the literature [72,118]. Thermal resistivities of membrane boundary layers are defined with empirical expressions for convection coefficients, selected from the literature for flow through hollow fiber channel configurations [119-121]. k_D and k_F are the thermal conductivities of the liquid desiccant and air feed, d is the is the diameter of the hollow fiber lumen, d_h is the hydraulic diameter of the shell side of the membrane module, Re is the Reynolds number, and Pr is the Prandtl

number. Other simulation parameters are consistent with experimental test conditions, as described further in Section 4.4.2.

Table 4.1. Simulation input parameters

Membrane vapor permeability B	3.94×10^{-6} g m^{-2} s^{-1} Pa^{-1} [72]
Membrane thermal conductivity k	0.19 W m^{-1} K^{-1} [118]
Convection coefficient of liquid desiccant thermal boundary h_D	$0.36 \frac{k_D}{d_h} Re^{0.55} Pr^{0.33}$ [119,120]
Convection coefficient of air feed thermal boundary h_F	$0.023 \frac{k_F}{d} Re^{0.8} Pr^{0.3}$ [119,121]

4.4.2 Experimental Analysis

Fertilizer dehumidification was experimentally demonstrated, and the proposed transport model was validated using a series of laboratory tests. The experimental apparatus is shown in Figure 4.6 The system consists of a membrane module that is supplied by a gas feed line and a liquid desiccant line. The liquid desiccant line is equipped with a positive displacement diaphragm pump (SFDP1-030-045-33, Seaflo, Xiamen, China) that delivers fluid from a 2-L sealed reservoir mounted on a mass balance (AX8201, Ohaus, Parsippany, NJ). Flow rate of the liquid desiccant is controlled by adjusting DC voltage applied to the pump motor and is then measured with a mass flow meter (8051K107, McMaster-Carr, Elmhurst, IL). Pulsations in the flow are dampened via an inline accumulator tank (SFAT-075-125-01, Seaflo, Xiamen, China). Temperature of the liquid desiccant is controlled by circulating fluid through a stacked-plate heat exchanger (35115K62, McMaster-Carr, Elmhurst, IL) that is supplied with a working fluid, maintained at the target temperature by a thermostatically controlled bath (TC550-SD, Brookfield, Middleboro, MA). Temperature

is then measured at both the membrane inlet and outlet via thermal resistance sensors (800-32/140-1188, Noshok, Berea, OH) mounted in thermowells (75-025-316SS, Noshok, Berea, OH) for protection. All lines are insulated with at least R-2 foam tubing.

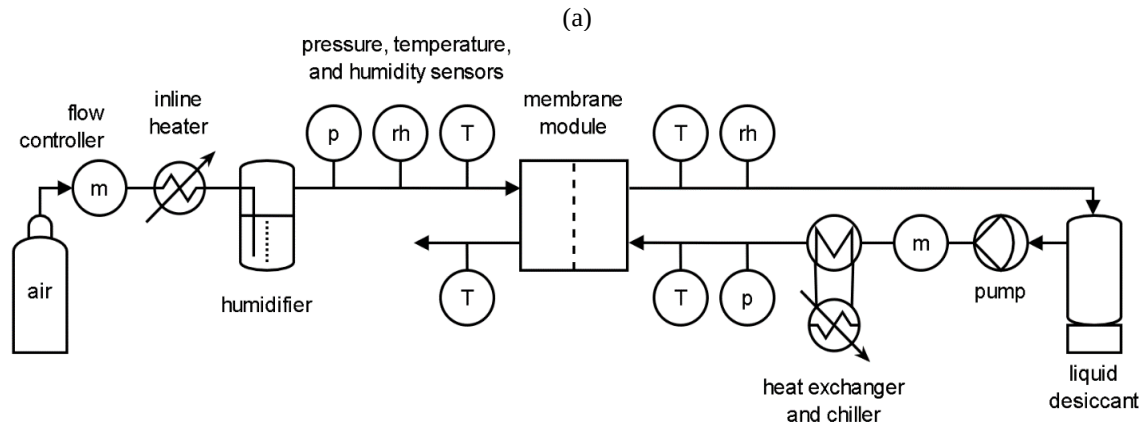

Figure 4.6. (a) Schematic and (b) photo of the liquid desiccant dehumidification test bench. The laboratory bench consists of a membrane module that is supplied by air feed and liquid desiccant at controlled temperature, humidity, pressure, and flow. (c) Photo of the hollow fiber membrane module.

On the gas side, air feed is supplied by compressed air that is heated as it circulates through an inline electric resistance heater (AHP-3742, Omega, Norwalk, CT), and then humidified as it bubbles through deionized water columns. Temperature is controlled by adjusting DC voltage applied to the resistance heater, and humidity is controlled by blending a parallel air stream that by-passes the humidifiers. Temperature and humidity are

measured by thermistor temperature sensors and capacitive humidity sensors (AM2315, Aosong Electronics, Guangzhou, China) installed at both the membrane inlet and outlet. Flow rate of the air feed is controlled by a mass flow controller (GH-32907-69, Masterflex, Radnor, PA). Pressure at both the air feed and liquid desiccant inlets are regulated to almost atmospheric pressure and monitored and recorded using a differential pressure transducer (GC557F0142CD, Ashcroft, Stratford, CT). All sensor data is recorded via 1-5 Vdc linear interpolation and recorded by a data acquisition module (OM-USB-1608FS, Omega, Norwalk, CT) connected to a PC. A dense polymer membrane was selected for this study, and the commercial hollow fiber module (PDMSXA-1.0, Perm Select, Ann Arbor, MI) was mounted on the test bench shown in Figure 4.6(c).

Table 4.2. Membrane specifications

Material	polydimethylsiloxane
Module type	hollow fiber
Membrane area a	1 m^2
Fiber length	0.14 m
Fiber diameter (outer) d	300×10^{-6} m
Fiber thickness L	55×10^{-6} m
Number of fibers	12,600
Flow orientation	counter flow

Key membrane specifications as provided by the manufacturer are summarized in Table 4.2. Tests were conducted across a range of environmental and operating conditions, including a range of feed air temperature, feed air humidity, fertilizer desiccant temperature, and fertilizer desiccant concentration. Three common fertilizer solutes were

selected, namely, ammonium chloride NH_4Cl, ammonium sulfate $(NH_4)_2SO_4$, and calcium nitrate $Ca(NO_3)_2$. A summary of experimental test conditions is provided in Table 4.3.

Table 4.3. Experimental test conditions

Liquid Desiccant Supply	
Fertilizer solute	$Ca(NO_3)_24H_2O$, NH_4Cl, $(NH_4)_2SO_4$
Concentration	45 - 95 % solubility
Temperature	2 - 20 °C
Mass flow	2 lpm
Pressure	35 kPa (gauge)
Air Feed Supply	
Humidity	70 - 90 %rh
Temperature	20 - 30 °C
Mass flow	5 slpm
Pressure	31 kPa (gauge)

Dehumidification rates were evaluated by considering the change in liquid desiccant mass as described in equation (4.18), and then verified by analyzing the change in air feed humidity as described in equation (4.19).

$$J = \frac{\Delta m}{a\,\Delta t} \tag{4.18}$$

$$J = \frac{\dot{m}_F}{a}\left(\frac{rh_{in}\,\frac{p_{sat,in}}{p_F}}{1 - rh_{in}\,\frac{p_{sat,in}}{p_F}} - \frac{rh_{out}\,\frac{p_{sat,out}}{p_F}}{1 - rh_{out}\,\frac{p_{sat,out}}{p_F}}\right)\frac{M_{H2O}}{M_{N2}} \tag{4.19}$$

Where Δm is the change in liquid desiccant mass that is observed at the AX8201 balance ($\pm$ 0.1 g), Δt is the length of the test trial recorded by the OM-USB-1608FS data acquisition system ($\pm$ 1.5 s), $\dot{m}_F$ is the air feed flow rate observed at the GH-32907-69 mass flow controller ($\pm$ 0.05 slpm), rh is the relative humidity of inlet and outlet air feed observed by the AM2315 i2C humidity sensors ($\pm$ 2 % rh), p_F is the air feed pressure observed by the

GC557F0142CD pressure transducer (± 2.4 kPa), and p_{sat} is the saturation pressure of inlet and outlet air feed that is obtained as a function of temperature, as observed by the AM2315i2C temperature sensors (± 0.3 °C). A detailed record of raw data, analytical methods, and uncertainty analysis is provided in Supplementary Note 4.4, and a complete dataset of raw measured results is provided in Supplementary Note 4.5.

4.5 Results

4.5.1 Dehumidification and Water Recovery Across a Range of Plant Environment Conditions

Figures 4.7 and 4.8 show the fertilizer-based dehumidification concept across a range of typical greenhouse and indoor farming conditions, where air temperature ranges from 20-30 °C, and target relative humidity ranges from 50-80 %. As expected, environments with higher air humidity will experience more rapid water vapor transfer across the selective membrane layer, and hence a greater amount of water vapor removal from the air feed stream. This is a result of the driving vapor pressure gradient that is proportional to air feed humidity. The effect on outlet humidity however is negligible and remains nearly constant at approximately 60 % relative humidity across all the range of tested inlet humidities. This is nearly equal to the equilibrium point of the selected desiccant and suggests that the membrane module and the amount of circulating liquid desiccant may be oversized relative to the amount of air feed supply, and therefore, in all cases the air stream simply reaches equilibrium with the liquid desiccant.

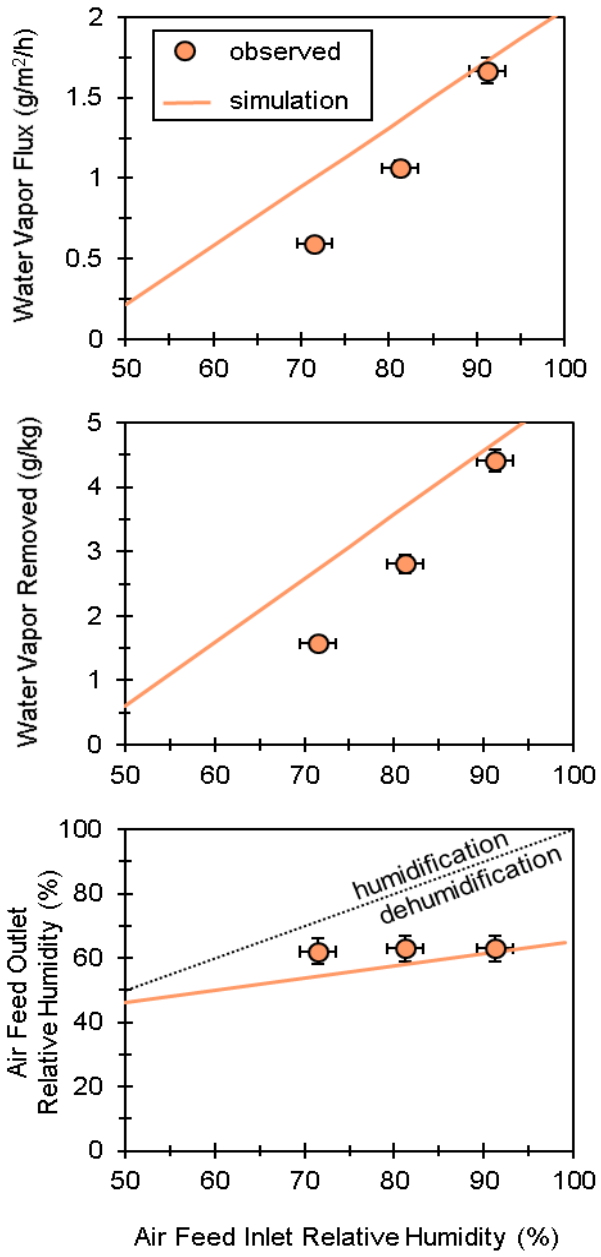

Figure 4.7. Water vapor flux, water vapor removed per unit dry air, and air feed outlet humidity at equivalent inlet temperature, across a range of air feed greenhouse humidities. Given liquid desiccant solution with $Ca(NO_3)_2$ fertilizer at concentration of 997.1 ± 0.2 g/l and temperature of 13.8 ± 0.3 °C, and given air feed at temperature of 25.6 ± 0.1 °C. Other test conditions are specified in Table 4.3.

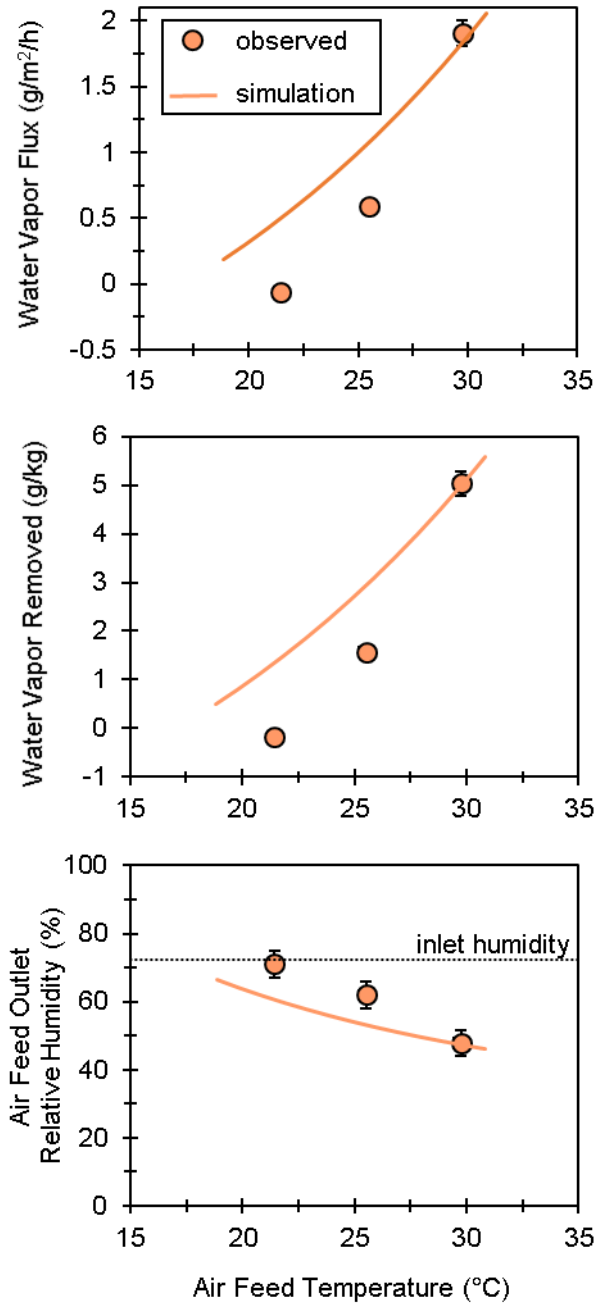

Figure 4.8. Water vapor flux, water vapor removed per unit dry air, and air feed outlet humidity at equivalent inlet temperature, across a range of air feed greenhouse temperatures. Given liquid desiccant solution with $Ca(NO_3)_2$ fertilizer at concentration of 996.9 ± 0.2 g/l and temperature of 13.8 ± 0.3 °C, and given air feed with 72 ± 2 % relative humidity. Other test conditions are specified in Table 4.3.

Similarly, environments with higher air temperatures will also experience higher water vapor flux, due to the increased water content and vapor pressure at a given relative humidity. Again, this leads to greater amounts of water vapor removal from the air feed, but no significant effect on the outlet humidity, since the process approaches equilibrium in all cases due to the oversized membrane area and liquid desiccant volumes. In other words, under the specified test bench operating conditions, the outlet air feed humidity appears to be limited simply by the equilibrium vapor pressure of the liquid desiccant, and not by the air feed temperature or humidity.

These results provide the first-ever demonstration of fertilizer-based desiccant dehumidification. Simulation results show reasonable agreement with experimental data, suggesting that major trends and dominant transport dynamics are accounted for.

4.5.2 Dehumidification and Water Recovery Across a Range of Operating Conditions

Figure 4.9 shows the dehumidification concept with a selection of common fertilizer solutions, including calcium nitrate $Ca(NO_3)_2$, ammonium chloride NH_4Cl, and ammonium sulfate $(NH_4)_2SO_4$ each at concentrations equivalent to approximately 75 % of room-temperature solubility. Vapor flux (between 0.59 and 0.66 $g/m^2/h$) and vapor removed (between 1.57 and 1.76 g/kg) are shown to be nearly the same for each fertilizer, suggesting that a broad range of fertilizers could potentially be used for liquid desiccant applications, provided that the environmental and operating conditions are favorable.

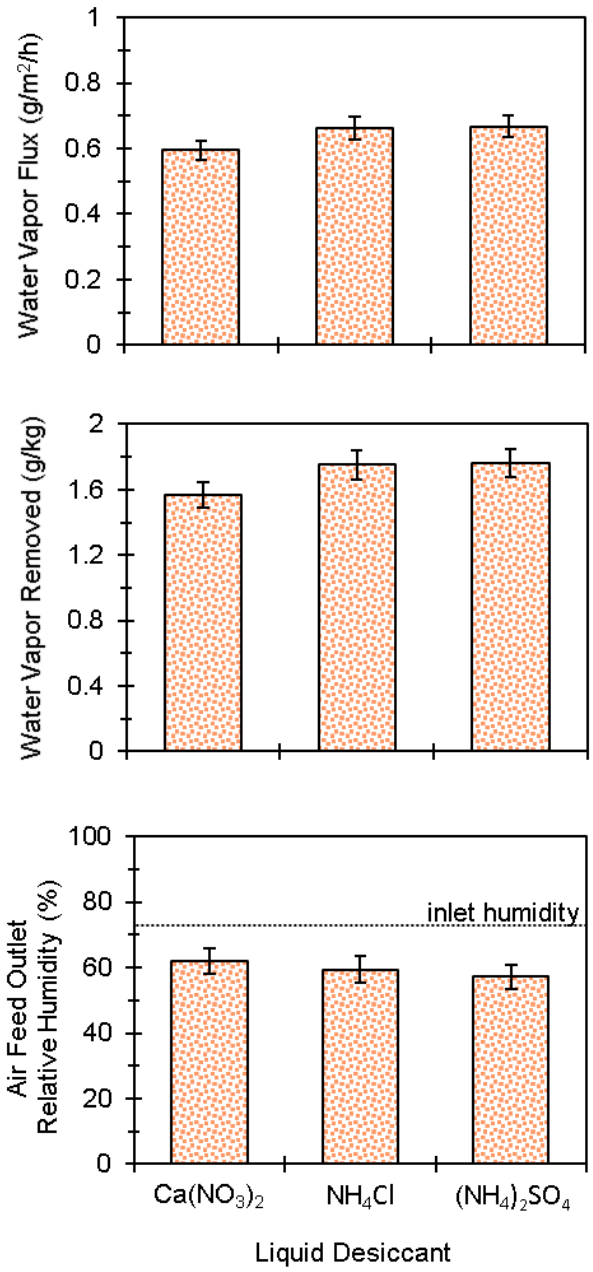

Figure 4.9. Water vapor flux, water vapor removed per unit dry air, and air feed outlet humidity at equivalent inlet temperature, for a variety of fertilizer solutes. Given liquid desiccant solution with temperature of 13.8 ± 0.3 °C and concentrations of 996.7 ± 0.2 g/l for calcium nitrate $Ca(NO_3)_2$, 285.6 ± 0.1 g/l for ammonium chloride NH_4Cl, and 575.4 ± 0.1 g/l for ammonium sulfate $(NH_4)_2SO_4$, or roughly 75 % of the room temperature solubility limit of each fertilizer. Also, given air feed with temperature of 25.2 ± 0.1 °C and 71 ± 2 % relative humidity. Other test conditions are specified in Table 4.3.

While environmental conditions will be specified mostly by the greenhouse crop's temperature and humidity requirements, the dehumidification process can presumably be operated at a range of liquid desiccant temperatures and concentrations. Figures 4.10 and 4.11 show the fertilizer-based dehumidification concept across a range of possible operating conditions, including liquid desiccant temperatures from 2-20 °C and concentrations from 500-1300 g/l, which is equivalent to roughly 45-100 % of the solubility limit. Simulation results are included and again show reasonable agreement with experimental data, accounting for major trends and correctly identifying dominant transport dynamics.

As shown, decreasing the temperature of the fertilizer liquid desiccant leads to significantly more rapid water vapor transfer, and hence greater quantities of water vapor removal from the air feed. For example, a drop in desiccant temperature from 20 to 10 °C leads to an over 10-fold increase in water vapor flux.

This is expected, as the vapor pressure of solution is strongly dependent on temperature, as shown previously in Figure 4.4. In addition, a drop in the outlet air feed humidity is observed, because the equilibrium vapor pressure of the solution, which was previously identified as the primary limiting factor of this process, is significantly reduced at lower liquid desiccant temperatures. The observed sensitivity to desiccant temperature provides insight into possible operational strategies for managing high rates of water vapor transfer, assuming of course that the energy costs of cooling desiccant could be technically and economically justified.

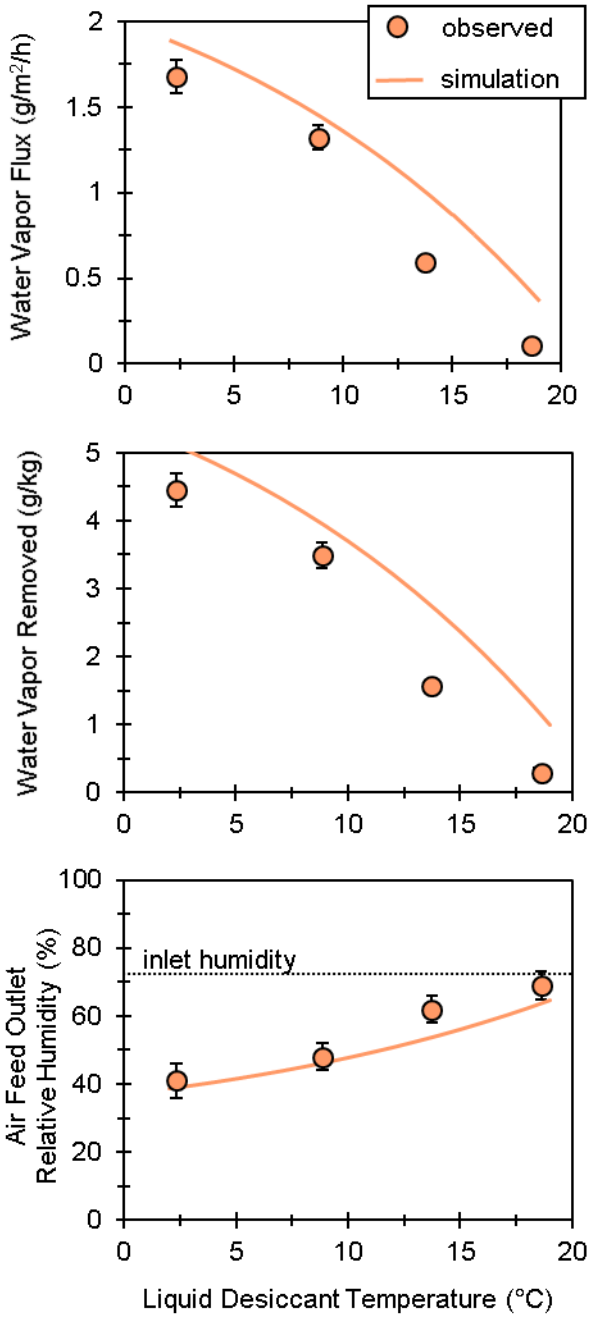

Figure 4.10. Water vapor flux, water vapor removed per unit dry air, and air feed outlet humidity at equivalent inlet temperature, across a range of liquid desiccant temperatures. Given liquid desiccant solution with $Ca(NO_3)_2$ fertilizer at concentration of 996.7 ± 0.2 g/l, and given air feed with temperature of 25.3 ± 0.1 °C and 71 ± 2 % relative humidity. Other test conditions are specified in Table 4.3.

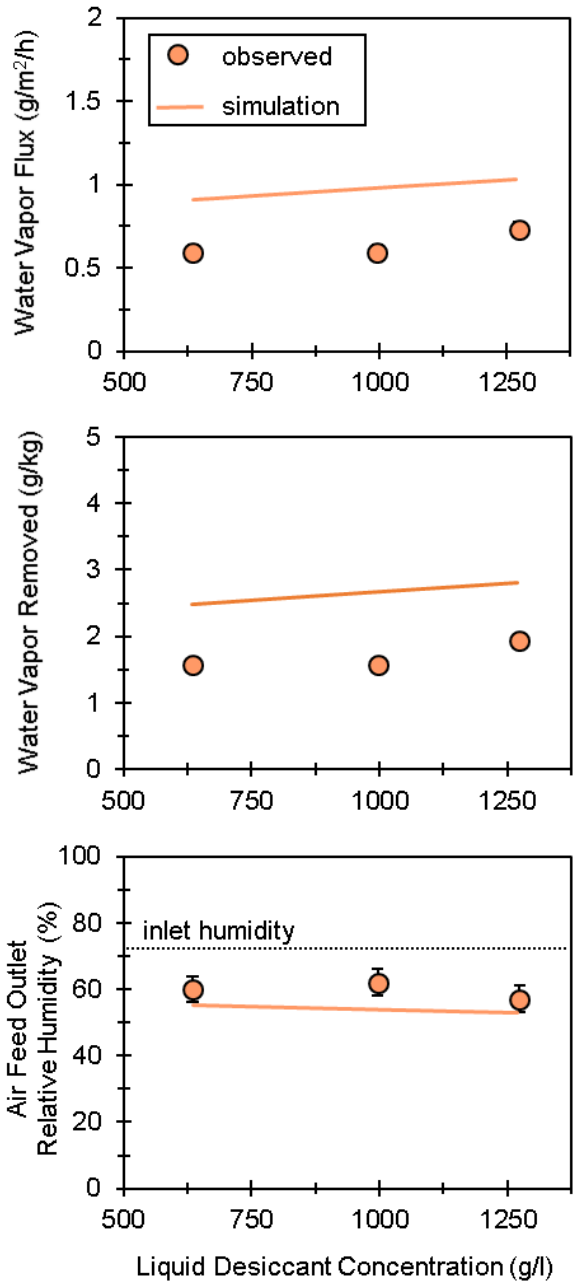

Figure 4.11. Water vapor flux, water vapor removed per unit dry air, and air feed outlet humidity at equivalent inlet temperature, across a range of liquid desiccant concentrations. Given liquid desiccant solution with $Ca(NO_3)_2$ fertilizer at temperature of 13.8 ± 0.3 °C, and given air feed with temperature of 25.2 ± 0.1 °C and 71 ± 2 % relative humidity. Other test conditions are specified in Table 4.3.

In contrast, the dehumidification performance is shown in Figure 4.11 to be only modestly influenced by liquid desiccant concentration. Water vapor flux and water vapor removed from the air feed are observed to decrease only slightly as desiccant concentration is adjusted from near the solubility limit down to approximately 45 % of the limit. This is expected from the theory as described by equations (4.1)-(4.3). This is meaningful because it is likely that the liquid desiccant process will be operated as a batch process, with a given quantity of fertilizer to be specified by the needs of a selected plant crop, and therefore the batch of liquid desiccant solution will likely be diluted over time as it recirculated. It should be noted however, that as the batch of liquid desiccant solution is continuously circulated, its concentrations will eventually drop well below the range explored in Figure 4.11, and at some point, its dehumidification potential will be reduced. The dynamics and limitations associated with these batch process dynamics should be carefully considered in future work.

4.6 Conclusions

In this study we have introduced and experimentally validated the novel concept of using fertilizer-based solutions as liquid desiccants for dehumidification of indoor plant environments. Fertilizer liquid desiccant was circulated through the lumen of a polydimethylsiloxane PDMS hollow fiber membrane, and rates of water vapor permeate were observed under a range of greenhouse and operating conditions. A variety of common fertilizer solutions were shown to perform nearly equally as well as one another, including $Ca(NO_3)_2$, NH_4Cl, and $(NH_4)_2SO_4$, suggesting that a wide variety of fertilizers can be

considered for such a system. This is the first time that fertilizer-based dehumidification has been demonstrated in the literature.

Up to 1.90 $g/m^2/h$ of water vapor flux and 5.03 g/kg of water vapor removal was observed under favorable conditions. Such water vapor flux is relatively low compared to dehumidification rates observed in other liquid desiccant and membrane processes [122,123]. However, this is largely a result of the fact that the membrane module used in this study was oversized, and air feed often exited the unit at equilibrium with the liquid desiccant. It is likely therefore that some portion of the membrane surface was rendered largely ineffective. Using a small membrane surface would presumably increase vapor flux, as would other measures such as selection of a highly permeable membrane.

Vapor permeation rates are important because maintaining target indoor humidity will largely depend on balancing dehumidification rates with plant transpiration rates. In cases where flux is low, larger membrane areas will be required to achieve target vapor removal rates, adding to the capital cost of such a system. Alternatively, maintaining thermal gradients between warm feed air and cool liquid desiccant was shown to be a key variable for achieving high dehumidification rates, as is consistent with other conventional liquid desiccant dehumidification systems [120,124,125]. Higher flux can be achieved by operating at cool liquid desiccant temperatures, although this will add to operational costs, and the energy implications of additional cooling requires further analysis.

More fundamentally, additional analysis is required to consider the dynamics and limits of fertilizer-based liquid desiccant dehumidification when it is operated as a batch process. Results from this study show that dehumidification rates are only modestly affected by concentration, but it is expected that the effect of concentration will become increasingly

important as a given batch of fertilizer solution is recirculated and diluted over time, and at some point, vapor equilibrium will be established. This equilibrium point will impose an upper limit on the amount of water vapor that can be recovered, and hence the amount of energy that can be economized from a batch of fertilizer. Since any given plant crop will require only a certain amount of fertilizer per unit time, these limits should be evaluated and compared against the evapotranspiration rates that are expected from the plant crop over the same period. Moreover, the balance between evapotranspiration and dehumidification rates will be dynamic and vary with day/night, weather, plant development, and as the fertilizer concentration is diluted. Investigating these bath process dynamics and limits is proposed for future study. Other important dynamics for further consideration should include analysis of thermal management strategies such as controlled liquid desiccant cooling, which interestingly, could be used to overcome the aforementioned limits of batch-process dilution, although again, the operational energy costs of such a strategy would need to be economically and technically justified.

In conclusion, the primary objectives of this work have been achieved, which have been to analytically and experimentally demonstrate the possibility of using common fertilizer solution for liquid desiccant dehumidification. This contribution to the literature may open up new possibilities for energy efficient dehumidification and water recycling in indoor plant environments.

4.7 Nomenclature

a	membrane surface area (m^2)
B	vapor permeability ($g\ m^{-2}\ s^{-1}\ Pa^{-1}$)

c	concentration of desiccant solute (mol l^{-1})
c_p	specific heat (J K^{-1} g^{-1})
d	diameter (m)
d_h	hydraulic diameter (m)
H_c	heat of condensation (J g^{-1})
h	thermal convection coefficient (W m^{-2} K^{-1})
i	number of ions
J	vapor flux (g m^{-2} s^{-1})
K	mass transfer coefficient (g m^{-2} s^{-1} Pa^{-1})
k	thermal conductivity (W m^{-1} K^{-1})
L	membrane thickness (m)
M	molar mass (g mol^{-1})
m	mass (g)
Pr	Prandtl number
p	pressure (Pa)
$\dot{q}$	heat flux (W m^{-2})
R	gas constant (J mol^{-1} K^{-1})
Re	Reynolds number
r	thermal resistance (K m^2 W^{-1})
rh	relative humidity (%)
x	mole fraction of water (mol/mol)
T	temperature (K)
V_m	molar volume (m^3 mol^{-1})
w	humidity mass ratio (g g^{-1})

Greek symbols:

π	osmotic pressure (Pa)

Subscripts and Superscripts:

'	standard temperature and pressure
D	liquid desiccant
F	air feed

H2O	water / vapor
in	membrane module inlet
m	membrane surface
o	pure water / saturation
out	membrane module outlet

4.8 Supplementary Notes

4.8.1 Supplementary Note 4.1: Advantages of Fertilizer-Based Liquid Desiccant Dehumidification

Table S4.1. provides a summary of the advantages of the proposed system relative to the current state of the art of humidity and water recovery methods for controlled plant environments (CPE). Typically, humidity is controlled via ventilation, where indoor humid air is rejected to the outside and replaced with fresh dry air. While simple and inexpensive, such ventilation involves significant heating and cooling to condition incoming fresh air. In very cold and hot climates these energy loads are even more pronounced and lessen the effectiveness of better insulated CPEs. Sensible heat exchangers have been proposed to reduce these heating and cooling loads, but such systems do not address other issues with open plant environments, including no water vapor recovery, limited CO_2 enrichment, and the risk of insects, spores, and other contaminants being introduced into the CPE.

Table S4.1. Pros and cons of different humidity control and water recovery methods for controlled plant environments

	Ventilation	Ventilation with Heat Exchanger	Dew-Point Condensation	Liquid or Solid Desiccant	Fertilizer Liquid Desiccant
Water	Water vapor is lost ★	Water vapor is lost ★	Water vapor is recovered as condensate but may need filtration ★★	Water vapor is recovered but must be carefully separated from desiccant ★★	Water is recovered by fertilizer and ready for delivery ★★★
Energy	Heating and cooling to condition fresh air ★	Minimal heating and cooling to condition fresh air ★★★	Mechanical work is needed to bring air to dew point ★	Thermal energy is needed to regenerate desiccant ★	Minimal work is needed to circulate fertilizer desiccant ★★★
Temperature	Introduces fresh air at outside temperature ★	Most sensible energy is recovered between fresh and exhaust air ★★★	Requires lowering air temperature to dew-point ★	Water vapor phase change releases minimal heat to air ★★★	Water vapor phase change releases minimal heat to air ★★★
CO_2	Effectiveness of CO_2 enrichment is limited ★	Effectiveness of CO_2 enrichment is limited ★	CO_2 enrichment is supported ★★★	CO_2 enrichment is supported ★★★	CO_2 enrichment is supported ★★★
Other	Insects, spores and contaminants may be introduced ★	Insects, spores and contaminants may be introduced ★	No insects, spores, and other contaminants are introduced ★★★	No insects, spores, and other contaminants are introduced ★★★	No insects, spores, and other contaminants are introduced ★★★

For closed-CPEs, several alternative humidity control and water recovery systems have been considered. Conventional dew-point condensers which are commonly used in buildings can be applied to plant environments, but these are energy intensive, requiring significant work to cool air to its dewpoint. This inability to regulate humidity without changing temperature, means that additional energy to reheat the air is often required. In addition, condensation on the cooling coils may favor bacteria and mold growth, compromising the quality of the air that is conditioned and the water that is recovered.

More recently, desiccant dehumidification has been proposed for closed-CPEs. These have shown excellent performance for high precision humidity control. Mostly toxic liquid desiccant solutions have been used such as lithium chloride and magnesium chloride. These solutions need to be regenerated requiring significant energy although can be from

heat source and waste heat energy. Water recovered must be separated from desiccant and care must be taken not to release desiccant into the water or air of the CPE.

4.8.2 Supplementary Note 4.2: Solubility of Desiccants

Table S4.2. Solubility of desiccants at atmospheric pressure and room temperature (101.3 kPa and 20 °C)

Fertilizer	Mass ratio (g/g_{water})	Mass fraction ($g/g_{solution}$)
$MgCl_2$	0.55	0.35
NH_4Cl	0.37	0.27
$(NH_4)_2HPO_4$	0.69	0.41
$(NH_4)_2SO_4$	0.75	0.43
NH_4NO_3	1.92	0.66
$Ca(NO_3)_2$	1.29	0.56
$NaNO_3$	0.88	0.47
KCl	0.34	0.25

4.8.3 Supplementary Note 4.3: Numerical Modelling Methods

All experimental observations were compared against numerical simulation of a finite element transport model. The model solves the heat and mass balance of each control volume applied to the discretized membrane surface, to obtain a solution in both the axial and normal directions to the membrane surface. The system of equations is described by equations (4.1) – (4.15), and the corresponding numerical logic and sequence of operations is illustrated in Figure S4.1. The model was implemented in Matlab (R2018a, Mathwords, Natick, MA).

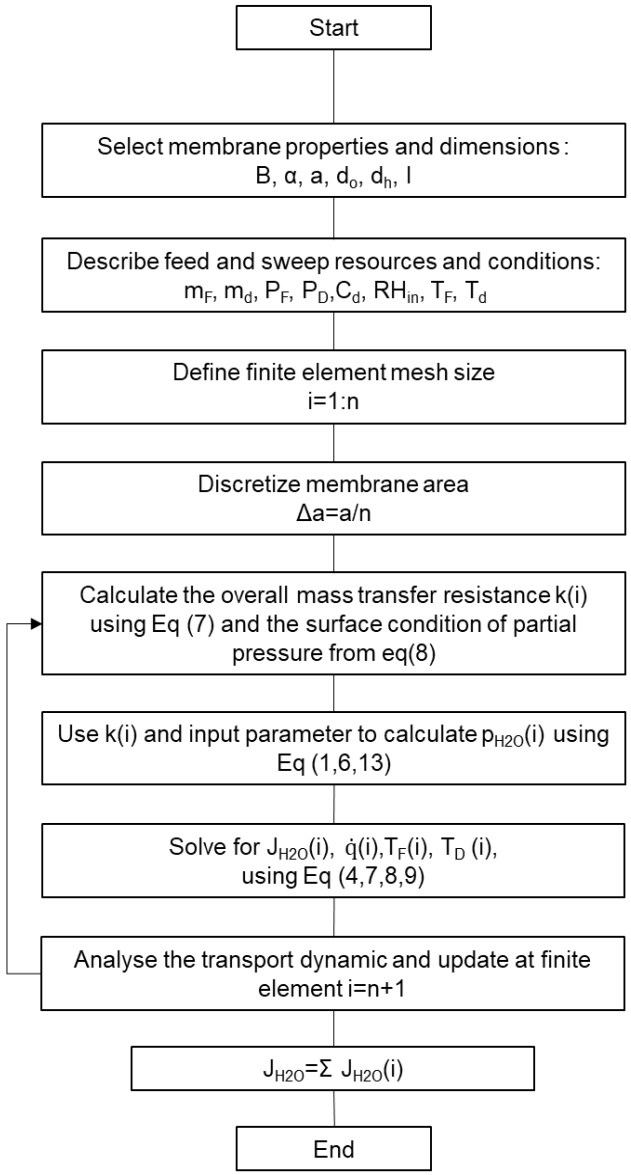

Figure S4.1. Finite element model used to numerically solve heat and mass transfer across each finite membrane element and determine the resulting energy and mass balance of each control volume throughout the liquid desiccant and air feed boundary layers. The model was implemented in Matlab (R2018a, Mathwords, Natick, MA) and used to simulate the dehumidification process.

4.8.4 Supplementary Note 4.4: Sample Test Data, Analytical Methods, and Uncertainty Analysis

Dehumidification was experimentally demonstrated, and the proposed transport model was validated using a series of tests performed on the Oakland University laboratory bench. Figure S4.2 shows raw data collected for a sample test trial, and Table S4.3 provides a detailed outline of how data is analyzed, including how experimental uncertainty is propagated throughout the analysis. Dehumidification rates were evaluated by considering a mass balance of the air feed.

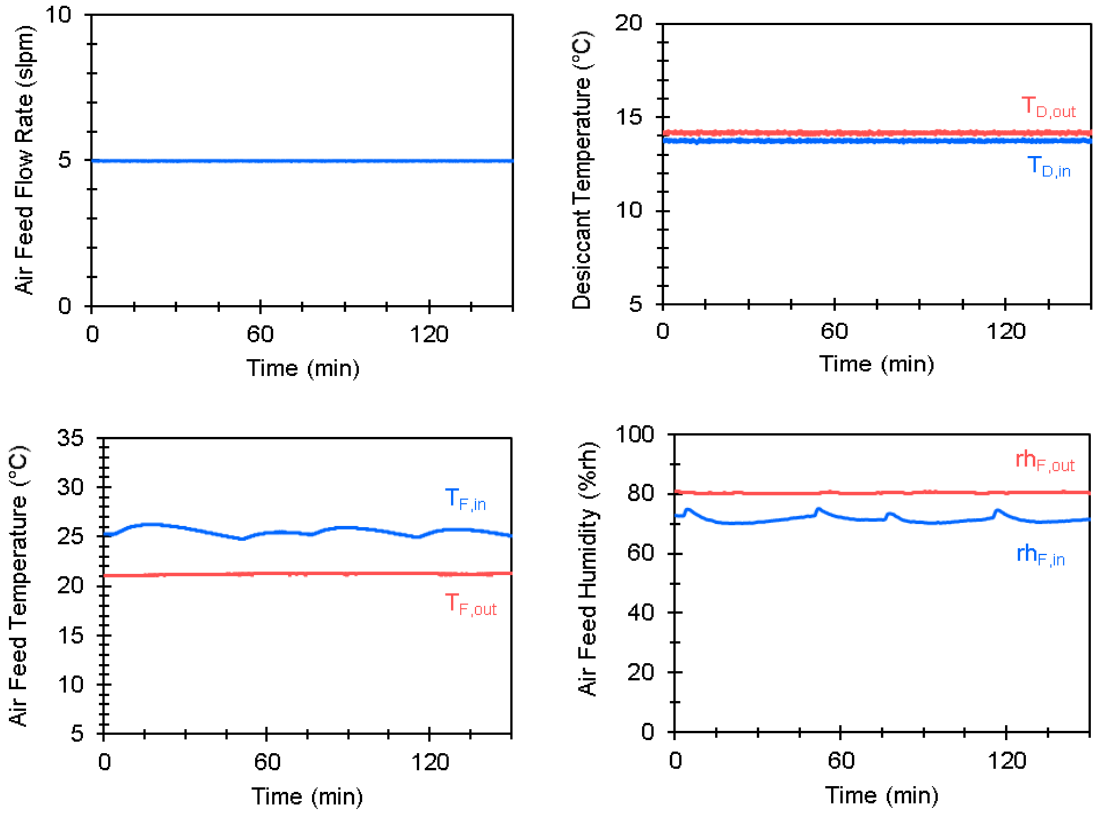

Figure S4.2. Raw test data.

Table S4.3. Raw test data and analysis.

Parameter	Value	Measurement or Analysis
Test preparation		
Liquid desiccant water mass $m_{D,w}$	980.4 ± 0.1 g	Balance (AX8201, Ohaus, Parsippany, NJ), 8000 ± 0.1 g
Liquid desiccant salt mass $m_{D,s}$	951.2 ± 0.1 g	Balance (AX8201, Ohaus, Parsippany, NJ), 8000 ± 0.1 g
Liquid desiccant concentration c_D	0.97 ± 0.00014 g/g	$c_D = \frac{m_{D,s}}{m_{D,w}}$ $\frac{\delta c_D}{c_D} = \sqrt{\left(\frac{\delta m_{D,s}}{m_{D,s}}\right)^2 + \left(\frac{\delta m_{D,w}}{m_{D,w}}\right)^2}$
Average trial results		
Air feed flow rate $\dot{V}_F$	4.99 ± 0.05 slpm	Mass flow controller (GH-32907-69, Masterflex, Radnor, PA), 5 slpm ± (0.8 % reading + 0.2 % full scale)
Air feed temperature at inlet $T_{F,in}$	25.5 ± 1 °C	Thermistor temperature sensor (AM2315, Aosong, Guangzhou, China), 125 ± 1 °C
Air feed temperature at outlet $T_{F,out}$	21.1 ± 1 °C	Thermistor temperature sensor (AM2315, Aosong, Guangzhou, China), 125 ± 1 °C
Air feed humidity at inlet $rh_{F,in}$	72.8 ± 2 %rh	Capacitive humidity sensor (AM2315, Aosong, Guangzhou, China), 100 ± 2 %rh
Air feed humidity at outlet $rh_{F,out}$	80.3 ± 2 %rh	Capacitive humidity sensor (AM2315, Aosong, Guangzhou, China), 100 ± 2 %rh
Air feed pressure p_F	17.66 ± 0.38 psia	Pressure transducer (GC557F0142CD, Ashcroft, Stratford, CT), 75 ± 0.38 psi
Liquid desiccant flow rate $\dot{V}_D$	2.08 ± 0.19 slpm	Flowmeter (8051K107, McMaster-Carr, Elmhurst, IL), 1.6 ± 0.05 gpm

Table S4.3 - Continued

Parameter	Value	Measurement or Analysis
Liquid desiccant temperature at inlet $T_{D,in}$	13.7 ± 0.3 °C	Thermal resistance sensor, (800-32/140-1188, Noshok, Berea, OH), 60 ± 0.3 °C
Liquid desiccant temperature at outlet $T_{D,out}$	14.2 ± 0.3 °C	Thermal resistance sensor, (800-32/140-1188, Noshok, Berea, OH), 60 ± 0.3 °C
Liquid desiccant pressure p_D	19.30 ± 0.38 psia	Pressure transducer (GC557F0142CD, Ashcroft, Stratford, CT), 75 ± 0.38 psid
Mass balance analysis		
Water vapor content of air feed at inlet $x_{H2O,in}$	0.0184 mol_{H2O}/mol ± 3.56 %	$x_{H2O,in} = rh_{in}\ \frac{p_{sat,in}}{p_F}$ where $p_{sat,in} = 10^{A-\left(\frac{B}{C+T_{F,in}}\right)}$ $\frac{\delta x_{H2O,in}}{x_{H2O,in}} = \sqrt{\left(\frac{\delta rh_{in}}{rh_{in}}\right)^2 + \left(\frac{\delta p_F}{p_F}\right)^2 + \left(B \ln(10) \frac{\delta T_{F,in}}{(C+T_{F,in})^2}\right)^2}$
Water vapor mass flow of air feed at inlet $\dot{m}_{F,H2O,in}$	4.39 g/h ± 3.76 %	$\dot{m}_{F,H2O,in} = \dot{m}_F \left(\frac{x_{H2O,in}}{1-x_{H2O,in}}\right) \frac{M_{H2O}}{M_{air}}$, $\frac{\delta \dot{m}_{F,H2O,in}}{\dot{m}_{F,H2O,in}} = \sqrt{\left(\frac{\delta \dot{m}_F}{\dot{m}_F}\right)^2 + \left(\frac{\delta x_{H2O,in}}{x_{H2O,in}(1-x_{H2O,in})}\right)^2}$

Table S4.3 – Continued

Parameter	Value	Measurement or Analysis
Water vapor content of air feed at outlet $x_{H2O,out}$	0.0159 mol_{H2O}/mol ± 3.33 %	$x_{H2O,out} = rh_{out} \frac{p_{sat,out}}{p_F}$ where $p_{sat,out} = 10^{A-\left(\frac{B}{C+T_{F,out}}\right)}$ $\frac{\delta x_{H2O,out}}{x_{H2O,out}} = \sqrt{\left(\frac{\delta rh_{out}}{rh_{out}}\right)^2 + \left(\frac{\delta p_F}{p_F}\right)^2 + \left(B \ln(10) \frac{\delta T_{F,out}}{(C+T_{F,out})^2}\right)^2}$
Water vapor mass flow of air feed at inlet $\dot{m}_{F,H2O,out}$	3.79 g/h ± 3.53 %	$\dot{m}_{F,H2O,out} = \dot{m}_F \left(\frac{x_{H2O,out}}{1-x_{H2O,out}}\right) \frac{M_{H2O}}{M_{air}}$ $\frac{\delta \dot{m}_{F,H2O,out}}{\dot{m}_{F,H2O,out}} = \sqrt{\left(\frac{\delta \dot{m}_F}{\dot{m}_F}\right)^2 + \left(\frac{\delta x_{H2O,out}}{x_{H2O,out}(1-x_{H2O,out})}\right)^2}$
Water vapor flux J	0.594 $g/m^2/h$ ± 5.16 %	$J = \frac{\dot{m}_{F,H2O,in} - \dot{m}_{F,H2O,out}}{a}$ $\frac{\delta J}{J} = \sqrt{\left(\frac{\delta \dot{m}_{F,H2O,in}}{\dot{m}_{F,H2O,in}}\right)^2 + \left(\frac{\delta \dot{m}_{F,H2O,out}}{\dot{m}_{F,H2O,out}}\right)^2}$

Table S4.4. Experimental raw test data

Fertilizer	salt mass $m_{D,s}$	water mass $m_{D,w}$	desiccant concentration c_D	Liquid desiccant pressure p_D	Liquid desiccant flow rate V_D	Inlet Liquid desiccant temperature $T_{D,in}$	Outlet Liquid desiccant temperature $T_{D,out}$	Air feed pressure p_F	Air feed flow rate V_F	Inlet Air feed temperature $T_{F,in}$	Inlet Air feed humidity $rh_{F,in}$	Outlet Air feed temperature $T_{F,out}$	Outlet Air feed humidity $rh_{F,out}$
	g	g	g/l	psi	Slpm	°C	°C	psi	Slpm	°C	% rh	°C	% rh
$Ca(NO_3)_2$	959.9	963.1	1.0	19.6	2.3	18.6	18.9	18.7	5.0	25.3	70.9	20.9	89.8
$Ca(NO_3)_2$	959.9	963.1	1.0	19.3	2.1	13.7	14.2	17.7	5.0	25.5	71.5	21.3	80.3
$Ca(NO_3)_2$	959.9	963.1	1.0	19.5	2.3	8.9	9.3	18.9	5.0	25.0	71.6	20.6	62.9
$Ca(NO_3)_2$	959.9	963.1	1.0	19.5	2.3	2.3	2.9	19.0	5.0	25.3	70.5	20.6	54.5
$Ca(NO_3)_2$	949.1	982.3	1.0	19.8	2.3	13.8	14.2	18.9	5.0	21.4	70.1	20.6	62.9
$Ca(NO_3)_2$	949.1	982.3	1.0	19.4	2.3	13.8	14.2	18.9	5.0	29.8	73.0	20.6	62.9
$Ca(NO_3)_2$	629.3	991.7	0.6	19.5	2.3	13.8	9.3	18.9	5.0	25.2	70.6	20.6	62.9
$Ca(NO_3)_2$	1252.9	983.1	1.3	20.8	2.3	13.8	9.3	18.9	5.0	24.9	70.7	20.9	72.0
$Ca(NO_3)_2$	952.7	970.9	1.0	19.4	2.3	13.8	14.3	18.7	5.0	25.3	81.2	20.9	89.8
$Ca(NO_3)_2$	949.1	982.3	1.0	20.0	2.3	13.8	14.4	19.5	5.0	26.0	91.2	20.9	89.8
NH_4Cl	278.8	976.2	0.3	19.1	2.3	13.9	14.3	14.9	5.0	25.1	71.0	21.4	74.0
$N_2H_8SO_4$	562.9	978.2	0.6	23.5	2.3	13.8	14.3	18.9	5.0	24.9	70.7	21.6	71.0

4.8.6 Supplementary Note 4.6: MATLAB code

```
%Sarah Moussaddy
% FEM for membrane dehumidification for a dessicant dehumidification

clear
clc

% constants
M_H2O=18; % (g/mol) molar mass of water
M_N2=28; % (g/mol) molar mass of air
M_sol=25; %(g/mol) molar mass of solution
R=8.314; % (J/mol/K) gas constant
Rc=0.1889; %(kJ/kg/K) gas constant
patm=101325; % (Pa) ambient pressure
T0=273; % (K) referance temperature
A=2.414e-5; % (Pa.s)constant for kinematic viscosity
B=247.8; %(K)constant for kinematic viscosity
C=140; %(K)constant for kinematic viscosity
d_air=1.225;%(kg/m3) Desity of air At STP
d_solution=1280;%(kg/m3) Desity 1.4 l of solution At STP
(d_Ca(NO3)2=1280g/l)
d_water=998; %(g/l) or (kg/m3) density of water at STP
vm=18*10^-6; %(m3/mol)molar volume of water at 20degC
Vshell=96/1000; %(l) volume of the membrane unit shell
K_s=0.2; %(W/m/K) thermal conductivity of silicone
K_w=0.6; %(W/m/K) thermal conductivity of water
K_a=0.026; %(W/m/K) thermal conductivity of air
Pr_w=8.5; %Prandtl number for sea water at 16 degC
Pr_a=0.7; %Prandtl number for air at 25 degC
Mu_a=15.314*10^-6;% (m2/s) kinematic viscosity of air
Mu_w=1.2*10^-6;% (m2/s) kinematic viscosity of water
Cp_a=29.15; % (J/mol/K) heat capacity of air
Cp_w=3.600; %(J/g/K) heat capacity of salty water (desiccant)

% material properties for silicone hollow fiber membrane
k_H2O=(3.6*M_H2O*3.35*10^-12)/(55*10^-6)*0.9; % (g/s/m2/Pa)
permeability to water vapor (input is 36000 barrer)
j0=k_H2O*(7.501*10^-2)/3.35; % (m3/m2/s/Pa)permeability to water
vapor
%b=1/128; %1/selectivity of silisone membrane for N2
%k_N2=k_H2O*b; % (mol/s/m2/Pa) permeability to N2
a=1; % (m2) membrane surface area
n=1000000; % number of node for finite element for the surface
d0=0.0003; %(m) OD of the fiber
d=55e-6; %(m) thickness of fiber wall
di=d0-2*d; %(m) inside diameter of the fiber
Nf=12600; %number of hollow fiber
Dis=0.06; %(m) ID of the shell side
Dh=((Dis^2)-(Nf*d0^2))/(Nf*d0); %(m) Hydraulic diameter on the shell
side
As=((Dis^2)-(Nf*d0^2))*3.14/4; %(m2) free flow area in the shell
```

```
% for Relative humidity input or different temperatire is used to
calculate
% the molar fraction with certain humidity value
A1=8.07131;% Antoine eq cst for water
B1=1730.63;% Antoine eq cst for water
C1=233.426;% Antoine eq cst for water

% % % % % % % % % % % % % % % % %
%    Initial Input condition    %
% % % % % % % % % % % % % % % % %

% ----------feed-------------
Pf=patm+29000; % (Pa) 5 psig total pressure of the feed
Tf_0=273+25; % (K) feed temperature
mf_0=5*d_air/60; % (g/s) (0.01-0.1g/s) mass flow rate of air
RH=0.71; %relatuve humidity of the feed
% ----------draw-------------
Pd=patm+31000; % (Pa) 7 psig total pressure of the draw
Td_0=273+15; % (K) draw temperature 13.7
Vd_0=2.1/60; % (l/s) volume flow rate of the solution
md_0=Vd_0*d_solution; %(g/s)(10-100 g/s) mass flow rate of solution
%md_0=Vd_0*d_solution; % (g/s)(10-100 g/s) mass flow rate of
solution
ms=1290*0.99; %(g) mass of solute used in the solution
(m_Ca(NO3)2=1290; m_(NH4)2SO4=754; m_NH4Cl=372)
M_s=236.15; % (g/mol) molar mass of solutes used
(M_Ca(NO3)2=236.15g/mole; M_(NH4)2SO4=132; M_NH4Cl=53)
C_0=ms/M_s/1.2*1000; %(mol/m3) 100% full equ ratio concentration of
the solution with molar mass

%Initial condition values
% ----------feed-------------
Pfsat_H2O_0=(10^(A1-B1/(C1+(Tf_0-273))))*133.32; % (Pa) water vapor
saturation pressure in the feed
%pf_H2O_0=RH*Pfsat_H2O_0; % (Pa) partial pressure of the water vapor
with no applied pressure
pf_H2O_0=RH*Pfsat_H2O_0; % (Pa) partial pressure of the water vapor
xf_H2O_0=pf_H2O_0/Pf; % molar fraction in the feed

% ----------draw-------------
Pdsat_H2O_0=(10^(A1-B1/(C1+(Td_0-273))))*133.32; % (Pa) water vapor
saturation pressure in the draw
O_0=3*C_0*R*Td_0; %(Pa)Osmotic pressure of the solution with
concentration C
pd_H2O_0=Pdsat_H2O_0*exp(((Pd-patm)-O_0)*vm/R/Td_0); % (Pa) partial
pressure of the water vapor in function of temperature, pressure and
concentration
xd_H2O_0=pd_H2O_0/Pd; %initial draw H2O molar fraction
da=a/n; %area differential
Mu=15.314*10^-6;% (m2/s) kinematic viscosity
b=1/600; %selectivity of silisone membrane for O2
```

```
%diffusion D of water vapor in N2%
D0=2.19*10^-5; %(m2/s)
D=D0*(patm/Pf)*(Tf_0/T0)^1.81; % (m2/s) waer vapor diffusion in air
% Initial molar flow rates on the draw and feed side
nf_0=mf_0/M_N2; % (mol/s) feed molar flow rate
% nd_0=md_0*1000/M_sol; % (mol/s) draw molar flow rate
Vshell/Vd_0;
nf_H2O_0=xf_H2O_0*nf_0;
hv=(3151.9-2.384*Td_0); %(J/g) heat of vaporization of water at
17degC (average temperature between air and desiccant)
for i=1:n
% Initial condition for feed and draw
nf(1)=nf_0;
md(1)=md_0;
Cs(1)=C_0;
O(1)=O_0;
xf_H2O(1)=xf_H2O_0;
xd_H2O(1)=xd_H2O_0;
nf_H2O(1)=xf_H2O(1)*nf(1);
md_H2O(1)=((d_water/M_H2O)/((ms/M_s)+(d_water/M_H2O)))*md(1);
p_H2Of(1)=pf_H2O_0;
p_H2Od(1)=pd_H2O_0;
Td(1)=Td_0;
Tf(1)=Tf_0;
dm_H2O(1)=0;
Pdsat_H2O(1)=Pdsat_H2O_0;
Pdsat_H2O_m(1)=(10^(A1-B1/(C1+((Td(1)+Tf(1))/2-273))))*133.32; %
(Pa) water vapor saturation pressure in the draw
p_H2Od_m(1)=Pdsat_H2O_m(1)*exp(((Pd-patm)-O(1))*vm/R/Td(1)); % (Pa)
partial pressure of the water vapor in function of temperature,
pressure and concentration
Pfsat_H2O(1)=Pfsat_H2O_0;
Re_w=Vd_0/As*Dh/Mu_w/1000;%reynolds number in shell side
Re_a=4*mf_0/pi/di/Mu_a/d_air/1000;
hd=0.36*K_w*(Re_w^0.55)*(Pr_w^0.33)/Dh; % (W/k/m2) heat coefficient
for dessicant side (shell side)
hf=0.023*K_a*(Re_a^0.8)*(Pr_a^0.3)/(di*Nf); % (W/k/m2) heat
coefficient for air side (tube side)(Dittus Boelter equation for
smooth tube)
F=(1/patm)*(T0/Tf(1));
uf=Nf*Vd_0/1000/As; % (m/s)Velocity of the gaz flux in the shell
side
%k=1.62*di/d0*(di^2*uf^2/Dis/D)^0.33;
k=0.0732*((Dh*100)^0.6)*((D*10000)^0.67)*((uf*100)^0.6)/(((d0*100)^0
.4)*((Mu*10000)^0.27)); %(cm/s)
xs(1)=(xf_H2O(1)*(k*0.01*F+j0*(xd_H2O(1)*(b-1)-
b))+j0*xd_H2O(1))/((k*0.01*F+j0*(1-xf_H2O(1)*(1-b))));
xf_H2O_m(1)=xf_H2O(1);
dm_H2O(i)=0.15*k_H2O*(Pf*xs(i)-p_H2Od_m(i))*da;%(g/s) water vapor
permeate rate
% permeate and heat flux per element da
%syms Tdm Tfm q
```

```
%eqn1=Tdm(i)-Td(i)-q(i)/hd==0; %(K)dessicant temperature at the
membrane surface
%eqn2=Tfm(i)-Tf(i)+q(i)/hf==0; % (K) air temperature at the membrane
surface
%eqn3=q(i)-dm_H2O(i)*hv/da-K_s/d*(Tfm(i)-Tdm(i))==0; % (W/m2) heat
transfer across the membrane
%eqn4=Pdsat_H2O_m(i)-(10^(A1-B1/(C1+(s_Tdm(i)-273))))*133.32==0; %
(Pa) water vapor saturation pressure in the draw
%eqn5=p_H2Od_m(i)-Pdsat_H2O_m(i)*exp(((Pd-patm)-
O(i))*vm/R/Td(i))==0; % (Pa) partial pressure of the water vapor in
function of temperature, pressure and concentration
%eqn4=dm_H2O(i)-k_H2O*(p_H2Of(i)-p_H2Od(i))*da==0;%(g/s) water vapor
permeate rate
    A=[1 0 1/hf/da;0 -hd*da 1;-K_s*da/d K_s*da/d 1];
    V=[ Tf(i); dm_H2O(i)*hv-hd*da*Td(i); 0];

X= linsolve(A,V);
s_Tfm(i)=X(1);
s_Tdm(i)=X(2);
s_q(i)=X(3);

%Update the flux on the feed side
nf_H2O(i+1)=nf_H2O(i)-(dm_H2O(i)/M_H2O);%(mol/s) feed H2O molar flux
nf(i+1)=nf(i)-(dm_H2O(i)/M_H2O); % (mol/s)total feed molar flux
xf_H2O(i+1)=nf_H2O(i+1)/nf(i+1); %feed H2O molar fraction
p_H2Of(i+1)=xf_H2O(i+1).*Pf;
Tf(i+1)=Tf(i)-s_q(i)/nf(i+1)/Cp_a;
Pfsat_H2O(i+1)=(10^(A1-B1/(C1+(Tf(i+1)-273))))*133.32;
%Update the flux on the draw side
md_H2O(i+1)=md_H2O(i)+dm_H2O(i); %(g/s) draw h2o molar flux
md(i+1)=md(i)+dm_H2O(i); % (g/s)total draw molar flux
Cs(i+1)=Cs(i)/(1+(dm_H2O(i)/md_H2O(i))); %draw concentration
(mol/m3)
Td(i+1)=Td(i)+s_q(i)/md(i+1)/Cp_w;
O(i+1)=2*Cs(i+1)*R*Td(i+1); % (pa) osmotic pressure on the draw side
Pdsat_H2O(i+1)=(10^(A1-B1/(C1+(Td(i+1)-273))))*133.32; % (Pa) water
vapor saturation pressure in the draw
p_H2Od(i+1)=Pdsat_H2O(i+1)*exp(((Pd-patm)-O(i+1))*vm/R/Td(i+1)); %
(Pa) partial pressure of the water vapor in function of temperature,
pressure and concentration
xd_H2O(i+1)=p_H2Od(i+1)/Pd;
Pdsat_H2O_m(i+1)=(10^(A1-B1/(C1+(s_Tdm(i)-273))))*133.32; % (Pa)
water vapor saturation pressure in the draw
p_H2Od_m(i+1)=Pdsat_H2O_m(i+1)*exp(((Pd-patm)-O(i+1))*vm/R/Td(i+1));
% (Pa) partial pressure of the water vapor in function of
temperature, pressure and concentration
xs(i+1)=(xf_H2O(i+1)*(k*0.01*F+j0*(xd_H2O(i+1)*(b-1)-
b))+j0*xd_H2O(i+1))/((k*0.01*F+j0*(1-xf_H2O(i+1)*(1-b))));
%xd_H2O(i+1)=p_H2Od(i+1)/Pd;
end
```

CHAPTER FIVE

SPECIFIC ENERGY ANALYSIS OF FERTILIZER-BASED LIQUID DESICCANT DEHUMIDIFICATION FOR SUSTAINABLE INDOOR PLANT ENVIRIOMENT AGRICULTURE

5.1 Original publication

Chapter Five is based on a paper that is in progress for publication. This study utilizes theoretical modeling and a parametric analysis to examine the impact of key operating conditions, including desiccant temperature, air and desiccant flow rates, and fertilizer concentration, on the specific energy of the system[4].

5.2 Introduction

The introduction of controlled plant environments, such as greenhouses, can help to overcome the challenge of providing food on a larger scale in response to rising global demand [24,74]. However, in the controlled plant environments, the humidity tends to rise as a result of evapotranspiration, which is the combination of soil evaporation and plant transpiration [19]. One of the essential aspects of running such systems for the best plant growth is regulating greenhouse humidity controls, which can be challenging due to this rise in humidity [126,127]. This humidity control can be costly and energy intensive [128], and recent regulations in certain locations have been imposed to limit the energy consumption associated with the dehumidification of the indoor plant environment [32].

[4] S. Moussaddy, S. Aryal, J. Maisonneuve, "Specific Energy Analysis of Fertilizer Based Liquid Desiccant Dehumidification for Sustainable Indoor Plant Environment Agriculture. In Progress

Most conventional dehumidification systems use a condenser for direct water removal [26,129] or involve significant operational costs to heat or cool the indoor air. In order to ensure effective management and system operation, the system's energy consumption should be established and adjusted; it is typically defined as the specific energy of a dehumidification system. Several studies focused into ways to reduce the specific energy of dehumidification systems.

In a recent study on dehumidification in a vapor compression cycle, Tang et al. [33] found that system optimization allowed them to achieve an energy density of 0.36 kWh/kg for air at 80% relative humidity and 0.94 kWh/kg at 38% relative humidity for air temperature of 26 ^{o}C. Recently, a liquid desiccant system has been suggested for a more regulated dehumidification with a smaller energy footprint [130]. Various studies have demonstrated the system's potential for dehumidification processes, but they still require desiccant regeneration [107-110,131-133]. A study by Zhang et al. [34] for a dehumidification system utilizing a heat pump coupled with a membrane desiccant unit produced a power density range of 0.52 to 0.8 kWh/kg. Furthermore, Lefers et al. [80] reported an estimated energy density of 0.45 kWh/kg when using a desiccant system for greenhouse dehumidification.

In an earlier work [134], the fertilized based dehumidification across a membrane was proposed as solution to recover water from the indoor plant environment and to reduce the energy load by removing the regeneration step of the desiccant. In this system, a batch of fertilizer desiccant is recirculated through the membrane dehumidification system, recovering water vapor from the indoor plant environment, until the solution is sufficiently diluted for delivery to the plants. Water vapor can be drawn from a humid air stream across

a selective membrane by the vapor pressure gradient established between the humid air and the cooled concentrated fertilizer-based liquid desiccant solution as shown in Figure 5.1.

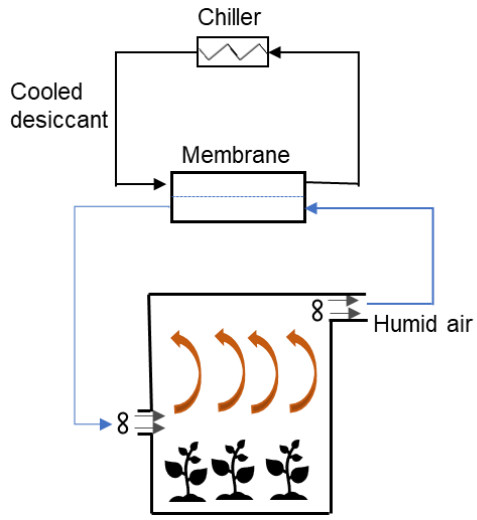

Figure 5.1. Water vapor permeate can be drawn from a humid air stream across a selective polymer membrane by a vapor pressure gradient established by a concentrated fertilizer-based liquid desiccant solution. This process can be used to dehumidify indoor plant environments and recycle water vapor for plant fertigation. A water-cooled chiller is used to maintain the fertilizer desiccant temperature.

As the fertilizer desiccant system is proposed as a solution to eliminate the energy required for regeneration, detailed energy analysis for the proposed system is needed to compare with state-of-the-art technologies. According to the previous study, desiccant temperature was major parameters affecting the system performance, where lower desiccant temperature achieved higher dehumidification rate. However, with lower temperature, higher energy rate for cooling is expected. Thus, the objective of this study is to perform an energy analysis to show the tradeoff between dehumidification and desiccant cooling energy consumption. For a given set of conditions, it is expected to have an optimal liquid desiccant temperature that can achieve the desired targeted humidity at a lower specific energy.

Therefore, in this study we perform a theoretical analysis, and build a numerical model for the energy analysis. The developed model takes into account the sensitivity of several key variables in order to plot the specific energy over a range of operational conditions. However, while we have already validated the concept using a PDMS dense membrane, the choice of the membrane is still one of the limiting factors in the system in terms of dehumidification capacity, thermal insulation properties, and their effect on energy consumption [106]. As a result, in this study, we also present the effect of the membrane property on the system's performance in terms of mass transfer and specific energy.

5.3 Theory

5.3.1 Vapor Transfer Across the Membrane

In a membrane-based dehumidification system, a polymer core separates concentrated desiccant solution from a humid air feed stream as shown in Figure 5.2. Water vapor from the air stream migrates to the membrane's surface, diffuses through it, and then desorbs and condenses on the liquid desiccant surface due to a differential vapor pressure between air stream and the liquid desiccant solution.

The water vapor flux associated with this process is defined as the water vapor mass transfer rate per unit membrane area. The water vapor mass transfer rate is proportional to the vapor pressure difference across the feed air and the liquid desiccant, and the mass transfer coefficient. The water vapor flux as a function of water vapor mass transfer rate is given by:

$$J = \frac{\Delta \dot{m}}{a} = K \, \Delta p_{H2O} \tag{5.1}$$

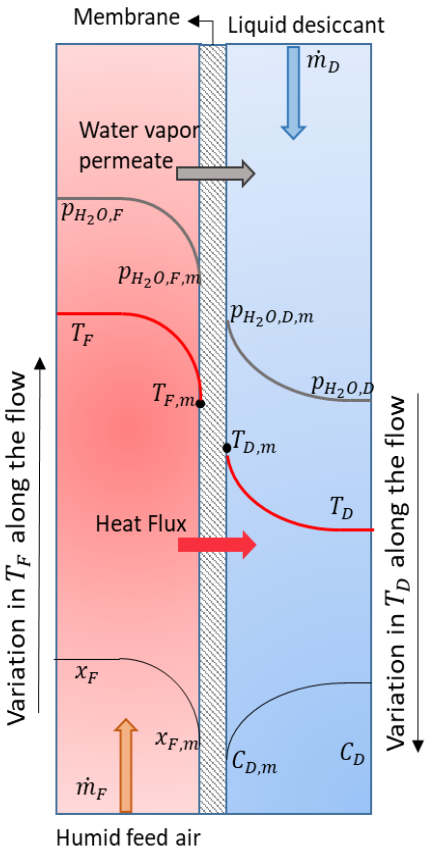

Figure 5.2. The water vapor pressure gradient difference between the liquid desiccant and the humid feed air drives the vapor flux in a membrane-based liquid desiccant dehumidification process. The vapor pressure difference is across the membrane will be determined by the non-linear temperature and concentration gradient.

Where J is the water vapor flux, $\Delta\dot{m}$ is the water vapor mass transfer rate, a is the membrane area, K is the mass transfer coefficient, and Δp_{H2O} is the vapor pressure difference across the two fluids. The resulting vapor pressure difference is calculated using the feed air and liquid desiccant vapor pressure as shown by:

$$\Delta p_{H_2O} = p_{H_2O,F} - p_{H_2O,D} \tag{5.2}$$

Where $p_{H_2O,F}$ and $p_{H_2O,D}$ denotes the vapor pressure at feed air and liquid desiccant side, respectively. The partial pressure of water vapor in air in equation (5.2) is calculated using the air relative humidity or the mole fraction of water vapor in air as shown by:

$$p_{H_2O,F} = x_F p_F = rh_F p_o \quad (5.3)$$

Where x_F is the mole fraction of water vapor in air, rh_F is the relative humidity of feed air, p_F is the hydraulic pressure of feed air and p_o is the saturation pressure. The vapor pressure of a liquid desiccant in equation (5.2) can be described by the Kohler equation, which describes the vapor pressure of a solution as a function of solution temperature, hydraulic pressure, and osmotic pressure [105, 106]. The Kohler equation is shown by:

$$p_{H_2O,D} = p_o \exp\left[\frac{V_m}{RT}(p - \pi)\right] \quad (5.4)$$

Where p_o is the equilibrium vapor pressure of pure water, p is the hydraulic pressure, R is the gas constant, V_m is the molar volume of water, T is the solution temperature and π is the osmotic pressure. In equation (5.4), the osmotic pressure of the desiccant solution can be calculated using the Van't Hoff equation and the equilibrium vapor pressure of pure water can be calculated using the Antoine equation as shown by:

$$\pi = iRTc \quad (5.5)$$

$$p_o = 10^{\left(A_o - \frac{B_o}{C_o + T}\right)} \quad (5.6)$$

Where i and c represents number of ions in the desiccant solution and desiccant concentration, respectively in equation (5.5). In the Antoine equation,A_o, B_o and C_o are the empirical constants. It is evident that equations (5.2-6) forms a basis for calculation of water vapor flux in equation (5.1).

Figure 5.3 shows the effect on water vapor flux with the variation of liquid desiccant temperatures for a typical fertilizer solution for a base case scenario ($T_F = 25$ ℃ and $rh = 70\%$). The figure shows that dehumidification rates are sensitive to the liquid desiccant temperatures. The larger vapor flux can be attained at lower desiccant temperatures as the

solution's equilibrium vapor pressure is significantly reduced at lower temperatures, and in addition, the outlet air feed humidity decreases. The sensitivity graph emphasizes the fact that the liquid desiccant temperature can be controlled to achieve the desired rate of dehumidification. The figure illustrates the relationship between lower dehumidification for higher desiccant temperatures and higher dehumidification for lower desiccant temperatures.

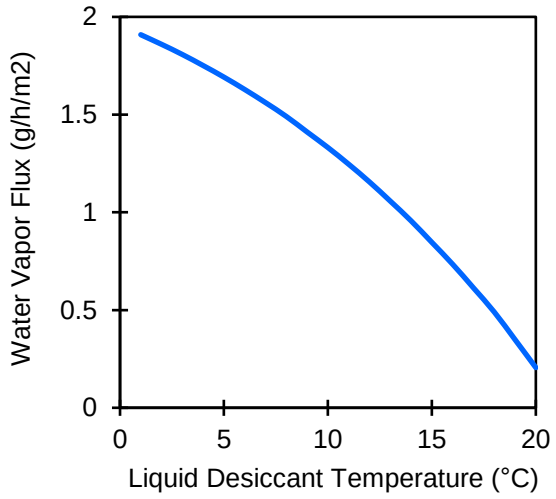

Figure 5.3. Effect of liquid desiccant temperature on water vapor flux for a liquid desiccant solution with $Ca(NO_3)_2$ fertilizer at concentration of 968 g/l, and given feed air with temperature of 25 ºC and 70% relative humidity.

5.3.2 Heat Transfer Across the Membrane

Due to the strong dependence of liquid desiccant vapor pressure on solution temperature, heat transfer dynamics have a significant impact on water vapor transport in a liquid desiccant system as explained by equation (5.4) and (5.6). In order to transfer the water vapor from feed air to the liquid desiccant, temperature gradients between warm air and cool desiccant solution must be maintained. As a result, the driving vapor pressure gradient between the feed air and the liquid desiccant develops, boosting the

dehumidification rate. Thus, careful consideration on heat transfer from air side to the liquid desiccant side have to be made to precisely define the dehumidification rate.

During the flow of the feed air and liquid desiccant, the temperature gradient exists in both the axial and normal direction. The bulk air, membrane surface on bulk air side, bulk liquid desiccant, and membrane surface on bulk liquid desiccant are at different temperatures as shown in Figure 5.3. It is to note that the air temperature decreases along the flow and causes the membrane surface temperature on its side to decrease. However opposite process happens in the liquid desiccant side.

As previously mentioned, it is critical to maintain the thermal gradient between the warm air and the liquid desiccant in order to achieve higher dehumidification rates. Thus, the additional energy required to keep the desiccant at the desired temperature is proportional to the temperature change caused by diffusion heat and the water vapor permeate condensation heat in the desiccant solution. We now define cooling load for the system as being solely related to the cooling energy added to the desiccant liquid solution, and we describe it as follows:

$$\dot{Q}_{cooling} = \dot{m}_D c_D \left(T_{D,out} - T_{D,in}\right) \tag{5.7}$$

Where $\dot{m}_D$ is the mass flow rate of the desiccant, c_D specific heat capacity of desiccant, $T_{D,in}$ is the inlet temperature of the desiccant, and $T_{D,out}$ is the outlet temperature of the desiccant.

The cooling load in these kinds of systems is the result of heat transfer via three mechanisms: thermal diffusion through the through the air and liquid boundary layers and membrane, mass transport of vapor through membrane, and heat of condensation produced through permeate phase shift in the liquid desiccant in these kinds of systems.

$$\dot{q}_{diffusion} = \frac{\Delta T}{r} \tag{5.8}$$

$$\dot{q}_{sensible} = Jc_pT \tag{5.9}$$

$$\dot{q}_{latent} = JH_c \tag{5.10}$$

Where c_p is the specific capacity of the vapor, H_c is the heat of condensation, r is the thermal resistivity across the finite temperature difference ΔT. The thermal resistance over the membrane is given by $r = \frac{L}{k}$. Here, L is the thickness of the membrane and k is the thermal conductivity associated with it. Similarly, there exists thermal resistance in the feed air and liquid desiccant which is $r = \frac{1}{h}$ where h is the heat transfer coefficient associated with feed air h_F and liquid desiccant h_D.

In the previous discussion, we mentioned that water vapor condensation has an impact on the cooling load needed to keep the desiccant at the desired temperature. It is also clear from equation (5.7) that the inlet desiccant temperature has an impact on the cooling load. Figure 5.4 shows the effect on cooling energy added to the liquid desiccant with the variation of liquid desiccant temperatures for a typical fertilizer solution for a base case scenario ($T_F = 25\,℃$ and $rh = 70\%$). It has been found that when the liquid desiccant temperature rises, less energy is required for cooling as a result of decreased latent heat and diffusive heat transfer. There is resistance to latent heat transfer at higher liquid desiccant temperatures due to the mass transfer of water vapor from the air side to the liquid side being constrained. Convective heat transfer is also reduced due to the smaller temperature difference from the air feed side to the liquid side at higher liquid desiccant temperatures. The evidence for decreased latent heat transfer at higher temperatures can be seen in Figure 5.3, which shows decreased vapor flux at higher desiccant temperatures.

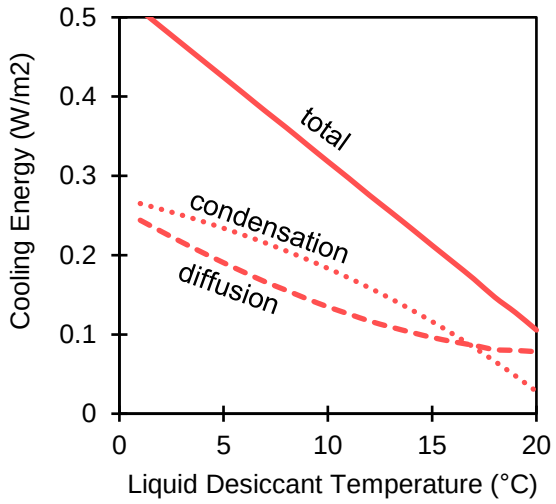

Figure 5.4. Effect of liquid desiccant temperature on cooling energy. Total cooling energy consumed by the system (solid line) in function of the desiccant temperature and the different rate of energy from diffusion (dashed line) and from permeate transfer (dotted line) related to the latent heat gain. Given liquid desiccant solution with $Ca(NO_3)_2$ fertilizer at concentration of 968 g/l, and given air feed with temperature of 25 °C and 70 % relative humidity.

5.3.3 Heat and Mass Transfer through Thermal and Concentration Boundary Layers

The preceding section provides a generalized overview of heat and water vapor transport in liquid dehumidification. The detailed analysis considering the membrane surfaces and boundary layers is presented in this section. The schematic of the process involving feed air boundary layer (δ_F), desiccant boundary layer (δ_D), membrane surfaces and concentration is shown in Figure 5.2. In the previous section, heat and mass transport was explained without going into detail using the membrane surface conditions. However, in reality, the membrane surface conditions are critical for accurately setting up the governing equations because both vapor transfer and heat transfer between the two fluids are affected by concentration and temperature at the membrane surfaces.

From equations (5.1) and (5.2), it is known that vapor flux is dependent on the mass transfer coefficient and the vapor pressure difference across the two fluids. However, in

practice, the vapor pressure difference across the membrane is less than the vapor pressure difference between the bulk fluids, owing to the non-linear trend of vapor pressure gradient across the boundary layers at both surfaces caused by temperature and concentration polarization as depicted in Figure 5.2. The resulting vapor difference across the membrane is calculated using the feed air vapor pressure ($p_{H_2O,F,m}$) and liquid desiccant vapor pressure ($p_{H_2O,D,m}$) at the membrane surfaces. As permeate diffuses within the bulk fluids, boundary layers will form on both the feed air and liquid desiccant sides of the membrane. These boundary layers add additional resistance to fluid-to-fluid vapor transport and must be factored into the overall mass transfer coefficient as shown by:

$$\frac{1}{K} = \frac{1}{K_F} + \frac{1}{K_m} + \frac{1}{K_D} \tag{5.11}$$

Where K_m is the mass transfer coefficient in the membrane which is the ratio of membrane permeability (B), and membrane thickness (L). The mass transfer coefficient across the feed boundary layer is given by the correlation used for gas flows in a hollow fiber membrane given by [46, 69, 114]:

$$K_F = 0.0732 \frac{P}{P'} \frac{T'}{T} \frac{D}{d^{0.4}} Re^{0.6} Sc^{0.33} \tag{5.12}$$

Where D is the water vapor diffusivity in air is, Re is the Reynolds number, Sc is the Schmidt number,d is the fiber outer diameter, and P' and T' are standard pressure and temperature. In the equation (5.11), mass transfer coefficient through the liquid desiccant boundary, K_D is neglected since the water concentration of liquid desiccant will change only slightly [53].

Since, the temperature at either side of the membrane surface affects the surface vapor pressure at its location, heat transfer analysis should be done taking this factor into account. The detailed heat transfer in the liquid desiccant dehumidification process can be described by the following governing equations:

$$\dot{m}_F \, c_{p,F} \left(T_{F,in} - T_{F,out}\right) - h_F dA \left(T_F - T_{F,m}\right) - JdA \, c_p \, T_F = 0 \qquad (5.13)$$

Where $\dot{m}_F$ is the mass flow rate of the feed air, $T_{F,in} - T_{F,out}$ is the temperature difference between feed air at inlet and outlet, h_F is the heat transfer coefficient of feed air, c_p is the specific heat capacity, and $T_F - T_{F,m}$ is the temperature difference between feed air at bulk and the membrane surface on feed side. equation (5.13) denotes the sensible heat transfer in the feed air side.

Where $\dot{m}_F$ is the mass flow rate of the feed air, $T_{F,in} - T_{F,out}$ is the temperature difference between feed air at inlet and outlet, h_F is the heat transfer coefficient of feed air, c_p is the specific heat capacity, and $T_F - T_{F,m}$ is the temperature difference between feed air at bulk and the membrane surface on feed side. equation (5.13) denotes the sensible heat transfer in the feed air side.

$$\dot{m}_D \, c_{p,D} \left(T_{D,in} - T_{D,out}\right) + h_D dA \left(T_{D,m} - T_D\right) + JdA \, c_p \, T_{D,m} + JdA \, H_c = 0 \qquad (5.14)$$

Where $\dot{m}_D$ is the mass flow rate of the liquid desiccant, $T_{D,in} - T_{D,out}$ is the temperature difference between liquid desiccant at inlet and outlet, h_D is the heat transfer coefficient of liquid desiccant, c_p is the specific heat capacity, and $T_{D,m} - T_D$ is the temperature difference between liquid desiccant at membrane surface and the bulk side. Equation (5.14) denotes the sensible heat transfer and latent heat transfer in the liquid desiccant side. In the

above equation heat due to dilution is neglected. The heat transfer through the membrane surfaces is represented by the equation given by:

$$h_F \left(T_F - T_{F,m}\right) + J\, c_p\, T_F = \frac{k}{L}\Delta T + J\, c_p\, T_{F,m} \tag{5.15}$$

$$\frac{k}{L}\Delta T + J\, c_p\, T_{F,m} + J\, H_C = h_D \left(T_{D,m} - T_D\right) + J\, c_p T_{D,m} \tag{5.16}$$

Equations (5.15) and (5.16) illustrate how the membrane-based liquid-desiccant dehumidification system combines conductive, convective, and latent heat transfer. Equations (5.13–16) display the sets of equations from the energy balance for the liquid–desiccant dehumidification system in both axial and normal orientations. All the governing equations for the heat transfer rate in air side and liquid desiccant side with the equivalent thermal circuit along with the mass transfer dynamics have been discussed and validated in the earlier study [134]. The way to derive heat and mass transfer governing equations constituting water is also clearly explained by Jeong et al. [135].

5.3.4 Specific Energy of Dehumidification

In our previous study and discussion, we demonstrated that higher flux can be achieved by operating at lower liquid desiccant temperatures, though this increases energy consumption and thus operational costs. As a result, we are investigating the energy usage required for the dehumidification rates.

The energy consumption for the dehumidification purpose is defined by the following equation:

$$E = \frac{\dot{Q}_{cooling}}{COP} = \frac{\dot{m}_D c_D \left(T_{D,out} - T_{D,in}\right)}{COP} \tag{5.17}$$

Where COP is the coefficient of performance of the system cooling the desiccant. As the $\mathrm{COP} > 1$, the energy usage is always less than cooling load which is described in the section 5.2.2. To correlate energy consumption with water vapor flux, equation (5.17) can be modified to define a parameter called specific energy of dehumidification, which is represented as:

$$e = \frac{\mathrm{E}}{\mathrm{J}} \tag{5.18}$$

Greater specific energy values are undesirable because they indicate that there will be a significant cooling energy addition to the desiccant. To maintain desiccant at lower temperatures, the energy consumed is high, however, higher dehumidification rates are be achieved. In contrast to this, at higher temperatures, the energy required to cool the desiccant is low, however the dehumidification performance deteriorates. As a result, determining the liquid desiccant temperature that yields the lowest specific energy of dehumidification while maintaining the system's required rate of dehumidification is critical. Therefore, optimizing the process from the dehumidification side while limiting the system's energy utilization is of interest.

Figure 5.5 shows the general overview of the effect of liquid desiccant temperature on the specific energy for a typical fertilizer solution for a base case scenario ($T_F = 25$ ℃ and $rh = 70\%$). As mentioned earlier, specific energy is a parameter dependent on the vapor permeate flux and the cooling energy, careful considerations have to be made to minimize it. Higher vapor flux is achieved at lower desiccant temperatures, however, the energy required to cool the desiccant increases. Higher desiccant temperatures result in a fall in vapor flux and a reduction in the overall cooling needed. In both the cases, the specific

energy is on the higher side. For a given set of conditions there will be some unique liquid desiccant temperature that can achieve the minimum specific energy. There is always a tradeoff between maintaining high dehumidification rates and low specific energy at different temperatures. We can see that for the specific conditions used in this case, we are able to obtain a minimum specific energy as low as 0.238 kWh/kg. Even though operating at lower desiccant temperatures and higher concentration can achieve much higher dehumidification rates, however, a compromise should be made as the minimum specific energy does not coincide with the maximum value of flux.

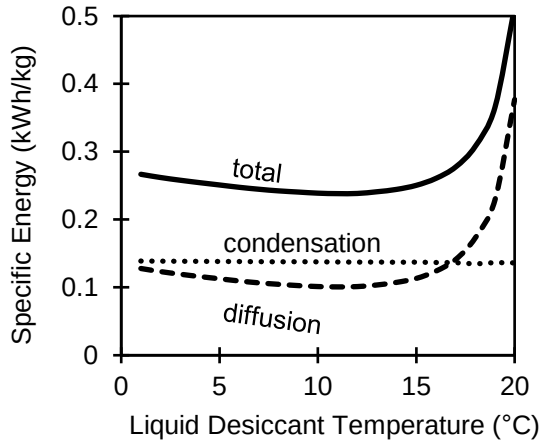

Figure 5.5. Effect of liquid desiccant temperature on specific energy. Total specific energy of the system (solid line) is function of the desiccant temperature and the different rate of energy from diffusion (dashed line) and from permeate vaporization heat transfer (dotted line). The latent energy can be considered as the minimum thermodynamic limit of the specific energy of dehumidification. Given liquid desiccant solution with $Ca(NO_3)_2$ fertilizer at concentration of 968 g/l, and given air feed with temperature of 25 °C and 70 % relative humidity.

5.4 Materials and Methods

To investigate the effects of several controlled parameters on the performance of fertilizer-based dehumidification, the various scenarios are thoroughly simulated and numerically analyzed using the forward finite difference method in MATLAB. The control volume consisting of feed air, membrane and liquid desiccant is discretized into 'n' number

of cells, each having equal area. The heat and mass transfer model is implemented in each cell by primarily using the governing equations using a numerical approach to solve for the gas transmembrane flux and temperature variation. The implemented model employs a 2-D finite element approach in which the normal and axial variations of concentration and temperature profiles in the boundary layer of a membrane hollow fiber are modeled using the angular symmetry assumption. The solution for the temperature, concentration, and resulting vapor pressure gradients in both the axial and normal directions to the membrane surface is obtained by solving the mass and energy balance between the fluids across the membrane to each element using the equations (5.1 - 16), and the corresponding numerical logic and sequence of operations are shown in Figure 5.6.

Numerical analysis and simulations are performed for different set of operation condition and membrane characteristic to compare the energy density and performance of the fertilizer-based dehumidification system. A hollow fiber module with dense PDMS membrane was used in the simulated model. A summary of the membrane characteristics and simulation input parameters is provided in Table 5.1.

The model was implemented in Matlab (R2018a, Mathwords, Natick, MA) and used to simulate the dehumidification process.

Default conditions for the simulation were based on operating conditions from the validated model with experimental trials as shown in Figure 5.7 and discussed in our previous work [134].

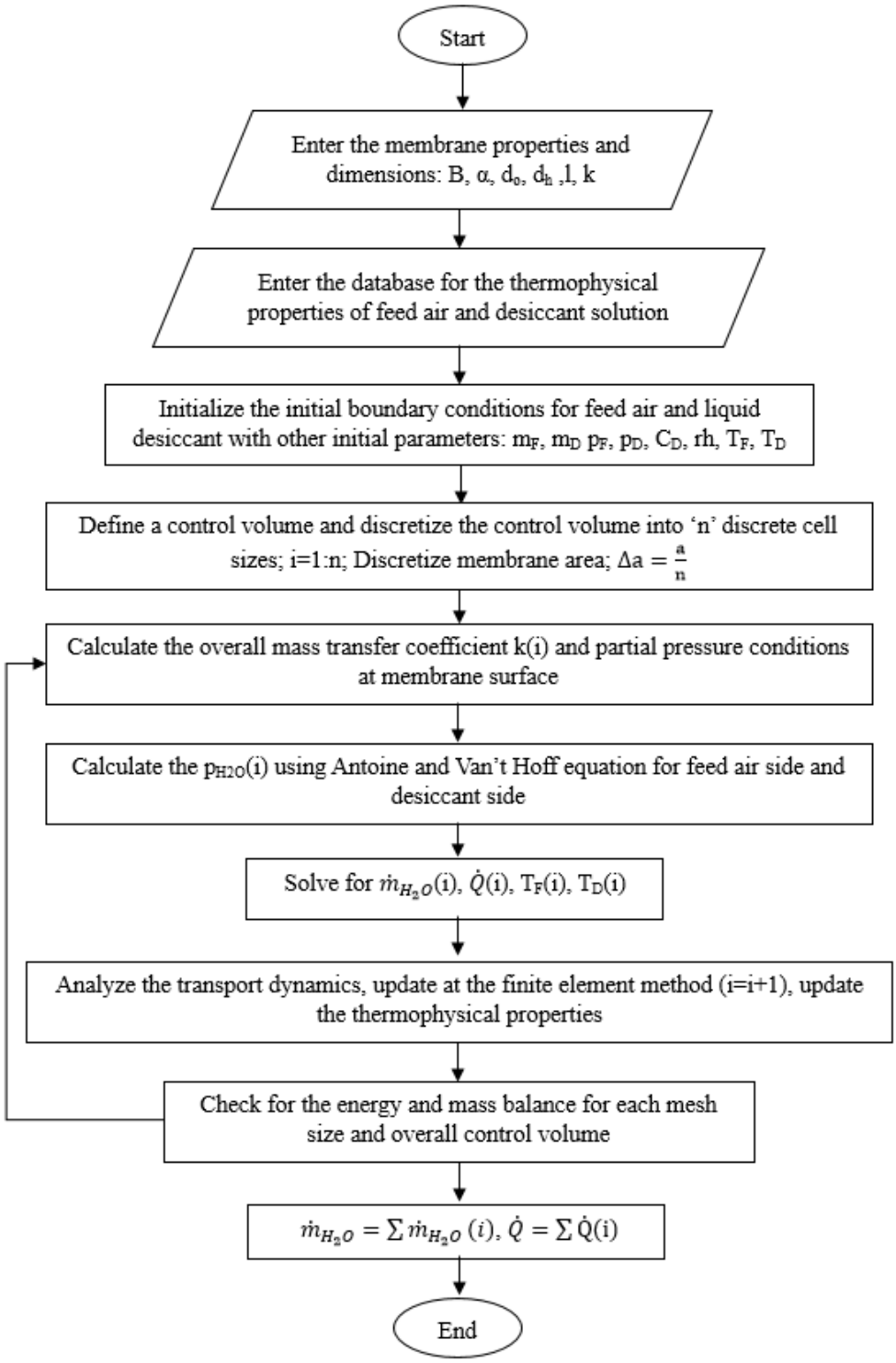

Figure 5.6. Finite element model used to numerically solve heat and mass transfer across each finite membrane element and determine the resulting energy and mass balance of each control volume throughout the liquid desiccant and air feed boundary layers.

Table 5.1. Baseline simulation input parameters.

Membrane	
Membrane area a	1 m^2
Number of fibers	12,600
Fiber thickness L	55×10^{-6} m
Fiber diameter (outer) d	300×10^{-6} m
Shell inner diameter D	6×10^{-2} m
Membrane vapor permeability B	3.94×10^{-6} g m^{-2} s^{-1} Pa^{-1} [72]
Membrane thermal conductivity k	0.19 W m^{-1} K^{-1} [118]
Water cooled chiller COP	5 [136]
Liquid Desiccant Supply	
Fertilizer solute	$Ca(NO_3)_2 4H_2O$
Saturation solubility	1.29 g/g_{water}
Mass flow	2.1 lpm
Convection coefficient desiccant h_D	$0.36 \frac{k_D}{d_h} Re^{0.55} Pr^{0.33}$ [120]
Air Feed Supply	
Humidity	70 % rh
Temperature	25 °C
Mass flow	5 slpm
Convection coefficient of air feed h_F	$0.023 \frac{k_F}{d} Re^{0.8} Pr^{0.3}$ [121]

The model was also verified in terms of mass and energy balance for each discretized cell as well as the overall control volume.

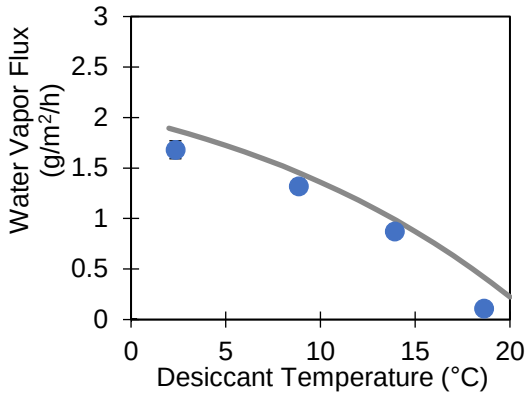

Figure 5.7. Water vapor flux across a range of liquid desiccant temperatures with model (grey line) and experimental results (blues circles). Given liquid desiccant solution with $Ca(NO_3)_2$ fertilizer at concentration of 996.7 ± 0.2 g/l, and air temperature of 25.3 ± 0.1 °C and rh=71 ± 2 %

5.5 Results

5.5.1 Effect of Liquid Desiccant Dilution due to Batch Process Re-Circulation

The fertilizer-based liquid desiccant requires no regeneration, instead, it is recirculated through the membrane system until the solution is sufficiently diluted from water vapor permeate before routing it to the plants. At lower desiccant temperatures higher dehumidification potential can offset the dilution of the fertilizer. However, operating at lower temperature will increase the cooling energy required and thus, the specific energy for dehumidification. The tradeoff between maintaining high dehumidification rates at low desiccant temperature and low specific energy at different range of temperatures is shown in Figure 5.5. However, operating at lower desiccant temperatures and higher concentration yields significantly higher dehumidification rates, as indicated in the figure, a balance should be made because the minimum energy rate does not overlap with the maximum value of flux.

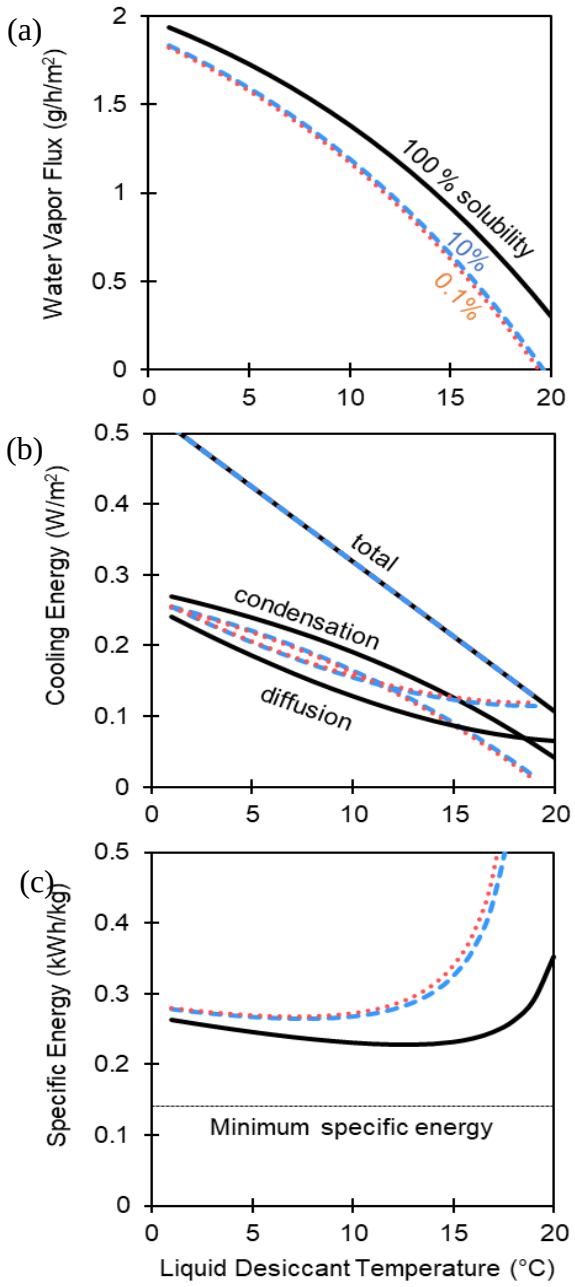

Figure 5.8. Water vapors permeate flux (a), cooling energy added to desiccant (b), and the resulting specific power density for cooling (c) across a range of liquid desiccant temperatures. Given liquid desiccant solution with Ca(NO3)2 fertilizer at different concentration based on the solubility percentage of 0.1% (blue dotted line), 10% (red dashed line) and at 100% at 1.28 g/gwater (black solid line), and given air feed with temperature of 25 °C and 70 % relative humidity.

It is observed from Figure 5.8 that the minimum specific energy value from cooling the desiccant shifts to the left when the concentration decreases during the dehumidification process. For the saturated solution concentration, we reach the minimum specific energy at 13 ^{o}C while the minimum specific energy at a temperature of 8 ^{o}C when the desiccant reaches a solubility of 0.1% of the equilibrium. Furthermore, due to the greater flux for highly concentrated solution, the specific energy of the system can be reduced with higher concentration. For example, at 0.1% solubility, the minimum specific energy of 0.27 kWh/kg is obtained for the full solubility solution case at a temperature of 18 ^{o}C. Thus, this difference in concentration from 0.1% solubility to 99% solubility is equivalent to a temperature reduction of 10 ^{o}C.

5.5.2 Effect of Operating at Different Liquid Desiccant and Air Feed Circulation Rates

In addition, flow conditions can affect the specific energy results and magnitude. Figure 5.9 shows the effect of the desiccant flowrate on the flux (a) and specific energy (b) across a range of desiccant temperature. The flow rate in the base case scenario is depicted in blue solid line, and two additional flowrates are considered for this analysis. The two limits of desiccant flow rate in the used PDMS membrane module are 0.5 lpm (dotted red line) and 6 lpm (green dashed line) as shown in Fig. 5.9. These are the lowest and highest flowrates based the PDMS membrane module size.

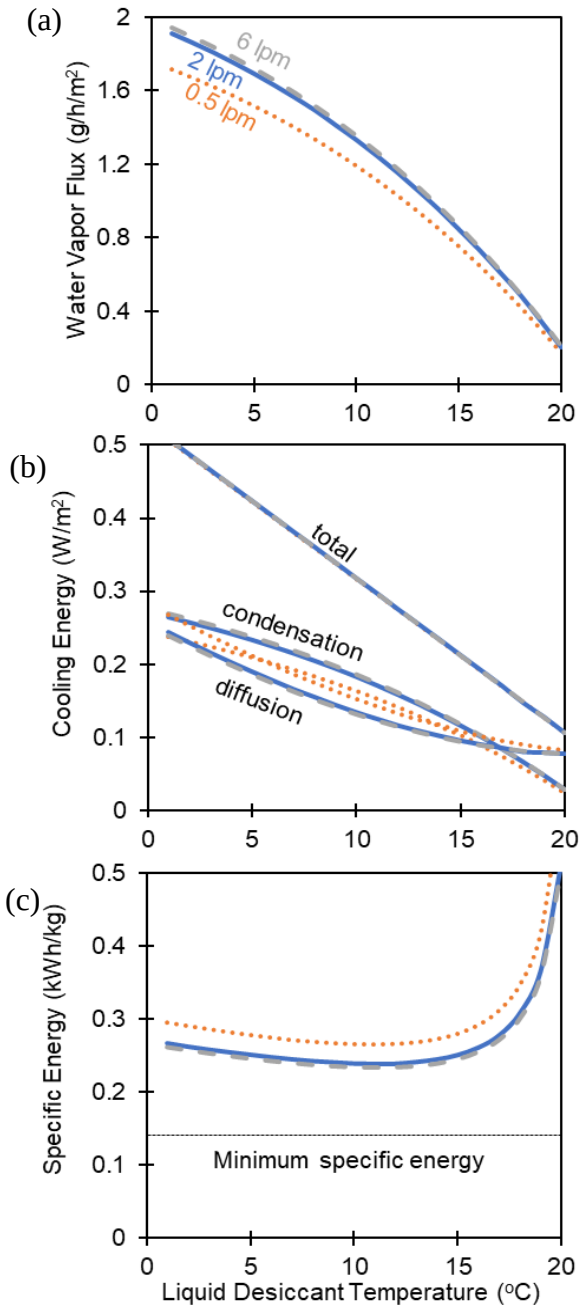

Figure 5.9. Water vapors permeate flux (a), cooling energy for maintaining the desiccant temperature (b) and the resulting specific energy consumption (c) across a range of liquid desiccant temperatures for a desiccant flow rate of 2 lpm (blue solid line), 0.5 lpm (red pointed line) and 6 lpm (green dashed line). Given liquid desiccant solution with $Ca(NO_3)_2$ fertilizer at concentration of 75% of solubility, and given air feed with temperature of 25 °C and 70 % relative humidity at 5 lpm flow rate.

It is observed that the fertilizer solution flow rate had minimal effect on the flux and specific energy when varied from 2 lpm to 6 lpm under these conditions. However, adjusting the flowrate to the minimum limit of liquid desiccant flow rate required for PDMS membrane reduced the water vapor permeate flux, causing the specific energy to rise. It caused the decrease in latent heat due to lower water vapor transport. However, the diffusion term of the energy balance increased, resulting in the total cooling being unaffected by this decrease in flow rate. Further analysis on this parameter dependent on the scale of the system and condition should be always considered during the design of the system to work at the optimal condition that leads to the lowest energy consumption.

Additional major operating condition that can affect the heat flux across the membrane is the air flowrate in the system. Figure 5.10. shows the effect of variation in the airflow rates on the water vapor flux and the consequent specific energy.

Higher flux is achieved with increasing air flow rate. However, even with higher dehumidification rates, the specific energy acquired for the higher flow rates is larger due to the rise in the heat flux paired with the mass transfer. In contrast, a lower air flow rate of 1 lpm results in a decreased dehumidification rate and a drop in specific energy and approaching the minimum specific energy line, because the total energy needed for desiccant cooling is reduced and is more significant than the dehumidification rate.

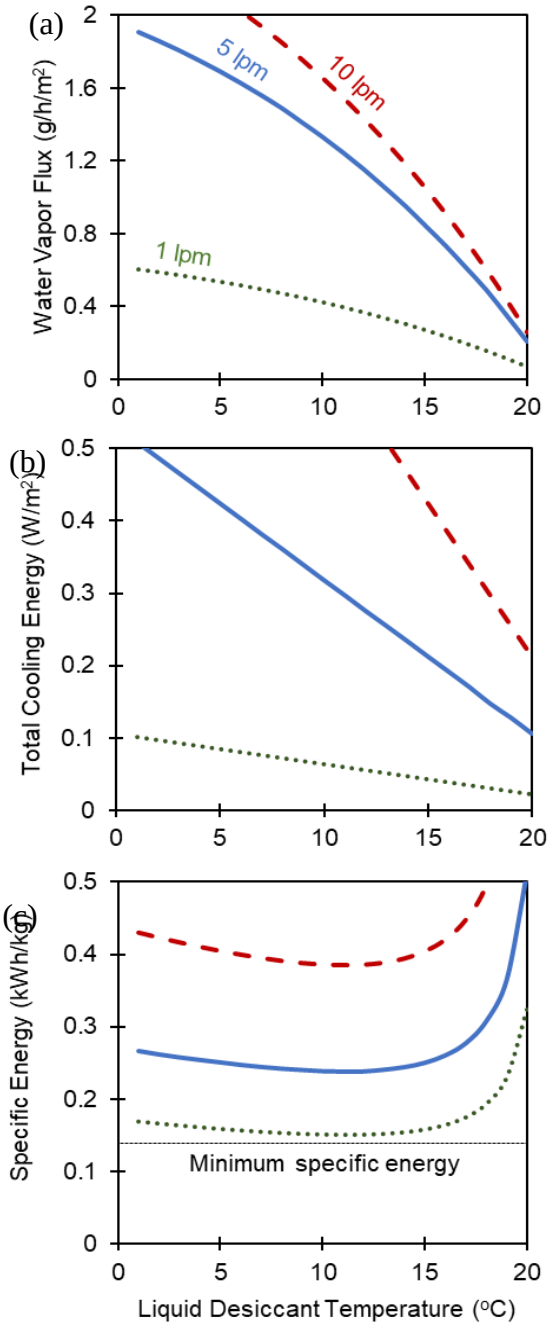

Figure 5.10. Water vapors permeate flux (a), cooling energy for maintaining the desiccant temperature (b) and the resulting specific energy consumption (c) across a range of liquid desiccant temperatures for air flow rate of 1 lpm (pointed orange line), 5 lpm (solid blue line) and 10 lpm (dashed purple line). Given liquid desiccant solution flow rate of 2 lpm with $Ca(NO_3)_2$ fertilizer at concentration of 75% of solubility, and given air feed with temperature of 25 °C and 70 % relative humidity.

Figure 5.11 depicts the heat flux, demonstrating that, even if the latent heat gained by the liquid desiccant side increases in accordance with the water vapor flux trend, the major dynamic affecting the specific energy is the heat transfer between the air and the desiccant, which is related to the increase or decrease in air flow rate and the residence time on the heat flux ratings. The system's energy efficiency will decline as air flow rates rises because condensation will cause the diffusion heat rate to surpass the latent heat rate.

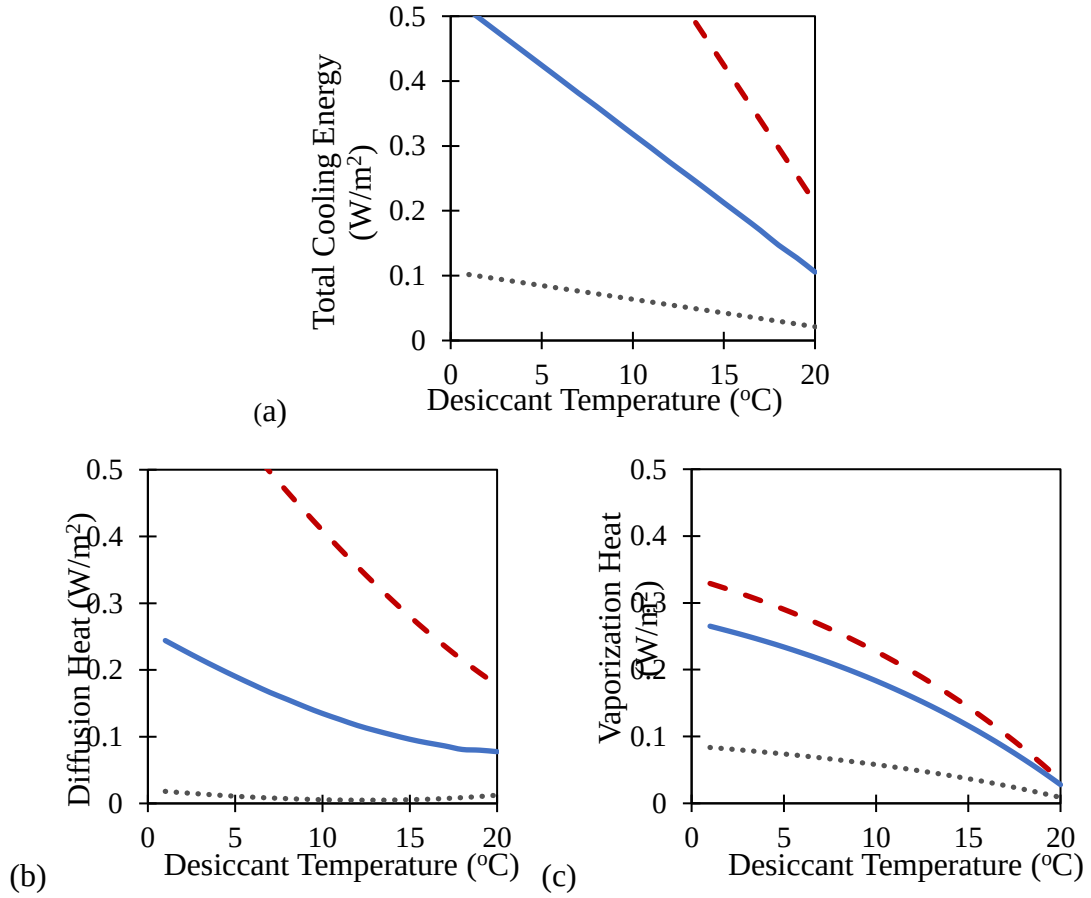

Figure 5.11. Heat Flux between the air and desiccant flow rate that need to be added as total cooling energy for the desiccant (a) that consist of the vaporization heat flux and the diffusion heat flux (b) across a range of liquid desiccant temperatures for air flow rate of 1 lpm (pointed orange line), 5 lpm (solid blue line) and 10 lpm (dashed purple line). Given base case scenario conditions.

Because the fluid with a lower heat transfer coefficient value regulates the overall heat transfer, and because air has a lower heat transfer coefficient than liquid desiccant in the dehumidification system, it dominates the specific energy analysis. The heat transfer coefficient of air improves with increased air flow rate, but it still falls far short of the heat transfer coefficient of liquid desiccant, and the rate at which water vapor is removed is also increased. Thus, careful consideration and optimization of the parameter is needed to be able to increase the efficiency of the system. As the air flow rate controlled the heat of diffusion and a significant effect is presented from this parameter, an optimization study of this parameter is primordial to increase the dehumidification rate and at the same time minimizing the specific energy of the system needed for a certain dehumidification target.

5.5.3 Effect of Membrane Properties

Membrane selection and characteristics appeared to be a significant factor in the performance of the dehumidification system. Water vapor mass permeate is directly related to membrane permeability, where dehumidification occurs in the selective membrane and moisture in the air transfers through the dense hydrophobic layer of the membrane, driven by vapor pressure gradient. As a result, selecting the best membrane material with the lowest transfer resistance is critical for overall performance [137].

Figure 5.12 shows the effect of membrane permeability across the range of desiccant temperatures. The PEBAX membrane, which has a high permeability of 5000 GPU [138], and Polyethersulfone, which has a lower permeability of 444 GPU [52,139], are used to compare flux and specific energy with the selected PDMS membrane. As we can see, the performance of the system increased following the permeability increase with the specific energy as low as 0.16 kWh/kg.

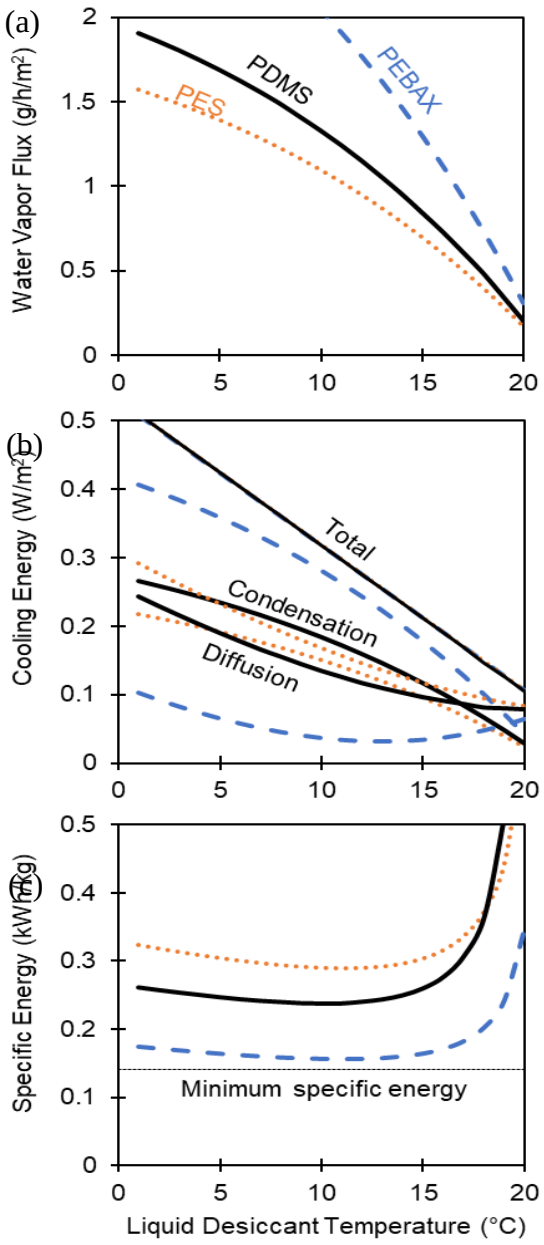

Figure 5.12. Water vapors permeate flux (a), cooling energy load (b) and the specific power density for cooling (c) across a range desiccant temperature. Given PEBAX permeability of 5000 GPU [138] and Polyethersulfone (PES) permeability = 444 GPU [52,139] Given conditions of the base case scenario.

As noted from the Figure 5.13, it is the lowest specific energy that occurs even with higher permeability. Along with the better performance, higher permeable membrane can handle a wider range of desiccant temperatures as the specific energy remains under 0.5 kWh/kg even at 20 ^{o}C. Thus, with better membrane, controlling the temperature of the desiccant becomes less critical to keep the specific energy below standard levels, and it shifts more for dehumidification control purpose in the system.

Figure 5.13 shows the effect of membrane permeability characteristic on the performance of the dehumidification system. As the membrane becomes more permeable to water vapor and flux increases, the specific energy for liquid desiccant cooling decreases until its asymptotes to a minimum value of 0.16 kWh/kg. Thus, even if we consider a membrane with very high permeability, a maximum related to the equilibrium between the two fluids across the membrane will limit the flux and thus the minimum specific energy that can be reached. When permeate flux increases, the desiccant gains additional latent heat that need to be removed with the cooling system. The specific energy still falls with increasing permeability despite the larger cooling demand associated to permeate because the net flux has a greater impact on the system. To ensure that the specific energy does not exceed the maximum value required for dehumidification [32], a membrane with permeability less than 1.2×10^{-6} g/s/Pa/m^2 cannot be used under the base case scenario conditions. It is also important to note that at permeabilities higher than 10^{-5} g/s/Pa/m^2, where the flux seemed to reach it maximum, the specific energy approaches the thermodynamic minimum specific latent energy. The permeability value of 10^{-5} g/s/Pa/m^2 is only a limit for this specific case, where we have a certain thermal conductivity, a certain ratio of flow rates and membrane area.

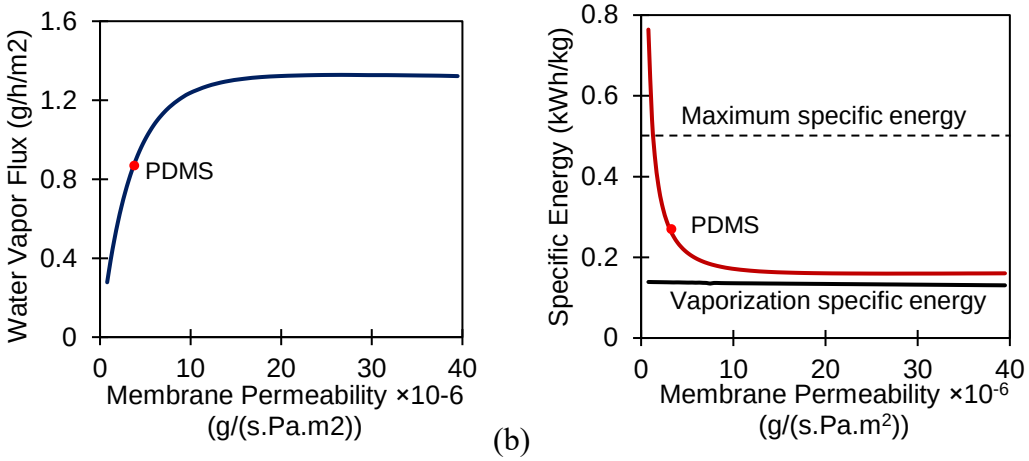

Figure. 5.13. Water vapors permeate flux (a) and the specific energy for cooling (b) across a range of membrane permeability values. Given conditions of the base case scenario.

5.6 Conclusions

Greenhouse humidity control is crucial for optimal plant growth but can be energy intensive. Fertilizer dehumidification offers advantages over traditional methods by avoiding air-desiccant contact and potential contamination. Additionally, membrane-based fertilizer dehumidification is expected to consume less energy compared to desiccant dehumidification, due to the absence of solution regeneration. Our previous research validated this concept under a variety of operational and plant environmental conditions [134].

In this study we investigated the impact of different operational parameters on the specific energy required for dehumidifying the controlled plant environment sustainably. Our findings revealed that lower desiccant temperatures lead to a higher rate of water vapor removal. However, this also resulted in additional energy needed for desiccant cooling. Hence, a trade-off between the rate of water vapor removal and the energy load must be made to ensure effective dehumidification while keeping energy costs low. We defined the specific energy as the ratio of cooling energy load to the dehumidification rate and

examined the impacts of various operational factors such as desiccant temperature, air and desiccant flow rate, and fertilizer concentration on specific energy using theoretical modeling and parametric study.

Our study showed that desiccant temperature and air flow rate had the most significant impact on specific energy, followed by fertilizer concentration. This effect is due to the system's dynamic relationship between heat and mass transfer, specifically the relationship between permeate flux and the heat gained by the desiccant during vapor condensation. We examined the impact of other operational factors over a range of desiccant temperatures to determine the ideal temperature that provides the lowest specific energy for each situation. The study revealed that the sensible heat flux between the two fluids, which was significantly affected by air flow rate and the latent heat associated with variations in water vapor mass transfer, shifted drastically with different air residence times. The lower air flow rates had a lower specific energy value of 0.15 kWh/kg but had lower dehumidification performance compared to higher flow rates. The energy performance of the system, however, did not significantly change as the desiccant flow rate increased from the base case scenario's 2 lpm to the membrane module's maximum flow rate of 6 lpm.

Our findings also indicated an unfavorable increase in specific energy as the fertilizer concentration decreased. The optimal desiccant temperature for each concentration value also varied significantly, highlighting the need for a control system to account for fertilizer dilution during the batch dehumidification process with no regeneration.

This study also investigated the impact of membrane water vapor permeance on the proposed dehumidification system for maintaining sustainable plant growth conditions. The findings showed that the membrane permeability had a significant effect on the

system's performance, improving it until it reached a plateau at 10^{-5} g/s/Pa/m2. Furthermore, we compared the permeability of different membrane materials and found that better membranes allowed for a wider range of desiccant temperatures, resulting in improved dehumidification and energy performance.

However, our primary energy analysis indicated that further research is required to optimize the overall performance of the dehumidification system and its associated cooling unit. Additionally, the batch process of the fertilizer solution and the specific dehumidification rate required for different crop types need to be considered to ensure optimal performance.

5.7 Nomenclature

a	membrane surface area (m^2)
B	vapor permeability (g m^{-2} s^{-1} Pa^{-1})
c	concentration of desiccant solute (mol l^{-1})
COP	Coefficient of performance
c_p	specific heat (J K^{-1} g^{-1})
d	diameter (m)
d_h	hydraulic diameter (m)
e	Specific energy (kWh/kg)
E	Energy consumption (W/m^2)
H_c	heat of condensation (J g^{-1})
h	thermal convection coefficient (W m^{-2} K^{-1})
i	number of ions
J	vapor flux (g m^{-2} s^{-1})
K	mass transfer coefficient (g m^{-2} s^{-1} Pa^{-1})
k	thermal conductivity (W m^{-1} K^{-1})

L	membrane thickness (m)
M	molar mass (g mol^{-1})
m	mass (g)
Pr	Prandtl number
p	pressure (Pa)
$\dot{q}$	heat flux (W m^{-2})
$\dot{Q}_{cooling}$	Cooling load (W m^{-2})
R	gas constant (J mol^{-1} K^{-1})
Re	Reynolds number
r	thermal resistance (K m^2 W^{-1})
rh	relative humidity (%)
x	mole fraction of water (mol/mol)
T	temperature (K)
V_m	molar volume (m^3 mol^{-1})
w	humidity mass ratio (g g^{-1})
Greek symbols:	
π	osmotic pressure (Pa)
Subscripts and Superscripts:	
‘	standard temperature and pressure
D	liquid desiccant
F	air feed
H_2O	water / vapor
in	membrane module inlet
m	membrane surface
o	pure water / saturation
out	membrane module outlet

CHAPTER SIX

CONLUSIONS

6.1 Contributions

This dissertation introduces two novel membrane-based concepts for energy and water recovery. Taking into account the ongoing efforts for moving towards clean energy, a complete change from fossil fuels may take several decades. Thus, improving the efficiency and performance of existing technologies or the introduction of new alternative technologies that reduce the energy consumption is important to mitigate greenhouse gas emissions during this transition.

6.1.1 New concept for generating power from water vapor

Chapter Two provides the first ever demonstration of power generation from membrane gas permeation with water vapor gradients. We were able to obtain a power density of 57 mW/m^2 from water vapor flux, and power density of 11.5 mW/m^2 from net gas flux, at low applied pressures and at low water vapor gradient of 2 vol.% using a PDMS membrane. A finite element model for mass transfer across the dense membrane was defined and validated against experimental results. This model was then used to illustrate the significance of membrane properties, such as permeability and selectivity, on the potential power density to recover from flue exhaust. We showed a possible improvement in energy potential up to 600 mW/m^2 were obtained when highly permeable and selective PEBA membranes are supplied with feed at 20 vol.% water vapor.

6.1.2 New concept for generating power from carbon dioxide

Chapter Three introduced the novel concept of using CO_2 gas permeation to generate an expanding mass of pressurized gas for potential power generation. With experimental validation, this is the first ever demonstration of power from CO_2 sweep gas permeation. In addition, this work shows the first ever demonstration of CO_2 permeate against an applied pressure. A power up to 1.08 W/m^2 from CO_2 permeate was observed, that compares very well to the literature. A power density up to 0.37 W/m^2 was also found from net flux when CO_2 feed concentrations of 20 % was used, assuming ideal machine with 100% energy conversion at the compressor and turbine. Next, an analysis on the energy conversion system efficiencies was performed, and it showed a significant reduction in net power potential when the efficiency losses were considered. However, power potential of the process can be optimized with operating conditions such as feed and sweep flow rates as well as with membrane properties improvement to offset the losses from the reverse flux on the system.

6.1.3 New concept of using fertilizer as a liquid desiccant

In Chapter Four, the liquid fertilizer dehumidification process showed promising outcomes with dehumidification rates using a PDMS hollow fiber membrane by maintaining the outlet humidity at desirable values over a range of inlet conditions. This contribution to the literature may open up new possibilities for energy efficient dehumidification and water recycling in indoor plant environments. A variety of common fertilizer solutions were shown to equally perform, including $Ca(NO_3)_2$, NH_4Cl, and $(NH_4)_2SO_4$, suggesting that a wide variety of fertilizers can be considered and validating the novel concept of using fertilizer-based solutions as liquid desiccants for

dehumidification of indoor plant environments. I then introduced a 2-D model for heat and mass transfer across the dense membrane, and it was also validated against experimental results. A dehumidification rate up to 1.90 g/m^2/h of water vapor flux and 5.03 g/kg of water vapor removal rate were obtained under favorable conditions.

One of the primary features of fertilizer-based liquid desiccant is, unlike conventional desiccant system, it requires no energy intensive regeneration. Yet, maintaining a thermal gradient between warm feed air and cool liquid desiccant was shown to be a key variable for achieving higher dehumidification rates. However, this will add to the energy consumption and thus to higher operational costs.

Therefore, in Chapter Five, an energy analysis was presented to show the effect of desiccant temperature on the energy performance of the system. And so, a theoretical modeling and a parametric study and analysis were performed to investigate the effects of operating conditions, such as air and desiccant flow rates and fertilizer concentration, all as a function of desiccant temperatures on the specific energy of the system. The latter was shown to be greatly influenced by the desiccant temperature and air flow rate followed by the fertilizer concentration. Since operating conditions affect both the dehumidification rate and the cooling energy consumption to maintain a thermal gradient, an optimal desiccant temperature with a minimum specific energy was observed in each different condition. As a result, a specific energy as low as 0.15 kWh/ kg was achieved under certain conditions and for optimized desiccant temperature and air flow rate, but with the consequence of lower dehumidification performance. On the other hand, the condition of fertilizer concentration showed an unfavorable increase of the specific energy with the optimal desiccant temperature shifting following the incremented decrease in

concentration. And this shift in the optimal desiccant temperature for each concentration value indicated the critical need of a temperature control system to take into account the dilution of fertilizer during the batch dehumidification when no regeneration is utilized. At the end, I studied the effect of the membrane water vapor permeance on the proposed system. In this analysis, the membrane permeability showed to improve the performance of the system until it plateaued after reaching a permeability of 10^{-5} g/s/Pa/m^2 where higher permeability will show no effect on the dehumidification and the related specific energy.

6.2 Future Work

In the new proposed process for recovering energy from water vapor and CO_2 gas permeation, the optimization of certain parameters, such as the sweep flow rate, and its effect on the net energy density should be considered in future studies. In addition, consideration of the overall mass transfer of multiple gases contained in the feed exhaust gas are still unaccounted for. Therefore, promising improvements can be considered in future work, foremost the multi gas gradients between the exhaust and ambient (mainly both water vapor and CO_2), that has the potential of increasing the net permeate flux and hence the net power density leading to higher power potential and improving the overall performance.

In addition, the effect of the thermal gradient in the system should be considered in future work, as the exhaust flue gas is expected to have higher temperatures than the ambient sweep air. Therefore, heat and mass coupled transfer across the membrane will hence increase the enthalpy exchange to the pressurized sweep before entering the turbine.

As a result, we expect the additional heat flux to improve the energy performance and to overcome the efficiency losses from the non-ideal energy conversion system.

For the second proposed dehumidification system, additional analysis should also be considered. Mainly the transient dynamics in the system, as the dehumidification rate largely depends on the balance between dehumidification and the indoor relative humidity increase from plant evapotranspiration. This should also include evaluation of the amount of fertilizer per unit time needed per plant and whether the batch system dehumidification capacity can be balanced with the plants evapotranspiration rate to be removed.

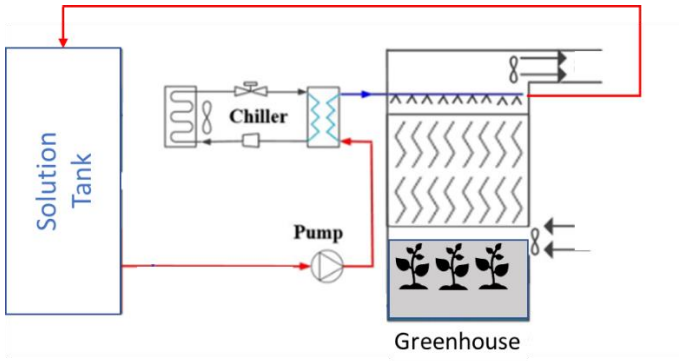

Figure 6.1 A schematic of the scenario case of a greenhouse with specific crop with integrated fertilizer desiccant to control the humidity. The chiller is to control and keep the desiccant temperature at the required levels.

To perform this study, a specific case scenario of the batch process for certain crop should be considered as shown in Figure 5.1, and the system performance will be evaluated using the validated model for the liquid desiccant process. Then, a study on the system sizing needs to be performed to ensure a balance between the permeate flux in the membrane system and the transpiration rate of the plant to maintain the humidity at the requires levels. Finally, an analysis on improving the water vapor flux will be conducted over a range of controlled variables to optimize the process from the dehumidification side along with specific energy consideration for each specific scenario.

REFERENCES

[1] U.S Information Energy Administration. 2022. September 2022 Total Energy Monthly Data. https://www.eia.gov/totalenergy/data/monthly/

[2] Database of State Incentives for Renewables and Efficiency (DSIRE). 2018. Accessed October 2022. https://www.dsireusa.org/

[3] A. Mardiana, and S. B. Riffat. "Building energy consumption and carbon dioxide emissions: threat to climate change." Journal of Earth Science & Climatic Change, vol. S3:1, 2015.

[4] H. Bai, J. Zhu, X. Chen, J. Chu, Y. Cui, Y. Yan, "Steady-state performance evaluation and energy assessment of a complete membrane-based liquid desiccant dehumidification system", Applied Energy, vol. 258, 114082, 2020.

[5] S. Englart, and K. Rajski, "Performance Investigation of a Hollow Fiber Membrane-Based Desiccant Liquid Air Dehumidification System". Energies, vol. 14, 3320, 2021.

[6] H. Lim, K. Goh, M. Tian, R. Wang, "Membrane-based air dehumidification: A comparative review on membrane contactors, separative membranes and adsorptive membranes", Chinese Journal of Chemical Engineering, vol. 41, pp. 121-144, 2022.

[7] J. Woods, "Membrane processes for heating, ventilation, and air conditioning", Renewable and Sustainable Energy Reviews, Volume 33, pp. 290-304, 2014.

[8] P.A. Kallenberger, M. Fröba, "Water harvesting from air with a hygroscopic salt in a hydrogel-derived matrix", Communication Chemistry, vol.1 (1), pp. 1-6, 2018.

[9] T. C. Merkel, H. Lin, X. Wei and R. Baker, "Power plant post-combustion carbon dioxide capture: An opportunity for membranes", Journal of Membrane Science, vol. 359, pp. 126-139, 2010.

[10] R. W. Baker, B. Freeman, J. Kniep, X. Wei and T. Merkel, "CO2 capture from natural gas power plants using selective exhaust gas recycle membrane designs", International Journal of Greenhous Gas Control, vol. 66, pp. 35-47, 2017.

[11] H. V. M. Hamelers, O. Schaetzle, J. M. Paz-García, P. M. Biesheuvel, and C. J. N. Buisman, "Harvesting Energy from CO2 Emissions", Environmental Science and Technology Letters, vol. 1, pp. 31−35, 2014.

[12] J. M. Paz-Garcia, J. E. Dykstra, P. M. Biesheuvel and H. V. M. Hamelers, "Energy from CO2 using capacitive electrodes: A model for energy extraction cycles", Journal of Colloid and Interface Science, vol. 442, pp. 103-109, 2015.

[13] S. Porada, D. Weingarth, H. V. M. Hamelers, M. Bryjak, V. Presser and P. M. Biesheuvel, "Carbon flow electrodes for continuous operation of capacitive deionization and capacitive mixing energy generation", Journal of Material Chemistry A, vol. 2, pp. 9313-9321, 2014.

[14] T. Kim, B. E. Logan, and C. A. Gorski, "A pH-Gradient Flow Cell for Converting Waste CO2 into Electricity". Environmental Science and Technology Letters, vol. 4, pp. 49−53, 2017.

[15] K. Park, D. Y. Kim and D. R. Yang, "Theoretical Analysis of Pressure Retarded Membrane Distillation (PRMD) Process for Simultaneous Production of Water and Electricity", Industrial & Engineering Chemistry Research, vol. 56, pp. 14888−14901, 2017.

[16] B. E. Logan and M. Elimelech, "Membrane-based processes for sustainable power generation using water", Nature, vol. 488, pp. 313-319, 2012.

[17] J. Maisonneuve, P. Pillay and C. B. Laflamme, "Pressure-retarded osmotic power system model considering non-ideal effects", Renewable Energy, vol. 75, pp. 416-424, 2015.

[18] J. Maisonneuve and S. Chintalacheruvu, "Increasing osmotic power and energy with maximum power point tracking", Applied Energy, vol. 238, pp. 683-695, 2019.

[19] T. Qian, J. Dieleman, A. Elings, G. Arie, L.F.M. Marcelis, and O. Kooten, "Comparison of climate and production in closed, semi-closed and open greenhouses", Acta Horticulturae, vol. 893, 2009.

[20] D. Dannehl, C. Huber, T. Rocksch, S. Huyskens-Keil, and U. Schmidt, "Interactions between changing climate conditions in a semi-closed greenhouse and plant development, fruit yield, and health-promoting plant compounds of tomatoes", Scientia Horticulturae, vol. 138, pp. 235-243, 2012.

[21] D. Dannehl, J. Suhl, S. Huyskens-Keil, C. Ulrichs, and U. Schmidt, "Effects of a special solar collector greenhouse on water balance, fruit quantity and fruit quality of tomatoes", Agricultural Water Management, vol. 134, pp. 14-23, 2014.

[22] P. Padmanabhan, A. Cheema, and G. Paliyath, "Solanaceous Fruits Including Tomato, Eggplant, and Peppers", Encyclopedia of Food and Health, Academic Press, pp.24-32, 2016.

[23] J.J.G. Opdam, G.G. Schoonderbeek, E.M.B. Heller, and G. Arie, “Closed greenhouse: A starting point for sustainable entrepreneurship in horticulture”. Acta Horticulturae, vol. 691, pp. 517-524, 2005.

[24] C. Stanghellini, “Horticultural production in greenhouses: Efficient use of water”, Acta Horticulturae, vol. 1034, pp. 25-32, 2014.

[25] N. Katsoulas, A. Sapounas, F. De Zwart, J.A. Dieleman, and C. Stanghellini, “Reducing ventilation requirements in semi-closed greenhouses increases water use efficiency”, Agricultural Water Management, vol. 156, pp. 90-99, 2015.

[26] L.D. Albright and M.L. Behler, “An air-liquid-air heat exchanger for greenhouse humidity control”, Transactions of the American Society of Agricultural Engineers, vol.27, pp. 1524-1530, 1986.

[27] D.R. Rousse, D.Y. Martin, R. Thériault, F. Léveillée, and R. Boily, “Heat recovery in greenhouses: a practical solution”, Applied Thermal Engineering, vol. 20(8), pp. 687–706, 2000.

[28] J.B. Campen, G.P.A. Bot, and H.F de Zwart, “Dehumidification of Greenhouses at Northern Latitudes”, Biosystems Engineering, vol. 86(4), pp. 487–493, 2003.

[29] L.Z. Zhang, “Progress on heat and moisture recovery with membranes: From fundamentals to engineering applications”, Energy Conversion and Management, vol. 63, pp. 173–195, 2012.

[30] R. Lefers, N.M.S. Bettahalli, N.V. Fedoroff, S. Nunes, and T. Leiknes T, “Vacuum membrane distillation of liquid desiccants utilizing hollow fiber membranes”, Separation and Purification Technology, vol. 199, pp. 57–63, 2018.

[31] Ahmed H. Abdel-Salam, Carey J. Simonson, “Annual evaluation of energy, environmental and economic performances of a membrane liquid desiccant air conditioning system with/without ERV”, Applied Energy, Volume 116, pp. 134-148, 2014.

[32] Energy Solutions and Cultivate Energy and Optimization, “Codes and Standards Enhancement (CASE) Initiative 2022 California Energy Code”, March 2022.

[33] C. Tang, K. Vafai, C. Gu, K. N. Gloria, M.D. Razaul Karim, “Experimental investigation of dehumidification performance of a vapor compression refrigeration system”, International Communications in Heat and Mass Transfer, Volume 137,2022, 106282.

[34] N. Zhang, S.-Y. Yin, M. Li, “Model-based optimization for a heat pump driven and hollow fiber membrane hybrid two-stage liquid desiccant air dehumidification system”, Applied Energy, Volume 228, 2018, Pages 12-20.

[35] G. T. Rochelle, “Amine scrubbing for CO2 capture”, Science, vol. 325, pp. 1652-1654, 2009.

[36] J. D. Figueroa, T. Fout, S. Plasynski, H. McIlvried and R. D. Srivastava, “Advances in CO2 capture technology: The U.S. Department of Energy’s Carbon Sequestration Program”, International Journal of Greenhouse Gas Control, vol. 2, pp. 9-20, 2008.

[37] E. Favre, “Carbon dioxide recovery from post-combustion processes: Can gas permeation membranes compete with absorption?”, Journal of Membrane Science, vol. 294, pp. 50-59, 2007.

[38] A. Brunetti, F. Scura, G. Barbieri and E. Drioli, “Membrane technologies for CO2 separation”, Journal of Membrane Science, vol. 359, pp. 115-125, 2010.

[39] Y. Huang, T. C. Merkel, and R. W. Baker, “Pressure ratio and its impact on membrane gas separation processes”, Journal of Membrane Science, vol. 463, pp. 33-40, 2014.

[40] D. Gao, Z. Li, H. Zhang, H. Chen, C. Cheng and K. Liang, “Moisture and latent heat recovery from flue gas by nonporous organic membranes”, Journal of Cleaner Production, vol. 225, pp. 1065-1078, 2019

[41] A. P. Straub, N. Y. Yip, S. Lin, J. Lee and M. Elimelech, “Harvesting low-grade heat energy using thermo-osmotic vapour transport through nanoporous membranes”, Nature Energy, vol.1, 16090, 2016.

[42] A. P. Straub and M. Elimelech, “Energy Efficiency and Performance Limiting Effects in Thermo-Osmotic Energy Conversion from Low-Grade Heat’’, Environmental Science & Technology, vol. 51, pp. 12925-12937, 2017.

[43] A. L. Myers and J. M. Prausnitz, “Thermodynamics of Mixed-Gas Adsorption”. American Institute of Chemical Engineers Journal, vol.11, No.1, pp. 121-127, 1965.

[44] S. Lin, A. P. Straub and M. Elimelech, “Thermodynamic limits of extractable energy by pressure retarded osmosis”. Energy and Environmental Science, vol. 7, pp. 2706-2714, 2014.

[45] J.G. Wijmans and R.W. Baker, “The solution-diffusion model: a review”, Journal of Membrane Science, vol. 107, pp. 1-21, 1995.

[46] G. He, Y. Mi, P. Lock Yue and G. Chen. “Theoretical study on concentration polarization in gas separation membrane processes”, Journal of Membrane Science, vol. 153, pp. 243-258, 1999.

[47] K.L. Wang, S.H. McCray, D.D. Newbold and E.L. Cussler, “Hollow fiber air drying”, Journal of Membrane Science, vol. 72, pp. 231-244, 1992.

[48] “Membrane Distillation (MD) - Flat Sheet Membranes | Sterlitech.” https://www.sterlitech.com/membrane-distillation-md.html (accessed March 9, 2020).

[49] “PermSelect 1,000-centimeter sq. membrane module | PermSelect-MedArray.” https://permselect.com/products/permselectr-1000-centimeter-sq-membrane-module (accessed March 9, 2020).

[50] N. Yip, D. A. Vermaas, K. Nijmeijer, and M. Elimelech, “Thermodynamic, Energy Efficiency, and Power Density Analysis of Reverse Electrodialysis Power Generation with Natural Salinity Gradients”, Environmental Science and Technology, vol. 48, pp. 4925−4936, 2014.

[51] B. Freeman, “Basis of Permeability/Selectivity Tradeoff Relations in Polymeric Gas Separation Membranes”, Macromolecules, vol. 32, pp. 375-380, 1999.

[52] S.J. Metz, W.J.C. van de Ven, J. Potreck, M.H.V. Mulder and M. Wessling, “Transport of water vapor and inert gas mixtures through highly selective and highly permeable polymer membranes”, Journal of Membrane Science, vol. 251, pp. 29–41, 2005.

[53] V. Karanikola, A. F. Corral, H. Jiang, A. E. Sáez, W. P. Ela and R. G. Arnold, ‘Sweeping gas membrane distillation: Numerical simulation of mass and heat transfer in a hollow fiber membrane module’, Journal of Membrane Science, vol. 483 pp. 15–2416, 2015.

[54] A. Droudian, M. Lokesh, S. K. Youn and H. G. Park, “Gas concentration polarization and transport mechanism transition near thin nanoporous and dense polymeric membranes”, Journal of Membrane Science, vol. 567, pp. 1-6, 2018.

[55] W.J. Massman, ‘A review of the molecular diffusivities of H2O, CO2, CH4, CO, O3, SO2, NH3, N2O, NO, and NO2, in air, O2, and N2, near STP’. Atmospheric Environment, vol. 32, No. 6, pp. 1111–1127, 1998.

[56] J. Maisonneuve, C. B. Laflamme and P. Pillay, “Experimental investigation of pressure retarded osmosis for renewable energy conversion: Towards increased net power”, Applied Energy, vol. 164, pp. 425-435, 2019.

[57] M.F. Naguib, J. Maisonneuve, C. B. Laflamme, and P. Pillay, “Modeling Pressure-Retarded Osmotic Power in Commercial Length Membranes”, Renewable Energy, vol. 76, pp. 619–27, 2015.

[58] M.S. Peters, K.D. Timmerhaus and R.E. West, “Plant Design and Economics for Chemical Engineers”, New York: McGraw-Hill, 2003.

[59] R.H. Perry, and D.W. Green, “Perry's Chemical Engineers’ Handbook”, New York: McGraw-Hill, 1997.

[60] G. W. Herbst, T. A. Newell, and H. H. Korst, “Feasibility Study of a Pressure Exchanger in an Air-Cycle Air Conditioner,” Air Conditioning and Refrigeration Center University of Illinois, 1997.

[61] U.S. Department of Energy, “Annual Energy Outlook 2021 with projection to 2050 Narrative”, U.S. Energy Information Administration, Independent Statistics & Analysis, 2021.

[62] U.S. Department of Energy, “U.S. Energy-Related Carbon Dioxide Emissions, 2019”, U.S. Energy Information Administration, Independent Statistics & Analysis, 2020.

[63] L.T. Keyßer, M. Lenzen, “1.5 °C degrowth scenarios suggest the need for new mitigation pathways”, Nature Communication 12, 2676, 2021.

[64] M. Jeuland, T. R. Fetter, Y. Li, S. K. Pattanayak and al, “Is energy the golden thread? A systematic review of the impacts of modern and traditional energy use in low- and middle-income countries”, Renewable and Sustainable Energy Reviews, vol. 135 (110406), 2021.

[65] S. Dong, Z. Wang, M. Sheng, Z. Qiao and J. Wang, “High-performance multi-layer composite membrane with enhanced interlayer compatibility and surface crosslinking for CO2 separation”, Journal of Membrane Science, vol. 610, 118221, 2020.

[66] P. Maas, N. Nauels, L. Zhao, P. Markewitz, V. Scherer, M. Modigell, D. Stolten and J.-F. Hake, “Energetic and economic evaluation of membrane-based carbon capture routes for power plant processes”, International Journal of Greenhouse Gas Control, vol. 44, pp. 124–139, 2016.

[67] L. Chen, F. Sun, C. Wu and R.L. Kiang, “Theoretical analysis of the performance of a regenerative closed Brayton cycle with internal irreversibilities”, Energy Conversion and Management, vol. 38 (9), pp. 871-877, 1997.

[68] S. Loeb, “Production of energy from concentrated brines by pressure-retarded osmosis: I. Preliminary technical and economic correlations”, Journal of Membrane Science, vol. 1, pp. 49-63, 1976.

[69] S. Moussaddy, G. Yuan & J. Maisonneuve, “A new concept for generating mechanical work from gas permeation”. Journal of Membrane Science, vol.614, pp. 118489, 2020.

[70] T.C. Merkel, V.I. Bondar, K. Nagai, B.D. Freeman, and I. Pinnau, “Gas sorption, diffusion, and permeation in poly(dimethylsiloxane)”. Journal of Polymer Science: Part B: Polymer Physics, vol. 38, pp.415– 434, 2000.

[71] M. Scholz, T. Harlacher, T. Melin and M. Wessling “Modeling Gas Permeation by Linking Nonideal Effects”, Industrial & Engineering Chemistry Research, vol 52, pp. 1079−1088, 2013.

[72] M. Sadrzadeh, K. Shahidi, and T. Mohammadi, “Effect of operating parameters on pure and mixed gas permeation properties of a synthesized composite PDMS/PA membrane,” Journal of Membrane Science, vol. 342, no. 1–2, pp. 327–340, 2009.

[73] L. S. White, K. D. Amo, T. Wu, T. C. Merkel, “Extended field trials of Polaris sweep modules for carbon capture”, Journal of Membrane Science, vol 542, pp 217–225, 2017.

[74] J.R. Schramski, C.B. Woodson, and J.H. Brown, “Energy use and the sustainability of intensifying food production”, Nature Sustainability, vol. 3, pp. 257–259, 2020.

[75] M. Herrero, P.K. Thornton, D. Mason-D’Croz, J. Palmer, T.G. Benton, B.L. Bodirsky, J.R. Bogard, A. Hall, B. Lee, K. Nyborg, P. Pradhan, G.D. Bonnett, B.A. Bryan, B.M. Campbell, S. Christensen, M. Clark, M.T. Cook, I.J.M. de Boer, C. Downs, K. Dizyee, C. Folberth, C.M. Godde, J.S. Gerber, M. Grundy, P. Havlik, A. Jarvis, R. King, A.M. Loboguerrero, M.A. Lopes, C.L. McIntyre, R. Naylor, J. Navarro, M. Obersteiner, A. Parodi, M.B. Peoples, I. Pikaar, A. Popp, J. Rockström, M.J. Robertson, P. Smith, E. Stehfest, S.M. Swain, H. Valin, M. van Wijk, H.H.E. van Zanten, S. Vermeulen, J. Vervoort, and P.C. West, “Innovation can accelerate the transition towards a sustainable food system”, Nature Food, vol. 1, pp. 266–272, 2020.

[76] J.A. Foley, N. Ramankutty, K.A. Brauman, E.S. Cassidy, J.S. Gerber, M. Johnston, N.D. Mueller, C. O'Connell, D.K. Ray, P.C. West, C. Balzer, E.M. Bennett, S.R. Carpenter, J. Hill, C. Monfreda, S. Polasky, J. Rockström, J. Sheehan, S. Siebert, D. Tilman, and D.P.M. Zaks, "Solutions for a cultivated planet", Nature, vol. 478, pp. 337–342, 2011.

[77] J. Elser and E. Bennett, "A broken biogeochemical cycle", Nature, vol. 478, pp. 29–31, 2011.

[78] K. Ashley, D. Cordell, and D. Mavinic, "A brief history of phosphorus: From the philosopher's stone to nutrient recovery and reuse", Chemosphere, vol. 84(6), pp. 737–746, 2011.

[79] N.M.S. Bettahalli, R. Lefers, N. Fedoroff, T. Leiknes, and S. Nunes, "Triple-bore hollow fiber membrane contactor for liquid desiccant based air dehumidification", Journal of Membrane Science, vol. 514, pp. 135–142, 2016.

[80] R. Lefers, N.M.S. Bettahalli, S. Nunes, N.V. Fedoroff, P.A. Davies, and T. Leiknes, "Liquid desiccant dehumidification and regeneration process to meet cooling and freshwater needs of desert greenhouses", Desalination and Water Treatment, vol. 57, pp. 23430–23442, 2016.

[81] R. Lefers, N.M.S. Bettahalli, N.V. Fedoroff, N. Ghaffour, P.A. Davies, S. Nunes, and T. Leiknes, "Hollow fibre membrane-based liquid desiccant humidity control for controlled environment agriculture", Biosystems Engineering, vol. 183, pp. 47–57, 2019.

[82] S. Phuntsho, H.K. Shon, S. Hong, S. Lee, and S. Vigneswaran, "A novel low energy fertilizer driven forward osmosis desalination for direct fertigation: Evaluating the performance of fertilizer draw solutions", Journal of Membrane Science, vol. 375, pp. 172–181, 2011.

[83] S. Phuntsho, H.K. Shon, T. Majeed, I. El Saliby, S. Vigneswaran, J. Kandasamy, S. Hong, and S. Lee, "Blended Fertilizers as Draw Solutions for Fertilizer-Drawn Forward Osmosis Desalination", Environmental Science and Technology, vol. 46, pp. 4567–4575, 2012.

[84] S. Phuntsho, S. Hong, M. Elimelech, and H.K. Shon, "Forward osmosis desalination of brackish groundwater: Meeting water quality requirements for fertigation by integrating nanofiltration", Journal of Membrane Science, vol. 436, pp. 1–15, 2013.

[85] S. Sahebi, S. Phuntsho, J.E. Kim, S. Hong, and H.K. Shon, "Pressure assisted fertiliser drawn osmosis process to enhance final dilution of the fertiliser draw

solution beyond osmotic equilibrium", Journal of Membrane Science, vol. 481, pp. 63–72, 2015.

[86] M. Xie, M. Zheng, P. Cooper, W. E. Price, L. D. Nghiem, and M. Elimelech, "Osmotic dilution for sustainable greenwall irrigation by liquid fertilizer: Performance and implications", Journal of Membrane Science, vol. 494, pp. 32–38, 2015.

[87] S. Phuntsho, J.E. Kim, M.A.H. Johir, S. Hong, Z. Li, N. Ghaffour, T. Leiknes, and H.K. Shon, "Fertiliser drawn forward osmosis process: Pilot-scale desalination of mine impaired water for fertigation", Journal of Membrane Science, vol. 508, pp. 22–31, 2016.

[88] S. Zou, and Z. He, "Enhancing wastewater reuse by forward osmosis with self-diluted commercial fertilizers as draw solutes", Water Research, vol. 99, pp. 235–243, 2016.

[89] L. Chekli, Y. Kim, S. Phuntsho, S. Li, N. Ghaffour, T. Leiknes, and H.K. Shon, "Evaluation of fertilizer-drawn forward osmosis for sustainable agriculture and water reuse in arid regions", Journal of Environmental Management, vol. 187, pp. 137–145, 2017.

[90] L. Chekli, J.E. Kim, I. El Saliby, Y. Kim, S. Phuntsho, S. Li, N. Ghaffour, T. Leiknes, and H. K. Shon, "Fertilizer drawn forward osmosis process for sustainable water reuse to grow hydroponic lettuce using commercial nutrient solution", Separation and Purification Technology, vol. 181, pp. 18–28, 2017.

[91] Y. Kim, Y.C. Woo, S. Phuntsho, L.D. Nghiem, H.K. Shon, and S. Hong, "Evaluation of fertilizer-drawn forward osmosis for coal seam gas reverse osmosis brine treatment and sustainable agricultural reuse", Journal of Membrane Science, vol. 537, pp. 22–31, 2017.

[92] V.H. Tran, S. Phuntsho, H. Park, D.S. Han, and H.K. Shon, "Sulfur-containing air pollutants as draw solution for fertilizer drawn forward osmosis desalination process for irrigation use", Desalination, vol. 424, pp. 1–9, 2017.

[93] X. Xiang, S. Zou, and Z. He, "Energy consumption of water recovery from wastewater in a submerged forward osmosis system using commercial liquid fertilizer as a draw solute", Separation and Purification Technology, vol. 174, pp. 432–438, 2017.

[94] S.M. Ali, J.E. Kim, S. Phuntsho, A. Jang, J.Y. Choi, and H.K. Shon, "Forward osmosis system analysis for optimum design and operating conditions", Water Research, vol. 145, pp. 429–441, 2018.

[95] F. Volpin, L. Chekli, S. Phuntsho, J. Cho, N. Ghaffour, J.S. Vrouwenvelder, and H.K. Shon, “Simultaneous phosphorous and nitrogen recovery from source-separated urine: A novel application for fertiliser drawn forward osmosis”, Chemosphere, vol. 203, pp. 482–489, 2018.

[96] J.E. Kim, J. Kuntz, A. Jang, I.S. Kim, J.Y. Choi, S. Phuntsho, and H.K. Shon, “Techno-economic assessment of fertiliser drawn forward osmosis process for greenwall plants from urban wastewater”, Process Safety and Environmental Protection, vol. 127, pp. 180–188, 2019.

[97] W. Suwaileh, D. Johnson, and N. Hilal, “Brackish water desalination for agriculture: Assessing the performance of inorganic fertilizer draw solutions”, Desalination, vol. 456, pp. 53–63, 2019.

[98] R. Lambrechts and M.S. Sheldon, “Performance and energy consumption evaluation of a fertiliser drawn forward osmosis (FDFO) system for water recovery from brackish water”, Desalination, vol. 456, pp. 64–73, 2019.

[99] F. Volpin, H. Heo, M.A.H. Johir, J. Cho, S. Phuntsho, and H.K. Shon, “Techno-economic feasibility of recovering phosphorus, nitrogen and water from dilute human urine via forward osmosis”, Water Research, vol. 150, pp. 47–55, 2019.

[100] M. Gulied, A. Al Nouss, M. Khraisheh, and F. AlMomani, “Modeling and simulation of fertilizer drawn forward osmosis process using Aspen Plus-MATLAB model”, Science of The Total Environment, vol. 700, 2020.

[101] P. Pourmovahed, M. Lefsrud, and J. Maisonneuve, “Thermodynamic limits of using fertilizer to produce clean fertigation solution from wastewater via forward osmosis”. Journal of Membrane Science, vol. 647 (120168), 2021.

[102] F. Volpin, R.R. Gonzales, S. Lim, N. Pathak, S. Phuntsho, and H.K. Shon, “GreenPRO: A novel fertiliser-driven osmotic power generation process for fertigation”, Desalination, vol.447, pp. 158–166, 2018.

[103] P. Pourmovahed and J. Maisonneuve, “Demonstration of power generation from fertilizer via pressure retarded osmosis”, Transactions of the American Society of Agricultural and Biological Engineers, vol. 64, pp. 495-505, 2021.

[104] P. Pourmovahed and J. Maisonneuve, “Thermodynamic limits of using fertilizer osmosis to produce mechanical work via pressure retarded osmosis”, Journal of Membrane Science, vol. 629 (119268), 2021.

[105] J. Lee and R. Karnik, “Desalination of water by vapor-phase transport through hydrophobic nanopores”, Journal of Applied Physics, vol. 108, 044315, 2010.

[106] J. Lee, A. P. Straub, M. Elimelech, “Vapor-gap membranes for highly selective osmotically driven desalination”, Journal of Membrane Science, vol. 555, pp. 407-417, 2018.

[107] J.L. Niu, L.Z. Zhang, “Membrane-based enthalpy exchanger: material considerations and clarification of moisture resistance”, Journal of Membrane Science, vol. 189 (2), pp. 179–191, 2001.

[108] R. S. Das, S. Jain, “Performance characteristics of cross-flow membrane contactors for liquid desiccant systems”, Applied Energy, vol. 141, pp. 1-11, 2015.

[109] A. Lowenstein, “Review of Liquid Desiccant Technology for HVAC Applications”, HVAC&R Research, vol.14 (6), pp. 819-839, 2008

[110] X. Niu, F. Xiao, Z.Ma, “Investigation on capacity matching in liquid desiccant and heat pump hybrid air-conditioning systems”, International Journal of Refrigeration, vol 35, pp. 160-170, 2012.

[111] Ó. Andrjesdóttir, C. L. Ong, M. Nabavi, S. Paredes, A.S.G. Khalil, B. Michel, D. Poulikakos, “An experimentally optimized model for heat and mass transfer in direct contact membrane distillation”, International Journal of Heat and Mass Transfer, vol. 66, pp. 855-867, 2013.

[112] R. Namvar, G. Gaoming, C. Simonson, and R. Besant, “Transient heat and moisture transfer characteristics of a liquid-to-air membrane energy exchanger (LAMEE) model verification and extrapolation”, International Journal of Heat and Mass Transfer, vol. 66, pp. 757-771, 2013.

[113] N. Zhang, X. Chen, Y. Su, H. Zheng, O. Ramadan, X. Zhang, H. Chen, S. Riffat, “Numerical investigations and performance comparisons of a novel cross-flow hollow fiber integrated liquid desiccant dehumidification system”, Energy, vol. 182, pp. 1115-1131, 2019.

[114] S. Moussaddy, and J. Maisonneuve, “Energy from carbon dioxide: Experimental and theoretical analysis of power generation from membrane-based sweep gas permeation”, Journal of Membrane Science, vol. 644 (120053), 2022.

[115] A. Bahlake, F. Farivar, B. Dabir, “New 3-dimensional CFD modeling of CO2 and H2S simultaneous stripping from water within PVDF hollow fiber membrane contactor”, Heat and Mass Transfer, vol. 52, pp. 1295–1304, 2016.

[116] J.R. Rivero, G. Panagakos, A. Lieber and K. Hornbostel, “Hollow Fiber Membrane Contactors for Post-Combustion Carbon Capture: A Review of Modeling Approaches”, Membranes, vol. 10, no. 12: 382, 2020.

[117] N. Ghasem, “Modeling and Simulation of the Simultaneous Absorption/Stripping of CO2 with Potassium Glycinate Solution in Membrane Contactor”, Membranes, vol. 10 (72) ,2020.

[118] E. E. Matula, J. A. Nabity, “Characterization of simultaneous heat, oxygen, and carbon dioxide transfer across a nonporous polydimethylsiloxane (PDMS) hollow fiber membrane”, Chemical Engineering Journal Advances, vol. 6 (100106), 2021.

[119] T. L. Bergman, A. S. Lavine, F. P. Incropera, and D. P. DeWitt, “Introduction to Heat Transfer” John Wiley & Sons, 2011.

[120] S.W.L. Alan, M.R. Islam, K.J. Chua, “A Theoretical Model on Internally Cooled Liquid Desiccant Dehumidification and Cooling Processes”, Energy Procedia, vol. 142, pp. 1009-1014, 2017.

[121] W. Roetzel, X. Luo, D. Chen, “Design and Operation of Heat Exchangers and their Networks”, Academic Press, 2020.

[122] S-M Huang, M. Yang, and X. Yang, “Performance analysis of a quasi-counter flow parallel-plate membrane contactor used for liquid desiccant air dehumidification”, Applied Thermal Engineering, vol. 63, pp. 323–332, 2014.

[123] X. Chen, Y. Su, D. Aydin, H. Bai, H. Jarimi, X. Zhang, and S. Riffat, “Experimental investigation of a polymer hollow fibre integrated liquid desiccant dehumidification system with aqueous potassium formate solution”, Applied Thermal Engineering, vol. 142, pp. 632-643, 2018.

[124] W.Z. Gao, Y.R. Shi, Y.P. Cheng, W.Z. Sun, “Experimental study on partially internally cooled dehumidification in liquid desiccant air conditioning system”, Energy and Buildings, vol. 61, pp. 202-209, 2013.

[125] M-H. Kim, J-Y. Park, M-K. Sung, A-S. Choi, J-W. Jeong, “Annual operating energy savings of liquid desiccant and evaporative-cooling-assisted 100% outdoor air system”, Energy and Buildings, vol. 76, pp. 538-550, 2014.

[126] A. Vadiee, V. Martin, “Energy management in horticultural applications through the closed greenhouse concept, state of the art”, Renewable and Sustainable Energy Reviews, vol. 16 (7), pp. 5087-5100, 2012.

[127] A. Vadiee, V. Martin, “Energy management strategies for commercial greenhouses”, Applied Energy, vol. 114, pp. 880-888, 2014.

[128] M. Amani, S. Foroushani, M. Sultan, and M. Bahrami, “Comprehensive review on dehumidification strategies for agricultural greenhouse applications”, Applied Thermal Engineering, vol. 181, page 115979, 2020.

[129] N. Katsoulas et al, “Reducing ventilation requirements in semi-closed greenhouses increases water use efficiency”, Agricultural Water Management, vol. 156, 2015.

[130] R. Leferset al, “Liquid desiccant dehumidification and regeneration process to meet cooling and freshwater needs of desert greenhouses”, Desalination and Water

[131] G.A. Longo, A. Gasparella, “Experimental and theoretical analysis of heat and mass transfer in a packed column dehumidifier/regenerator with liquid desiccant”, International Journal of Heat and Mass Transfer, vol 48 (25), pp. 5240-5254, 2005.

[132] X. Liu, M. Qu, X. Liu, L. Wang, “Membrane-based liquid desiccant air dehumidification: A comprehensive review on materials, components, systems and performances”, Renewable and Sustainable Energy Reviews, vol. 110, pp. 444-466, 2019.

[133] A. Ali, K. Ishaque, A. Lashin, and N. Al Arifi, “Modeling of a liquid desiccant dehumidification system for close type greenhouse cultivation”, Energy, vol. 118, pp. 578-589, 2017.

[134] S. Moussaddy, S. Pushparajah, J. Maisonneuve, “Fertilizer-Based Liquid Desiccants: A Novel Concept for Energy Efficient Dehumidification and Water Vapor Recycling in Indoor Plant Environments,” Applied Thermal Engineering, vol. 219 Part B, 119529, 2022.

[135] K. Jeong, M. J. Kessen, H. Bilirgen, and E. K. Levy, “Analytical modeling of water condensation in condensing heat exchanger,” International Journal of Heat and Mass Transfer, vol. 53 (11–12), pp. 2361-2368, 2010.

[136] F.W. Yu, K.T. Chan, R.K.Y. Sit and J. Yang, “Review of standards for energy performance of chiller systems serving commercial buildings”, Energy Procedia, vol. 61, pp. 2778 – 2782, 2014.

[137] Z-X Li, L-Z. Zhang, “Flow maldistribution and performance deteriorations in a counter flow hollow fiber membrane module for air humidification/dehumidification”. International Journal of Heat and Mass Transfer, vol. 74, pp. 421-430, 2014.

[138] F. H. Akhtar, M. Kumar, K.-V. Peinemann, “Pebax®1657/Graphene oxide composite membranes for improved water vapor separation”, Journal of Membrane Science, vol. 525, pp. 187-194, 2017.

[139] P. G. Ingole, M. Sohail, A. M. Abou-Elanwar, M. Irshad-Baig, J-D. Jeon, W. K. Choi, H. Kim, H. K. Lee, “Water vapor separation from flue gas using MOF incorporated thin film nanocomposite hollow fiber membranes”, Chemical Engineering Journal, vol. 334, pp. 2450-2458, 2018.